NO_X STORAGE AND REDUCTION OVER CE-ZR MIXED OXIDE SUPPORTED CATALYSTS

A THESIS SUBMITTED TO
THE GRADUATE SCHOOL OF NATURAL AND APPLIED SCIENCES
OF
MIDDLE EAST TECHNICAL UNIVERSITY

BY

BAŞAR ÇAĞLAR

IN PARTIAL FULFILLMENT OF THE REQUIREMENTS
FOR
THE DEGREE OF MASTER OF SCIENCE
IN
CHEMICAL ENGINEERING

FEBRUARY 2009

Approval of the thesis:

NO_X STORAGE AND REDUCTION OVER CE-ZR MIXED OXIDE SUPPORTED CATALYSTS

submitted by **BAŞAR ÇAĞLAR** in partial fulfillment of the requirements for the degree of **Master of Science in Chemical Engineering Department, Middle East Technical University** by,

Prof. Dr. Canan Özgen
Dean, Graduate School of **Natural and Applied Sciences** _____

Prof. Dr. Gürkan Karakaş
Head of Department, **Chemical Engineering** _____

Prof. Dr. Deniz Üner
Supervisor, **Chemical Engineering Dept., METU** _____

Examining Committee Members:

Prof. Dr. Hayrettin Yücel
Chemical Engineering Dept., METU _____

Prof. Dr. Deniz Üner
Chemical Engineering Dept., METU _____

Prof. Dr. Gürkan Karakaş
Chemical Engineering Dept., METU _____

Prof. Dr. Margarita Kantcheva
Chemistry Dept., Bilkent University _____

Assist. Prof. Dr. Ayşen Yılmaz
Chemistry Dept., METU _____

Date: _____

I hereby declare that all information in this document has been obtained and presented in accordance with academic rules and ethical conduct. I also declare that, as required by these rules and conduct, I have fully cited and referenced all material and results that are not original to this work.

Name, Last name: Başar Çağlar

Signature:

ABSTRACT

NO_X STORAGE AND REDUCTION OVER CE-ZR MIXED OXIDE SUPPORTED CATALYSTS

Çağlar, Başar

M. S., Department of Chemical Engineering
Supervisor: Prof. Dr. Deniz Üner

February 2009, 109 pages

NO_x storage and reduction activities of $Pt/BaO/Ce_xZr_{1-x}O_2$ (x= 1, 0.75, 0.5, 0.25, 0) catalysts were investigated by transient reaction analysis and Diffuse Reflectance Infrared Fourier Tramsform Spectroscopy (DRIFTS). $Pt/BaO/Al_2O_3$ catalyst was used as reference catalyst. Ce-Zr mixed oxides were synthesized by means of Pechini Method. Pechini method is a sol-gel like method based on mixing the related mixed oxide precursors with an α-hydroxy carboxylic acid. 10% BaO (w/w) and 1% Pt (w/w) were deposited on synthesized mixed oxide and reference alumina support via incipient wetness impregnation. Prepared catalysts were characterized by BET, XRD and in-situ DRIFTS. $Pt/BaO/Ce_xZr_{1-x}O_2$ catalysts (x= 0.75, 0.5, 0.25) exhibited higher surface than pure ceria and zirconia supported catalysts and highest surface was observed for $Pt/BaO/Ce_{0.5}Zr_{0.5}O_2$. The reducibility of catalysts was tested by Temperature Programmed Reduction (TPR). It was observed that the reducibility of $Pt/BaO/Ce_xZr_{1-x}O_2$ catalysts increases with incorporation of Zr into ceria lattice. $Pt/BaO/Ce_{0.25}Zr_{0.75}O_2$ showed the highest reducibility. The Pt dispersions of catalysts

were determined by CO chemisorption. The highest Pt disperison was observed in the presence of $Pt/BaO/Ce_{0.5}Zr_{0.5}O_2$ catalyst. NO_x storage and reduction efficiency of the catalysts were determined by transient reaction analysis in a home-built setup at 350^oC. The reaction results revealed that all catalysts exhibit similar NO_X storage and reduction performance. The NO_X storage performances of all catalysts were differentiated via in-situ DRIFTS analysis. $Pt/BaO/Ce_xZr_{1-x}O_2$ (x= 0.75, 0.5, 0.25) catalysts revealed higher performance than the ceria and zirconia supported catalysts. $Pt/BaO/Ce_{0.5}Zr_{0.5}O_2$ catalyst absorbed highest amount of NO on the surface in the form of nitrate. The reduction behaviours of catalysts also were investigated by in-situ DRIFTS. It was observed that nitrates and nitrites were completely removed from the surface after reduction by H_2 at 300^oC.

Keywords: NSR, Ce-Zr mixed oxide, TPR, transient reaction analysis, in-situ DRIFTS

ÖZ

CE-ZR KARIŞIK OKSİTLERİ İLE DESTEKLENEN KATALİZÖRLER ÜZERİNDE NO_X DEPOLAMA VE İNDİRGEME

Çağlar, Başar

Yüksek Lisans, Kimya Mühendisliği Bölümü
Tez Yöneticisi: Prof. Dr. Deniz Üner

Şubat 2009, 109 sayfa

$Pt/BaO/Ce_xZr_{1-x}O_2$ (x= 1, 0.75, 0.5, 0.25, 0) katalizörlerinin NO_x depolama ve indirgeme verimleri zamana bağlı reaksiyon analizi ve DRIFTS kullanılarak incelendi. Referans katalizör olarak $Pt/BaO/Al_2O_3$ kullanıldı. Ce-Zr karışık oksitleri Pechini metodu kullanılarak sentezlendi. Pechini metodu, α hidroksil karboksil acid ile ilgili karışık oksitlerin öncül maddelerinin karışması esasına dayalı bir yöntemdir. Hazırlanan karışık oksitler ve referans olarak kullanılan aluminyum oksit üzerine kütlece %10 BaO ve kütlece %1 Pt yüklemesi yapıldı. Katalizörler hazırlandıktan sonra BET, XRD ve in-situ DRIFTS ile karakterize edildi. Destek malzemesi karışık oksit olan malzemelerin, destek malzemesi saf seryum dioksit ve zirkonyum dioksit olan malzemelere göre daha yüksek yüzey alanı gösterdiği görüldü. En yüksek yüzey alanı $Pt/BaO/Ce_{0.5}Zr_{0.5}O_2$ katalizör varlığında gözlemlendi. Katalizörlerin yüzey indirgenebilirlikleri sıcaklık programramlı indirgeme yöntemi ile test edildi. $Pt/BaO/Ce_xZr_{1-x}O_2$ katalizörlerinin yüzey indirgenebilirliklerinin, Zr atomunun seryum dioksit kafes yapısı içindeki miktarının artmasıyla orantılı olarak arttığı

gözlemlendi. $Pt/BaO/Ce_{0.25}Zr_{0.75}O_2$ katalizörünün en yüksek yüzey indirgenebilirliğine sahip olduğu görüldü. Katalizör yüzeylerindeki Pt dağılımı CO kimyasal sorption işlemi ile belirlendi. En yüksek Pt dağılımı $Pt/BaO/Ce_{0.5}Zr_{0.5}O_2$ katalizörü varlığında görüldü. Katalizörlerin NO_x depolama ve indirgeme verimleri kendi hazırladığımız düzenekte zamana bağlı reaksiyon analizi yöntemi ile incelendi. Reaksiyon sonuçları katalizörlerin benzer depolama ve indirgeme verimlerine sahip olduğunu gösterdi. Katalizörlerin depolama verimleri in-situ DRIFTS analizi kullanılarak birbirinden ayırıldı. $Pt/BaO/Ce_xZr_{1-x}O_2$ (x= 0.75, 0.5, 0.25) katalizörlerinin seryum dioksit ve zirkonyum dioksit ile desteklenen katalizörlerden daha yüksek depolama performansı gösterdiği görüldü. Katalizörlerin indirgeme verimleri de in-situ DRIFTS analizi kullanılarak incelendi. 300^oC'de H_2 ile indirgendikten sonra bütün katalizörler için nitratların ve nitritlerin tamamen yüzeyden uzaklaştırıldığı görüldü.

Anahtar kelimeler: NSR, Ce-Zr karışık oksitleri, TPR, dönüşümlü reaksiyon analizi, in-situ DRIFTS

To my parents and my love

ACKNOWLEDGMENTS

I would like to thank my supervisor Prof. Dr. Deniz Üner for her valuable support, encouragement, guidance and patience. I am also very grateful to for her invaluable assistance in every aspect of life outside the laboratory.

Assist. Prof. Dr. Ayşen Yılmaz is gratefully acknowledged for her friendly and positive attitude and constructive comments throughout this study.

I also wish to express my great appreciation to every member of CACTUS Research Group: Osman Karslıoğlu, Orçun Ergün, Volkan Değirmenci, Arzu Kanca, Mert Mehmet Oymak, Mukaddes Can, Hilal Demir Kıvrak, Mehmet Kaptan, Özge Güner, Berk Giray and newly joined members; Bahar İpek, Saygın Aras, Oğuz Canıaz and Svetlana. I would like to thank my hememates Barış Erdoğan and Bilal Bayram and my friends Egemen Agi, Ayça Arınan, Ayşegül Çiftçi, Cem Tokay, Saltuk Pirgalıoğlu, Canan Gücüyener, Canan Yeniova, Tuğçe İrfan Ersöz, Güzide Aydın, İlker Soner and Hatice Ceylan in Chemical Enginnering Department for their friendship and supports.

I want to extend my thanks to Mehmet Kayran, Semih Seyyidoğlu and Tolga Depçi in Chemistry Department, for their technical assistance during XRD measurements and their friendly approach.

The technical assistance by Gülten Orakçı in BET measurements, İsa Çağlar for glasware work, electrician Nevzat Bekçi for setting up the electronic switchboard of the solenoid, and Adil Demir, Süleyman Arslan, and Ertuğrul Özdemir for their support and assistance are appreciated.

The Turkish Automobile Factory (TOFAŞ-FIAT) and the Scientific and Research Council of Turkey (TUBİTAK, Research Grant No: CAYDAG 106Y075 and MAG 107M447) are kindly acknowledged for the MS scholarship and financial support during the study.

My last and special thanks are to my eternal love, Ebru. She was always with me and encouraged me throughout this study. She was my real motivation to complete the works. I am grateful for having you in my life. Thank you my cute darling.

TABLE OF CONTENTS

APPENDICES

LIST OF TABLES

TABLES

LIST OF FIGURES

FIGURES

LIST OF SYMBOLS

Å	Angstrom, length unit
A/F	Air to fuel ratio (w/w)
BET	Brunauer-Emmett-Teller
BJH	Barrett-Joyner-Halenda
C_p	Constant Pressure Heat Capacity, J/mol
DRIFTS	Diffuse Reflectance Infrared Fourier Transform Spectrometry
$\Delta G°$	Gibbs' Free Energy of Formation, J/mol
ΔG_{rxn}	Gibbs' Free Energy Change on Reaction, kJ/mol
ΔG°_{rxn}	Gibbs' Free Energy Change on Reaction at STP, kJ/mol
$\Delta H°$	Enthalpy of Formation, kJ/mol
ΔH_{rxn}	Enthalpy Change on Reaction, kJ/mol
FT-IR	Fourier Transform Infrared
ICDD	International Centre for Diffraction Data
ID	Internal Diameter, mm
K_{eq}	Equilibrium Constant
K_0	Equilibrium Constant at Standard States
λ	Air to fuel molar ratio
MECA	Manufacturers of Emission Controls Associations
M_n	Molecular Weight, g/mol
ppm	Parts per million
R	Universal Gas Constant (j/(mol*K))
rxn	Reaction
T	Temperature, K
TPR	Temperature Programmed Reduction
TWC	Three Way Catalytic Converter
XRD	X-ray Diffraction

CHAPTER 1

INTRODUCTION AND OBJECTIVE

According to the studies about energy consumption and global warming, 50% of total oil consumption and 21% greenhouse emissions originated from transportation [1]. Therefore, the two of the primary technological challenges engine manufacturers continuously confront are the fuel economy and emissions control [2]. In order to improve the fuel consumption and pollutant emission in vehicles, automobile manufacturers is now promoting continuous lean operation rather than the current stoichiometric-mode by increasing the air to fuel ratio in the combustion chamber. Normally, gasoline engines operate close to stoichiometric air to fuel ratio ($\lambda=1$) and this ratio is increased by operating the vehicle under lean-burn conditions ($\lambda>1$) to decrease the fuel consumption and therefore pollutant emissions. Although lean-burn engines produce cleaner engine-out exhaust, the effluent streams still contain significant levels of carbon monoxide, unburned hydrocarbons, nitrogen oxides (NOx) and also particulate matter (carboneous product of lean-burn exhaust) not being present in the exhaust of gasoline engine. Moreover the three-way catalysts (TWC) used for emission control on current-production gasoline vehicles are not effective for reducing nitrogen oxides (NOx) in lean burn engines [3]. Reducing NO_X to N_2 in the lean, or O_2-rich, exhaust is problematic. Current three way catalytic converters on lean-burn engine exhausts can not meet today's regulations for NO_X emissions [2]. Therefore, implementation of lean-burn engines requires development of a new catalyst technology to remove NO_X emissions and an innovation for particulate matter abatement.

1.1 Lean Burn Engines-Diesel Engines

Lean-burn engine is an engine that operates under oxygen excess conditions which means that the amount of air in the combustion chamber is greater than that in conventional gasoline engines. In gasoline engine, the air to fuel ratio (A/F) is 14.7 as weight ratio (w/w) and 1 as molar ratio (λ=1). On the other hand, in lean burn engines air to fuel ratio (A/F) is greater than 20 as weight ratio (>20). Therefore, lean burn engines provide fuel efficient operation. Depending on the driving conditions, a lean-burn engine can decrease fuel consumption by up to 30% compared with a stoichiometric engine [4].

There are two types of lean burn engines; (i) spark ignited lean burn gasoline engines and (ii) compression ignited Diesel engine. These two engines are differentiated from each other according to their thermodynamic operation cycles. Spark ignited gasoline engines operate according to Otto cycle whereas Diesel engines operate according to Diesel cycle. Main difference of these two cycles is related to the type of action during combustion. In Diesel cycle, isobaric expansion takes place during combustion while, in Otto cycle heat addition is isochoric, in other words, piston does not move during combustion. This isobaric expansion in Diesel cycle allows the operation at high volumetric compression ratio and so providing higher thermal efficiency. Nonetheless, in Otto cycle there is no permission to run at high volumetric compression ratio, since pressure increases substantially during isochoric combustion and causes to break the pistons and the other parts of engine. In Diesel engine, this dramatic pressure increase during combustion is compensated by isobaric expansion [5]. Therefore, diesel engine has higher volumetric compression ratio (14-25) compared to gasoline engine (8-12) and this results in high thermal efficiency.

Due to having both lean-burn characteristic properties (lower fuel utilization) and high thermal efficiency, a Diesel engine emits lower amount of pollutant than the gasoline counterparts. On the other hand, the Diesel engines emit high amount of nitrogen oxides (NOx) and particulate matter than the gasoline engines having a

three way catalytic converter system and exhaust emission require significant reductions of these pollutants. Thus, there is a pressing need to develop Diesel emission control technology to take full advantage of the fuel efficiency and durability of Diesel vehicles.

1.2 Exhaust Emissions

Air pollution generated from mobile sources is a problem of general interest. In the last 60 years, the World vehicle fleet has increased from about 40 million vehicles to over 700 million; this figure is projected to increase to 920 million by the year 2010. The environmental concern originated by mobile sources is due to the fact that the majority of engines employ combustion of fuels derived from crude oil as a source of energy [6]. If the hydrocarbon is burned with air ideally, the reaction gives water (H_2O) and carbon dioxide (CO_2). However, if the non-perfect combustion takes place, then significant amount of pollutants form in the engine and they must be converted to harmless products before exhaust. Typical exhaust compositions of Diesel and gasoline engines are shown in Table 1.1. As seen in Table 1.1, exhausts contain three main pollutants; unburned hydrocarbons (HC), carbon monoxide (CO) and nitrogen oxides (NOx). In addition, Diesel engine exhaust also contains particulate matter (PM).

Unburned hydrocarbon (HC) and carbon monoxide (CO) forms because of non-complete oxidation reaction and generally in the presence of scarce oxygen. NO_X primarily forms due to combination of atmospheric nitrogen (N_2) and oxygen (O_2) at high temperatures. Particulate matter (PM) is primarily composed of soot. Soot forms as result of pyrolysis of highly viscous fuel droplet in the fuel rich zone. Soot particles, consisting of a carbonaceous solid core with adsorbed hydrocarbons, sulphates, and polycyclic aromatic hydrocarbons (PAH), exhibit a highly defective structure and are highly functionalised [7]. In comparison to the Gasoline engines, the Diesel engines emit lower amount of HC, CO and NO_X and higher amounts of PM as seen in Table 1.1.

Table 1.1: Exhaust conditions of Diesel and four strokes spark ignited engine (gasoline engine) [6]

Exhaust Components and Conditions	Diesel Engine	Four-stroke spark ignited-engine
NO_X	350-1000 ppm	100-4000 ppm
HC	50-330 ppm C	500-5000 ppm C
CO	300-1200 ppm	0.1-6 %
O_2	10-15 %	0.2-2 %
H_2O	1.4-7 %	10-12 %
CO_2	7%	10-13.5 %
SO_X	10-1000 ppm	15-60 ppm
PM	65 mg/m^3	-
Temperatures (test cycle)	r.t.-650^oC (r.t.-420 ^oC)	r.t.-1100^oC
GHSV	30000-100000	30000-100000
λ(A/F)	~1.8 (26)	~1.0 (14.7)

Exhaust composition is mainly affected by the fuel characteristics and air to fuel ratio. When taking in to account the fuel caharacteristics, there are three main properties of fuel that affect the composition of pollutants; (i) density (ii) sulphur content (iii) cetane number. A variation of density alters exhaust emissions; the high density fuels increase the probability of PM formation. The presence of suplhur in the fuel causes sulphur oxide emissions and also to increase PM formation by increasing sulfate content of PM. Sulfur oxides can not be removed by post combustion reactions and so it is preferred to minimise sulphur emissions by diminishing the sulphur content of fuel. Cetane number is a measurement of the combustion quality of the Diesel fuel during compression ignition and high cetane numbers decrease HC, CO and NO_X emissions. How the air to fuel ratio (A/F) influences engine emissions is shown in Figure 1.1. As seen in the Figure, under the rich operation the amount of NO_X is low because of oxygen deficiency. However, under lean conditions, the low combustion temperature leads to lower NO_X emissions and excess oxygen causes to decrease the HC and CO concentrations. At very high A/F ratio, misfire occurs and HC emissions increases dramatically again [6].

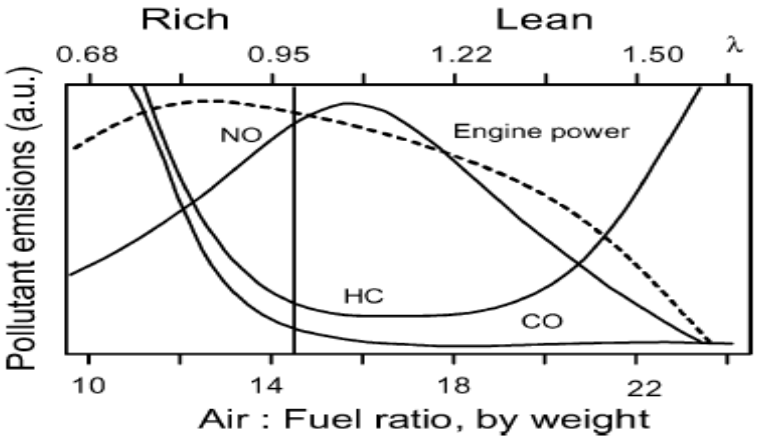

Figure 1.1: The effect of A/F ratio on engine emissions and engine power [6]

1.3 Exhaust Emissions Regulations

Due to negative impact on environment and human health caused by engine emissions, the pollutants including hydrocarbons (HC), carbon monoxide (CO), nitrogen oxides (NO_X) and particulate matter (PM), are regulated by law in many developed countries [8]. The Diesel emission regulations effective in 2009 are summarized at Table 1.2 [9].

Table 1.2: Diesel Emission Standards of USA, EU and Japan as of year 2009 [9]

	USA Tier 2 Bin 5	Europe Euro V	Japan JC 08
HC (g/km)	0.056	-[a]	0.024
NOx (g/km)	0.04	0.18	0.08
CO (g/km)	2.62	0.50	0.63
PM (g/km)	0.006	0.005	0.005

[a] In Europe HC emission in Diesel cars is not allowed. There is another regulation for total HC+NOx concentration. Emission limit of HC+NOx will be 0.23 g/km in 2009.

1.4 NO_X Emissions

Combustion of fuels in transport devices, power plants, house heating and the chemical industry constitute the major sources of NOx emissions [10]. Nitrogen monoxide (NO) accounts for 95% of all nitrogen oxide (NO_X) emissions. NO forms as a result of reaction between nitrogen (N_2) and oxygen (O_2) at high temperature.

Nitrogen oxides (NOx) are extremely toxic to a human body and also harmful to environment [11], since they are suspected to cause acidification of ground and lake water and eutrofication. They also leads to the formation of ground level ozone by reacting with HC in the presence of sunlight [12 and references therein].

Upcoming regulations for diesel engines require significant reductions in NO*x* emissions, in the order of 50–60 % in Europe and Japan, and 80–90 % in the US [13] in order to meet regulations given in Table 1.2.

1.5 Aftertreatment Systems for NOx Abatement

The aim of aftertreatment systems for NOx abatement is to convert all nitrogen oxides (NO_X) to nitrogen (N_2). This desired reaction is a reduction reaction and so there is a need of reductants equivalent amount of NO_X. HC and CO are main reductants to reduce NO_X in the exhaust. HC and CO reduce all NOx molecules to N_2 when the engine run at stoichiometric A/F ratio by using Three Way Catalytic (TWC) Converter, since only at this condition (stoichiometric A/F ratio) the amount of reductants (HC and CO) balances the amount of NO_X. Otherwise, it is not possible to achieve high conversions of NO_X.

TWC converter is catalytic system which consists of honeycomb monolith filter containing reduction and oxidation catalyst. The reactions that take place on the filter are shown in the following:

On Reduction Catalyst:

$$2NO \Leftrightarrow N_2 + O_2 \quad (1.1)$$

$$2NO_2 \Leftrightarrow N_2 + 2O_2 \quad (1.2)$$

On Oxidation Catalyst:

$$2CO + O_2 \Leftrightarrow 2CO_2 \quad (1.3)$$

$$HC + O_2 \Leftrightarrow CO_2 + H_2O \quad (1.4)$$

Catalytic materials are loaded on the filters via washcoating. Washcoat composition consists of Al_2O_3, CeO_2-ZrO_2 mixed oxide, noble metals (NM) and barium oxide and lanthana. Al_2O_3 in washcoat composition provides high surface area for the catalytic reaction. CeO_2-ZrO_2 mixed oxide and barium oxide and lanthana are added as oxygen storage promoters and surface area stabilizers, respectively. Actual active phase in washcoat composition is the noble metal. Noble metal enables to carry out oxidation and reduction reactions simultaneously. Pt and Rh is used as reduction catalyst and Pt or Pd is used as oxidation catalyst.

The performance of TWC mainly depends on the A/F ratio, in other words, it depends on the amounts of reductants (HC, CO) and oxidants (NO_X, O_2). Figure 1.2 exhibits how the pollutants conversion changes according to A/F ratio (w/w) by using TWC.

It is observed that when the A/F ratio is 14.7 (stoichiometry), nearly all pollutants are converted. This is related to balancing the amount of oxidants and reductants. However, when the ratio is different from the stoichiometry than the balance breaks down and the conversion decreases. Therefore, the TWC activity is restricted to the stoichiometric combustion and is employed for treating NOx emissions in gasoline engine [15] whereas it is not effective for NO_X reduction in lean burn engines. As shown from Figure 5, when the A/F is greater than the stoichiometric (>14.7) then the amount of oxidants in the exhaust line increases. This net-oxidizing atmosphere enables the straightforward oxidation of hydrocarbons and CO, whereas NOx

reduction reaction can not take place due to lack of reductants. Since the traditional TWC does not work for lean exhausts there is a compulsory need to find new ways for NO_X reduction under oxidizing conditions [16].

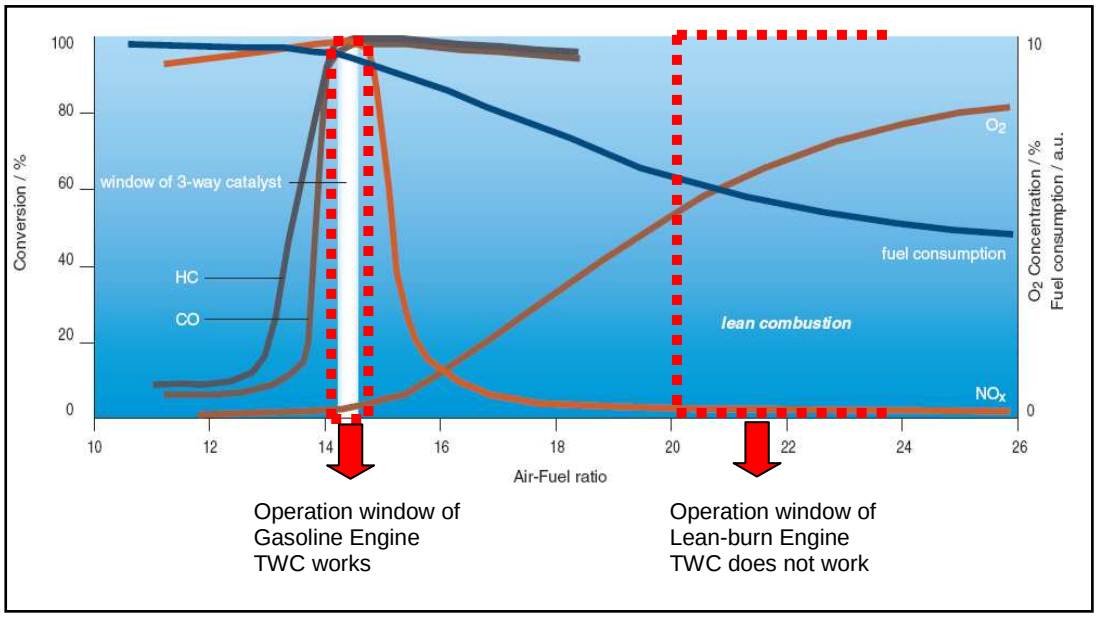

Figure 1.2: Pollutant conversion with respect to A/F ratio by using TWC [14]

Consequently, to increase the fuel economy while still preserving low emissions of NO_X, new catalytic strategies are needed. A variety of techniques are currently being investigated [15]. There are two main approaches: (i) increasing the amount of reductants up to level at which oxidant/reductant balance occurs, called Selective Catalytic Reduction (SCR) (ii) trapping the NO_X molecules at lean period and then switching the medium to rich and reducing NO_X to N_2, called lean NOx trap (LNT) or NOx Storage and Reduction (NSR). In SCR approach, NO_X is reduced to N_2 by adding a reducing agent under lean conditions. Selective Catalytic Reduction could be carried out by two different reducing agents: urea or NH_3 called NH_3-SCR and hydrocarbon, called HC-SCR. In HC-SCR applications, fuel is directly injected to the exhaust line and NO_X is catalytically reduced to N_2. In the HC-SCR research, a large number number catalyst was studied. Metal ion-exchanged zeolites (e.g. Cu-,

Co-, Fe-, Pt-) and supported platinum group metals (PGMs) such as Pt, Pd, Rh, Ag, on various metal oxides (e.g. Al_2O_3, TiO_2, CeO_2) were studied for HC-SCR reactions. However, the rather poor stability of metal ion-exchanged zeolites and the deactivation of base metal oxides in the presence of water in the feed constitute the main drawbacks of these catalysts to be used under real lean conditions. Moreover, supported PGMs exhibit rather low selectivity to N_2 and N_2O being formed in substantial amounts [17]. Not only having selectivity and stability problems but also bringing about extra fuel utilization, HC-SCR is not commonly applied to automobiles. In NH_3-SCR applications, urea solution is vaporised and injected in the pre-heated zone where carbon dioxide and NH_3 form as a result of hydrolysis of urea. Urea hydrolysis reaction is shown in the following:

$$CO(NH_2)_2 + H_2O \Leftrightarrow CO_2 + 2NH_3 \quad (1.5)$$

After hydrolysis, urea reacts with NOx in the presence of excess oxygen and gives N_2 and H_2O according to reactions (1.6), (1.7) and (1.8).

$$4NH_3 + 4NO + O_2 \Leftrightarrow 4N_2 + 6H_2O \quad (1.6)$$

$$6NO_2 + 8NH_3 \Leftrightarrow 7N_2 + 12H_2O \quad (1.7)$$

$$NO + NO_2 + 2NH_3 \Leftrightarrow 2N_2 + 3H_2O \text{ (fast SCR)} \quad (1.8)$$

The standard catalysts used in NH_3-SCR are TiO_2-WO_3-V_2O_5 or TiO_2-WO_3-V_2O_5. NH_3-SCR is more commonly used techniques compared to HC-SCR, but it has two important problems: (i) storage (ii) suitable urea injection. Though there are some applications of urea storage tank on heavy-duty vehicles, no application on light-duty vehicles are present due to the size of storage tank. It is possible to construct a small size storage tank, but if it is so, then NH_3 must be refueled frequently. Second problem is related to the potential risk of NH_3 which is explosive, corrosive and toxic. Thus, suitable amount of urea must be injected to the system and the ammonia slip must not exceed 10 ppm to prevent possible damage. Second approach for NO_X reduction in lean conditions is the storage and reduction approach. Firstly, NO_X is

stored on the catalytic surface as nitrate or nitrite form during lean operation. Then the medium is switched from lean to rich and the stored NO_X molecules are reduced by rich composition of exhaust gas. In NSR, the catalyst composition, lean/rich duration time, and the type and composition of reducing agent given to the system in the rich period are important parameters that influence the NO_X conversion and selectivity to N_2.The main catalytic material used in NSR system is $Pt/BaO/Al_2O_3$. Alumina is used as support material and provides high surface area. Barium oxide has a function to store NO_X molecules on the surface and platinum provides oxidation and reduction capability to the catalyst. NSR system is highly preferred compared to SCR system bacause of reductant storage and injenction problems. Nonetheless, supplying reductants to the system is also a problem for NSR. The reductant provided by either the fuel of vehicle or another reductant tank is a still a point of issue. Apart from this fact, the main objective is to provide high conversion and selectivity with minimum economic load.

1.6 Objective of the Thesis

In this thesis, NO_X storage and reduction system was investigated in detail. The parameters that influence the NSR system efficiency were evaluated by following the methods presented in the literature. The main objective of the study was to develop a new NSR catalyst formulation for achieving high NO_X conversion and selectivity. For this purpose, Ce-Zr mixed oxide system was selected as a new support material for NSR catalyst. $Pt/BaO/Ce_xZr_{1-x}O_2$ catalysts were prepared and the storage and reduction behaviour of the prepared catalysts were studied. The objective was to observe the effect of Ce-Zr mixed oxide support on the NO_x storage and reduction efficiency by comparing with the most commonly used $Pt/BaO/Al_2O_3$ catalyst.

CHAPTER 2

LITERATURE SURVEY

2.1 General Overview of NO_X Storage and Reduction (NSR) Technology

NO_X storage and reduction (NSR) technology is used for NO_X reduction in lean-burn engines and diesel engines. The inherent difficulty of NO_X reduction in lean burn and diesel engines is selectively reducing NO_X to N_2 in oxygen-rich environment without resulting in unacceptable fuel efficiency losses [18]. One of the techniques that overcome this difficulty is NO_X Storage and Reduction (NSR) technique. NSR technology is based on cyclic catalytic operation. While engine is running lean, NO and O_2 react to form NO_2 on active metal site and NO_2 molecules is trapped on the catalyst surface. Then, this lean period is interrupted by rich excursion to regenerate the catalyst surface. During the rich excursion, NO_X molecules leave from the surface and are reduced to N_2 molecules on the active metal sites. Lean-rich cycles continue sequentially. Storage and reduction process in lean/rich duration time are schematically represented in Figure 2.1.

Lean period takes generally 2-8 minutes and during this period engine runs at lean-burn condition (A/F ratio greater than stoichiometry), in other words, under oxidizing medium. At the end of this period, rich pulse is introduced to the system and reductant concentration increases. There are three different ways to introduce rich pulse: (i) running the engine at stoichiometric conditions (ii) direct fuel injecting to the exhaust line (iii) injection of reductants produced by fuel reforming. Rich period

takes generally 20-60 seconds. The Engine works by cycling lean/rich period sequentially. Concentration and duration of rich pulse is important for fuel economy. The rich pulse must be highly concentrated and the duration of pulse must be as low as possible. According MECA report in 1999, greater than 3% reduction in fuel economy resulting from either operating scheme would be unacceptable. Determining the requisite fuel consumption to achieve a high NO_X conversion is essential in assessing the viability of NSR [19].

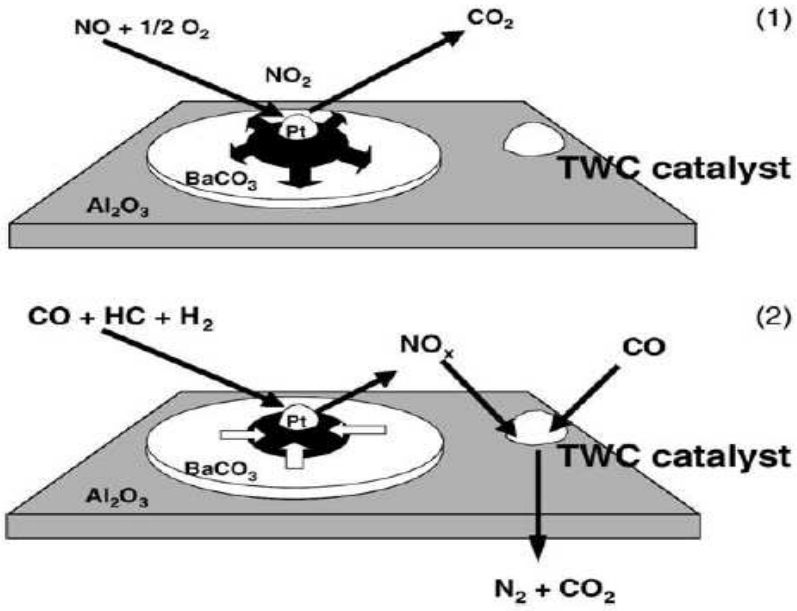

Figure 2.1: Schematic presentation of (1) storage and (2) reduction process [6]

Catalysts that are used in NSR process require strong basic properties to achieve storage of NO and NO_2 molecules, and redox properties to oxidize and reduce NO molecules. NSR catalysts used in literature are composed of alkaline earth metal to bring the catalysts basic character and nobel metal to facilitate redox reactions. Mostly used formulation for NSR catalysts is Pt/BaO/γ- Al_2O_3.

2.2 NSR Catalytic Process

NSR catalytic process consists of four sequential steps: (i) NO oxidation to NO_2 (ii) NO_X storage (NO_X trap) on the catalyst surface in the form of nitrite and nitrate form (iii) NO_X release from nitrite and nitrate sites (iv) NO_X reduction to N_2 [18]. All steps are associated with each other and all of them are transient. The steps of NSR process are shown in Figure 2.2 that exhibits the NO_X concentration profile as a function of the time. As shown in the figure, the NO_X concentration during first minutes is zero that means all NO_X molecules are stored on the surface. Then, after the dead time, the NO_X concentration increases slowly and reaches the maximum point (saturation point) at which NO_X concentration is equal to the concentration of NO_X in the inlet gas. As the surface is fully saturated, the NO_X concentration is at maximum, the storage period is completed. At the end of storage period, reductants are fed to the system and the oxidizing medium is replaced by a reductant rich medium. The intermittent shift of the atmosphere into a rich-burn condition brings about of releasing of adsorbed NO_X molecules. At this point the NO_X concentration increases dramatically as shown in Figure 2.2. After releasing, NO_X molecules are reduced to N_2. The NO_X concentration decreases rapidly and at the end of the rich period reaches zero that means that all NO_X molecules relaesed from the surface are converted to N_2 and to the other byproducts (N_2O, NH_3) depending on the selectivity.

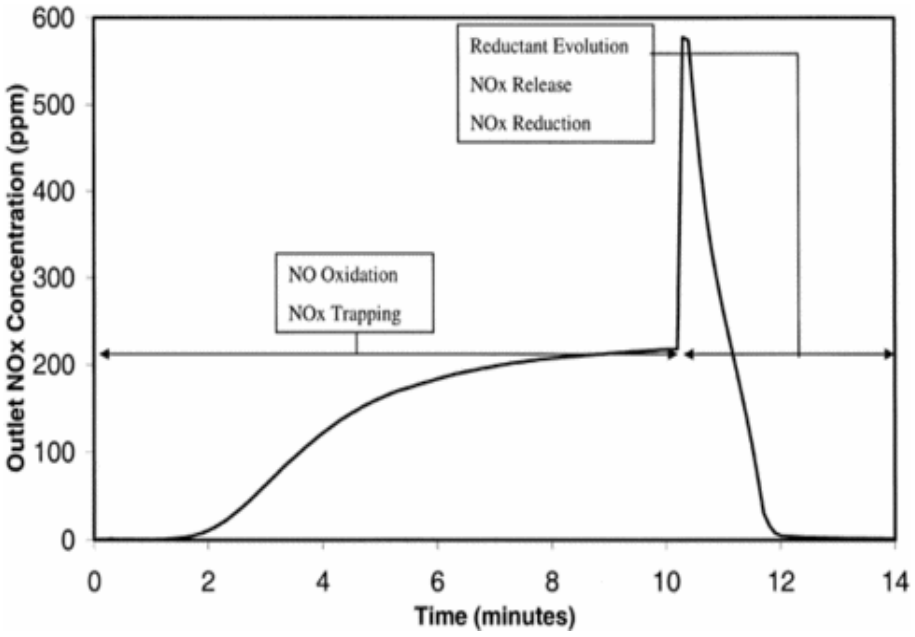

Figure 2.2: NO_X concentration profile with respect to time through all NSR operation [18]

2.2.1 NO oxidation to NO_2

NO_X in real engine exhaust primarily consists of NO. In the first step of NSR, NO is oxidized to NO_2. In the literature it was suggested that NO_2 is precursor for the trapping process. Experiments show that when only NO_2 is fed to the $Pt/BaO/Al_2O_3$ catalyst, substantial NO_X adsorption occurs, whereas, when the feed gas includes just only NO in the absence of O_2, much less NO molecules are trapped on the surface. Actually, it was proposed that this minor adsorption is associated with a residual surface oxygen participating in the oxidation reaction, direct adsorption onto Pt or weak adsorption onto other components of the catalyst. The difference in catalytic activity when comparing NO_2 to NO in the presence of O_2 is related to kinetic limitations of NO oxidation reactions on the noble metal sites. When the temperature is increased above 300^oC, the kinetic limitations are eliminated, then no difference was observed between NO or NO_2 as NO_X source. According to the experimental studies it may be concluded that NO_2 plays an important role in the catalytic trapping

process in the absence or presence of O_2 and one way to improve trapping efficiency is to enhance the oxidation ability of catalyst.

NO oxidation reaction occurs on the noble metal sites of NSR catalyst and it can be either kinetically or thermodynamically limited in the Diesel operation conditions. In the low temperature region, the reaction is kinetically limited and at temperature higher than 200^{o}C the equilibrium dictates lower NO_2 conversion as temperature increases (Thermodynamic NO/NO_2 equilibrium values for different O_2 concentration are shown in Figure 2.3). Thus, there is an optimum temperature to achieve a high conversion of NO depending on the catalyst characteristic (surface area, noble metal dispersion) and residence time or space velocity. In the study of Epling et. al. [18] this temperature was determined 350^{o}C and 380^{o}C for a space velocity 10000 h^{-1} and 25000 h^{-1} respectively in the presence of Pt/Al_2O_3 catalyst (Figure 2.4).

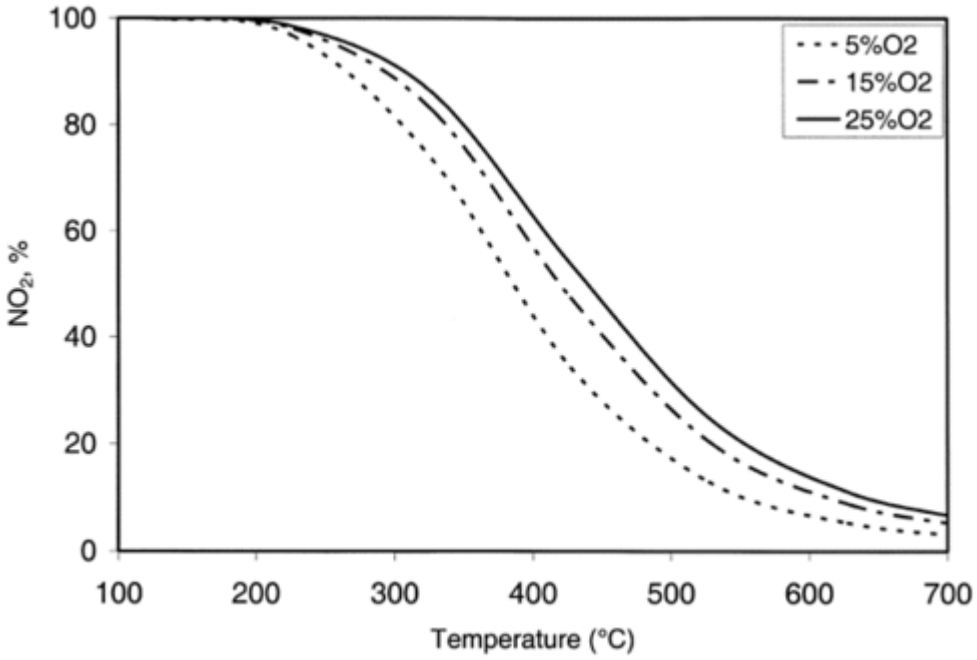

Figure 2.3: Thermodynamic NO/NO_2 equilibrium values for 5, 10 and 15 % O_2 concentrations [18]

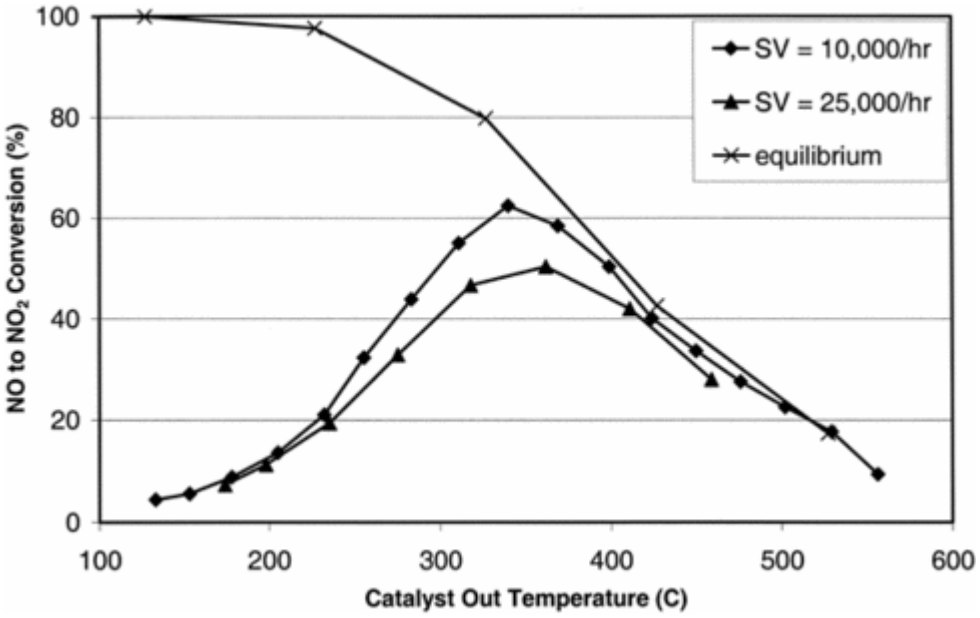

Figure 2.4: NO oxidation rates for different space velocities on the Pt/Al_2O_3. The reactant gas was composed of 8% O_2, 250 ppm NO, and a balance of N_2 [18].

The kinetics of NO oxidation reaction is affected by the choice of noble metal, metal dispersion on the surface and the choice of support material. Among the noble metals, Pt is promising metal for NO oxidation. According to experimental studies, it was shown that Rh and Pd are much less active for NO oxidation compared to Pt, but they are also much more active for NO_X reduction [20, 21, 22]. Temperature programmed oxidation (TPO) experiments of NO show that Pt based NSR catalysts reveal greater NO oxidation activity than Pd and Rh based catalysts. The effect of support material on NO oxidation activity is related to the strength of bonds between NO_X molecules and the support material. If the bond is weaker than the bond between two support molecules then any sorbed NO_X molecules can migrate rapidly to the oxidation sites on the surface and oxidation reaction occurs. Experiments focusing the support effect show that higher rates are observed in the presence of SiO_2 as a support material [23]. Moreover, the effect of noble metal dispersion on the rate of NO oxidation was studied in the literature. According to the experimental studies related to this topic, it was asserted that decrease in Pt dispersion renders increase in NO oxidation rate. This is attributed to increase in the particle size of Pt.

Since the smaller particles of Pt leads to oxide formation coincident with a decrease in activity, larger particles of Pt prevents activity losses. These activity losses are sourced by not only reduced Pt dispersion but also the effect of BaO particles. It was suggested that BaO particles bring about the activity losses either by leading to steric hinderance of Pt sites or by enhancing the formation of less reactive Pt oxides. Therefore, larger particles could limit any possible steric hindrances and Pt oxide formation. Following this argument, it was concluded that low Pt dispersion have positive effect on NO oxidation reaction opposed to the effect of Pt dispersions on most catalytic studies.

2.2.2 NO_X Storage on the Surface (NO_X trapping)

In the second step of NSR, NO_X molecules are sorbed on the alkali or alkaline earth components in the form of nitrites and nitrates. NO_X sorption or NO_X trapping refers to the process associated with extensive NO_X accumulation on the surface, due to NO_X adsorption in the form of nitrates or nitrites with the formation of ionic bonds, leading to a near complete removal of NO_X from the gas stream for appreciable periods of time [18].

As pointed out before, NO_X composition in feed gas have an influence on trapping performance. The NO_X in real engine exhaust primarily consists of NO, but active species or intermediate of sorption process are NO_2. Therefore, in order to achieve high trapping efficiency, NO oxidation activity of catalyst should be improved.

NO_X trapping process is also affected by gas compositions, temperature and catalyst compositions. In the catalyst preparation step, catalyst is exposed to the CO_2 and water in air and this exposure causes to occur phase transformations on the surface. CO_2 and H_2O react with BaO on the catalyst surface and form $BaCO_3$ and $Ba(OH)_2$ respectively. Before the reaction BaO, $Ba(OH)_2$ and $BaCO_3$ coexist at the surface. It was known that NOx storage occurs first at BaO sites, then hydroxide and finally carbonate according to rxns 2.1, 2.2 and 2.3 respectively. This storage activity

ranking is related to the basic properties of material and thermodynamic limitations the of reactions. The equilibrium constant of rxn 2.1 is greater than rxn 2.2 and the equilibrium constant of rxn 2.2 is greater than that of rxn 2.3 at the temperature window of diesel exhaust (300-400^{o}C). Phase distribution on the surface due to H_2O and CO_2 bring about also decrease in the trapping capacity since it was supposed that H_2O and CO_2 has negative influence on the stability of nitrate species on the surface. On the other hand, it was observed that O_2 increases the nitrate stability and so the trapping capacity.

$$BaO + 2NO_2 + 1/2O_2 \Leftrightarrow Ba(NO_3)_2 \quad (2.1)$$

$$Ba(OH)_2 + 2NO_2 + 1/2O_2 \Leftrightarrow Ba(NO_3)_2 + H_2O \quad (2.2)$$

$$BaCO_3 + 2NO_2 + 1/2O_2 \Leftrightarrow Ba(NO_3)_2 + CO_2 \quad (2.3)$$

NO_X trapping process reveals a volcano type dependence on the temperature (Figure 2.5 [24]). In the low temperature region, kinetic limitations of NO oxidation prevent to occur a high amount of trapping. Nonetheless, at high temperatures, the amount of NOx trapped on the surface is limited by thermodynamic stability of nitrates. Therefore, these two competing trend result in a volcano type of dependence on the temperature. Maximum trapping is observed at a temperature between 350-400^{o}C. The maximum trapping temperature was determined as 300^{o}C by Lietti *et al* [25], 350^{o}C by Mahzoul *et al* [24], 380^{o}C by Fridell *et al* [26] and 400^{o}C by Li *et al* [27].

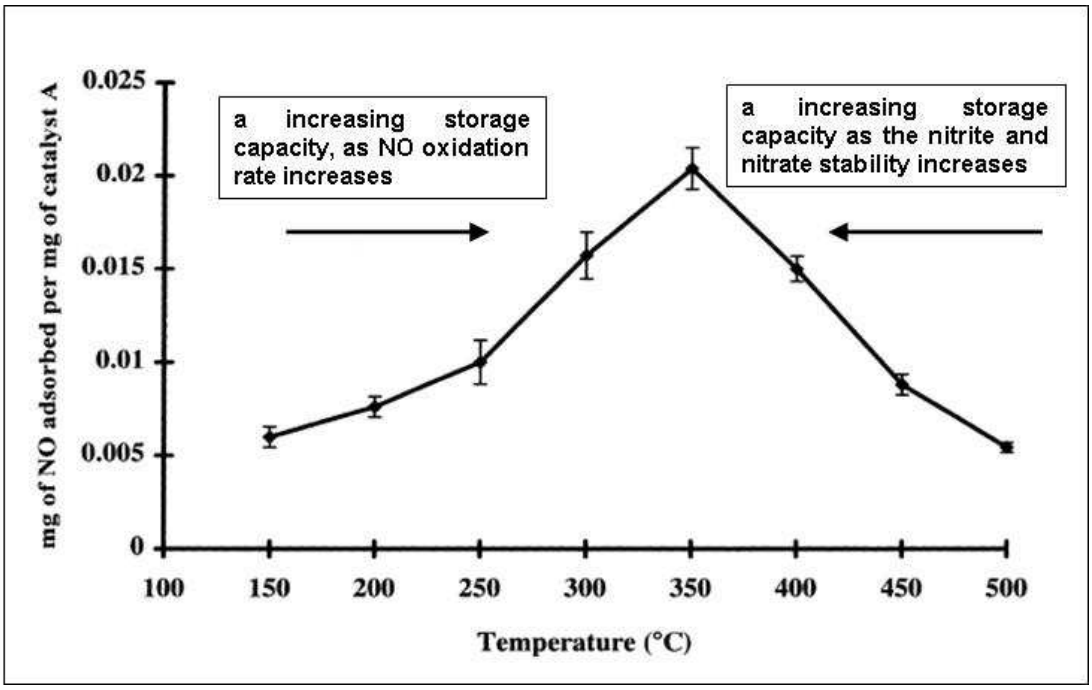

Figure 2.5: The amount of adsorbed NO with respect to temperature for Pt-Rh/Ba-La/ washcoat catalyst (catalyst A). The reactant gas was composed of 7% O_2, 500 ppm NO, and a balance of N_2 [24]

Alkali- or alkaline earth components of the catalyst have actual importance for NO_X trapping process. They provide a major contribution to the overall NO_X adsorption capacity of catalyst. The activity of alkali- or alkaline earth components is associated with their basic characters. It was demonstrated that the basicity of the component is directly related to the reaction equilibrium constants for the trapping reaction [28, 29, 30]. Thus, the sorbate component performance at 350^{o}C was found to decrease in the following order: K>Ba>Sr≥Na>Ca>Li≥Mg [18]. However, though according to this ranking K seems to be the best choice for sorbate material, experimental studies reveal that Ba shows best performance at high temperature when all NSR steps are taken into account. Also, some experiments demonstrated that the addition of alkali metal to the Ba results in higher trapping activity at high temperature. This is related to the high mobility of alkali material at high temperatures. The higher mobility of alkali material facilitates the transport of nitrate species to the barium sites and so may enhance the NO_X trapping process. On the other hand, low nitrate stability of

alkali material brings about a high NO_X release and so low NO_X reduction. Based on the nitrate stability and the ability of trapping two moles of nitrates, it was also supposed that Ba has a higher NOx trapping and reduction performance than alkali based sorbents. Also, it was observed that the addition of K to the Ba based NSR catalysts, the sorbent component performance increases.

Noble metal in catalysts also influences NO_X trapping process. The effect of noble metal is related to NO oxidation reaction and so the amount of NO_2 molecules on the catalyst surfaces. Based on the experimental evidence, Pt indicates superior performance in NO oxidation reaction compared to Pd and Rh. However, this does not necessarily suggest an influence on trapping itself, only an influence on the NO_2 amount at the surface.

Literature studies showed that phase distribution of catalytic material affects the NO_X storage activity. In the catalyst preparation step, if the catalytic material is exposed to high temperatures ((T>600^{o}C), spinel type oxides, perovskites and mixed oxides form on the surface. These structures have high stability and high temperature resistance and also do not react with CO_2. Nonetheless, since they have low surface area, the storage capacity of them is not high. In the case of applying a low temperature treatment to catalytic material during the preparation, two distinct phases belonging to the support and storage material occur on the surface and the resulting phase changes depend on the gas composition in the calcination medium. In case of chosing BaO as a storage material and alumina as a support material, Al_2O_3 and BaO phases form on the surface and if calcination is carried out in air, BaO reacts with H_2O and CO_2 to form $Ba(OH)_2$ and $BaCO_3$. In the studies of Piacentini *et al* [31, 32], barium acetate was used as precursor of BaO and the calcination was carried out in air. Three different barium containing phases have been distinguished from each other based on their crystallinity and thermal stability: (i) BaO phases being in an intimate contact with the support that are unstable and decompose already during calcination of the catalyst at 500^{o}C (ii) Low temperature $BaCO_3$ phase (LT-$BaCO_3$) well-dispersed on the catalyst surface decomposing at relatively low temperature (iii)High temperature $BaCO_3$ phase (HT-$BaCO_3$) possessing a bulk-like stability. LT-

$BaCO_3$ and HT-$BaCO_3$ phases are also called surface and bulk carbonate phases in the study of Szanyi *et al.* [33]. These three Ba-containing phases possess different reactivity for barium nitrate ($Ba(NO_3)_2$) formation. BaO phase confined to the interface with the alumina support and LT-$BaCO_3$ phase being in intimate contact with BaO are active phases for NO_X trapping, whereas HT-$BaCO_3$ phase is inactive due to high thermal stability. The relative proportion of Ba species depends on the Ba-loading. At low Ba loading (<5 wt %), the Ba-containing phase exists exclusively as BaO. At high Ba loading, as Ba loading increases, LT-$BaCO_3$ and HT-$BaCO_3$ grow on the surface respectively. Piacentini *et al.* [31] showed that if the Ba loading on the alumina support (S_g= 210 m^2/g) exceeds 5 wt %, then LT-$BaCO_3$ appers on the surface and if the loading exceeds 16 wt %, then HT-$BaCO_3$ commences to grow on the surface. The Ba phase distribution according Ba loading is shown in Figure 2.6. Moreover, in the same study it was observed that at Ba loading greater than 16 wt %, the amount of LT-$BaCO_3$ phases remains constant whereas the amount of HT-$BaCO_3$ increases proportionally to Ba loading. As shown in Figure 2.7, after 16 wt % of Ba loading, the amount of LT-$BaCO_3$ is limited to the same value, whereas bulk like HT-$BaCO_3$ grows without any limitations. The Ba loading at which the amount of LT-$BaCO_3$ phases reach the limited value is accepted as the monolayer capacity of the active barium phases. The monolayer capacity of active barium phases for alumina support (S_g=200 m^2/g) was determined as 8-10 wt % and 9.8 wt % by Fanson *et al.* [34] and Lebalme *et al.* [35] respectively. Since Ba loading greater than the monolayer capacity of the active Ba phases causes HT-$BaCO_3$ phases growing on the surface, high Ba loading results in a decrase in the trapping efficiency. Castoldi *et al*. observed [36] activity loses and by-product formation at the Ba loading exceeding monolayer capacity (10 wt % for alumina suppot having 200 m^2/g) of active Ba phases. In another study of Piacentini *et al* [37] it was observed that the Ba phase distribution is also influenced by the support material. They used SiO_2, CeO_2, ZrO_2 and Al_2O_3 as support material and observed the effect of them on the phase distribution of Ba particles for three different Ba loadings: (i) low barium loading (LBL)-4.5 wt % (ii) standard barium loading (SBL)-16.7 wt % (iii) high barium loading (HBL)-28 wt %. The resulting phase distribution is shown Table 2.1. As shown in Table 2.1, the inactive HT-$BaCO_3$ phases did not grow on the silica-

supported catalyst even at high Ba loading, the ratio of HT-$BaCO_3$ phases in Ba-containing phases is high in ceria and zirconia-supported catalyst for high Ba loading. Catalytic activities of catalysts were also evaluated for different Ba loadings. NOx storage efficiency of the catalysts are shown in Figure 2.8. As seen from figure, at Ba-loadings up to about 10 wt.% the ceria-supported catalysts show significantly higher NOx storage capacity (mg NO/mg of catalyst) than corresponding zirconia-, alumina-, and silica-supported catalysts, while at higher loading, up to about 20 wt.%, the zirconia- and alumina-supported catalysts show superior performance. Authors proposed that the high NO_X storage performance of ceria supported catalyst at low Ba loading may be attributed to its high lattice-oxygen mobility favoring adsorption of NO. They also showed that a large fraction of the HT-$BaCO_3$ is directly participating in the NO_X storage on ZrO_2-supported samples at higher Ba-loadings. They asserted this explains why zirconia-supported catalyst shows high activity at high Ba loading.

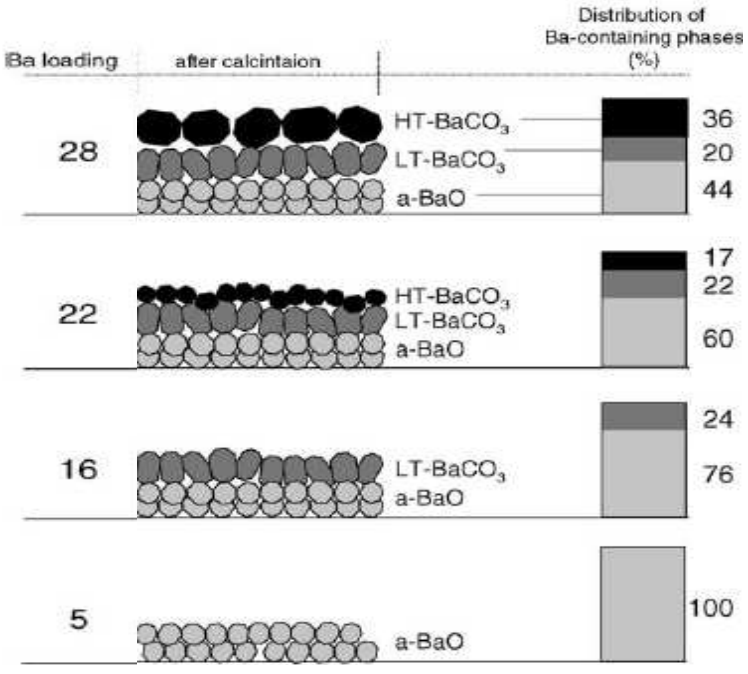

Figure 2.6: Schematic presentation illustrating the effect of Ba-loading on the distribution of Ba-containing phases [31]

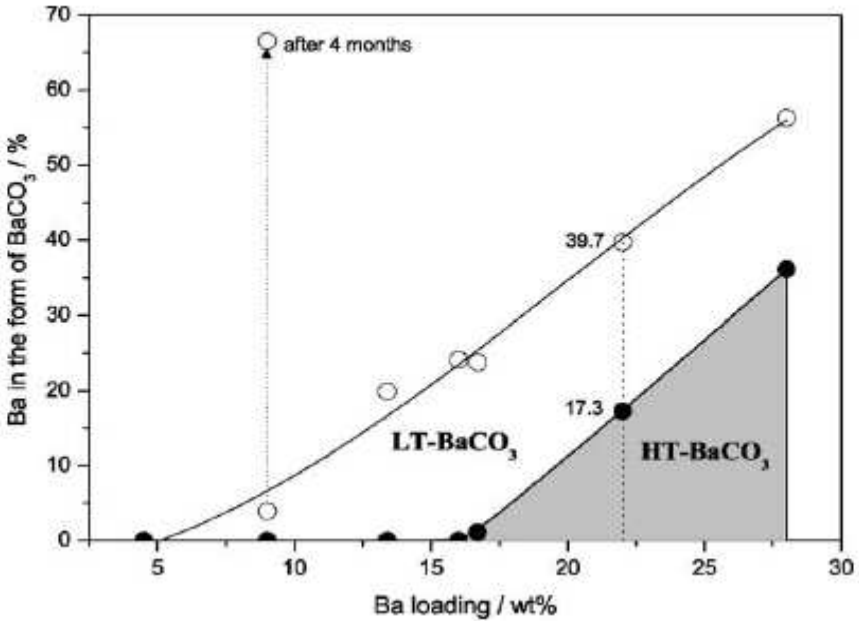

Figure 2.7: Fraction of Ba in calcined catalysts present in the form of $BaCO_3$ as a function of Ba-loading. In a sample containing e.g. 22 wt.% Ba, 39.7% exists as $BaCO_3$ (17.3% HT-$BaCO_3$, 22.4% LT-$BaCO_3$) and 60.3% of $BaCO_3$ decomposed during catalyst calcination [31]

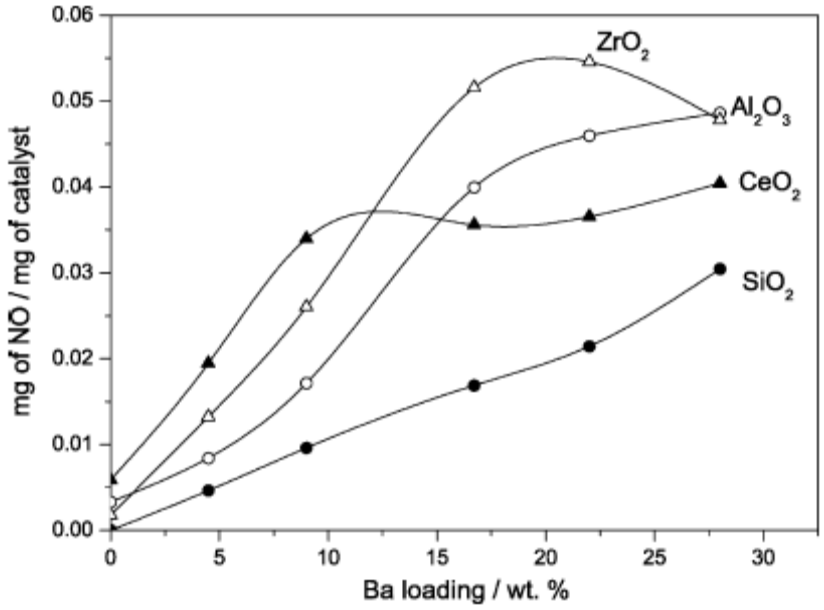

Figure 2.8: NOx storage efficiency of Al_2O_3, CeO_2, ZrO_2 and SiO_2 as a function of Ba loading [37]

Table 2.1: Relative abundance of different Ba phases (%) in Pt–Ba/MO_2 catalysts of different Ba-loading: low Ba-loading (LBL) 4.5 wt.%; standard Ba-loading (SBL) 16.7 wt.%; high Ba-loading (HBL) 28 wt.% [37]

Support	Relative abundance of Ba phases (%)		
	LBL	SBL	HBL
Al_2O_3			
BaO	100	72.5	30
LT-$BaCO_3$	0	26	25
HT-$BaCO_3$	0	1.5	45
CeO_2	59	33	26
BaO	41	27	18
LT-$BaCO_3$	0	40	56
HT-$BaCO_3$			
SiO_2			
BaO	100	100	98
LT-$BaCO_3$	0	0	2
HT-$BaCO_3$	0	0	0
ZrO_2			
BaO	58	30	24
LT-$BaCO_3$	42	35	19
HT-$BaCO_3$	0	35	57

Throughout the storage period there are two different sorption trends with respect to the time: (i) fast sorption (ii) slow sorption. As mentioned before, during the first part of storage period, fast sorption takes place and all NO_X molecules are trapped on the surface. After the fast sorption, a slow sorption period commences. The amount of NO_X trapped on the surface decreases slowly and at the end of this period all NO_X molecules pass over the catalyst without any sorption. Fast and slow sorption could also be seen in Figure 2.2 according to NO_X concentration profile as a function of time.

The reason of these two different sorption trends was investigated. Tuttlies *et al* [18] postulated that NOx storage occurs according to shrinking core mechanism. At the outer shell of Ba containing particles barium nitrate forms and particle expands due to high specific volume of nitrate molecules. This cause to form diffusion limitations

and diffusion to unreacted core through nitrate layer limits storage rate. Scholz *et al.* [38] asserted that these two sorption trends take place due to multiple storage sites sourced by phase distribution storage material (BaO, LT-$BaCO_3$, HT-$BaCO_3$). They proposed that multiple storage sites on the surface results in different sorption rates. Epling *et al.* [18] pointed out the proximity between noble metal and sorbent as the reason of fast and slow sorption. They said that sorption rate increases in case noble metal is in a close proximity to the sorbent and decreases if the noble metal is mounted far away from the sorbent.

Reaction pathway of nitrate formation is still debated in the literature. It was asserted different kinds of reaction mechanism. Epling *et al.* [18] summarized some of these reactions in the following:

- Nitrites are formed from BaO, NO, and oxygen and subsequent oxidation leads to the nitrate.

$$BaO + 2NO + O^* \rightarrow Ba(NO_2)_2 \quad (2.4)$$

$$Ba(NO_2)_2 + 2O^* \rightarrow Ba(NO_3)_2 \quad (2.5)$$

- NO_2 molecules react with the Ba species precursor and oxygen to form the nitrate.

$$BaO + 2NO_2 + O^* \rightarrow Ba(NO_3)_2 \quad (2.6)$$

- NO molecules react with the Ba species precursor and multiple oxygen atoms to form the nitrate.

$$BaO + 2NO + 3O^* \rightarrow Ba(NO_3)_2 \quad (2.7)$$

- An N_2O_4 dimer forms and reacts with the surface to form a mixture of nitrites and nitrates. The nitrites are subsequently oxidized to nitrates.

$$2NO_2 \rightarrow N_2O_4 \quad (2.8)$$

$$2BaO + N_2O_4 + 2NO_2 \rightarrow Ba(NO_3)_2 + Ba(NO_2)_2 \quad (2.9)$$

- A mixture of nitrites and nitrates are formed from NO_2 and oxygen. Again the nitrites are subsequently oxidized to nitrates.

$$2BaO + 4NO_2 \rightarrow Ba(NO_3)_2 + Ba(NO_2)_2 \quad (2.10)$$

All reactions that are listed above require a source of surface oxygen, O^*. It was supposed that there could be three types of surface oxygen sources: (i) surface or lattice oxygen associated with catalyst components (ii) O_2 in the gas stream (iii) NO_2 in the gas stream. Since it was known that surface or lattice oxygen is a transient source of oxygen, actual importance belongs to O_2 and NO_2 in the gas stream. In the literature it was proposed that when sorbent particles are in a close proximity to the noble metal, then O_2 is used for a source of surface oxygen and sorption process takes place rapidly (fast sorption). Throughout the reaction nitrite formation was also observed as intermediate, thereby, this reaction route was called nitrite route. On the other hand, if the sorbent particles are far away from the noble metal particles then NO_2 is used for surface oxygen source and the reaction takes place slowly (slow sorption). This reaction route is called nitrate route and as a result of this route disproportionation reaction occurs and one mole of NO forms. This one mole of NO differentiates nitrite and nitrate route from each other. Actually, experimental evidence shows that actual sorption process occurs at sorption material-noble metal interfaces where O_2 is used as surface oxygen source. Therefore, it may be proposed that trapping efficiency increases with increasing sorbent-noble metal interface concentration. General reactions of nitrite and nitrate route are as the following:

Nitrite Route:

$$BaO + 2NO_2 + 1/2O_2 \Leftrightarrow Ba(NO_3)_2 \quad (2.11)$$

Nitrate Route:

$$BaO + 2NO_2 \Leftrightarrow Ba(NO_3)_2 + NO \quad (2.12)$$

2.2.3 NO_X Release

Third step in NSR is the NO_X releasing step. After finishing the lean period, rich mixture is introduced to the system and catalyst is regenerated by the reductants. In the exhaust line, rich environment is created in three different ways: (i) reductants could be injected directly in the exhaust line of engine; (ii) engine may operate at rich conditions by adjusting air to fuel ratio in combustion chamber; (iii) fuel may be reformed and the resulting reductants may be sent to the entrance of catalytic part of exhaust line. After a rich pulse, a net reducing environment is created which results in oxygen consumption in the gas phase and on the surface of catalyst. As a result of oxidation of the reductant by the oxygen present in gas phase and stored on the catalyst surface, heat is generated by exothermic reactions. Both substantial decrease of partial pressure of oxygen in the gas phase and heat generated by oxidation reactions decline the nitrate stability and cause NO_X release from the surface. NO_X realeasing occurs according to the reverse reactions of rxn 2.11 or 2.12. The releasing process is followed by reduction of NO_X molecules leaving from the surface. In order to achieve high conversions, most of the released NO_X molecules should be reduced on the noble metal sites. However, in the experimental studies the release of unconverted NO_X was observed. This unconverted NO_X molecules may originate from (i) a slower reduction of the precious metal sites in comparison to the decomposition of Ba nitrate species; (ii) release from sites at the surface that are not proximal to Pt. In the study of Epling *et al.* [39] has shown that the unconverted NO_X release increases at high temperatures and this may be due to the fact that the rate of nitrate decomposition or NO_X release accelerates faster than the rate of reduction reactions. They tabulated the NO_X trapping and reduction efficiency with respect to the temperature for Pt/BaO (20)/Al_2O_3 catalyst (Table 2.2). The trapping efficiency was defined as the amount of NO_X adsorbed on the surface divided by the amount of

NO_X present in the exhaust line and the reduction efficiency was defined as the amount of NO_X reduced divided by the amount of NO_X release. As shown in Table 2.2, better reduction efficiency, higher amount of NO_X reduced per NOx release, was observed between the temperature of 300-330^oC, since the regeneration and reduction are more active at this temperature interval. At higher temperatures, less NO_X is trapped but more is released and also at low temperature high concentration of NO_X is released due to low rate of reduction reaction. Second explanation why NO_X is released is related to the noble metal-sorbent proximity. It was observed that if the sorbent is in a close proximity to the noble metal particle, then NOx molecules leaving from the surface are easily reduced or they may migrate along the surface to the noble metal site and are reduced. In order to increase overall NSR reduction efficiency reductants, which are active at low temperature, either may be utilized or nitrate stability may be increased. Also, it was shown that the rate of NO_X release is affected by the gas composition. CO_2 in the exhaust accelerates the rate of NO_X release. The effect of CO_2 is associated with the equilibrium between CO_2 and NO_2 on Ba sites. CO_2 enhances the carbonate formation and decreases the nitrate stability and causes higher NO_X release on the surface [16]. As opposed to CO_2, H_2O decreases the amount of NO_X released. Experiments about the effect of H_2O and CO_2 on NOx release demonstrated that H_2O slightly reduces the amount of NO_X released whereas CO_2 promotes NO_X release. The effect of CO_2 and H_2O is clearly observed in Figure 2.9. As seen from the Figure, in the presence of CO_2, the amount of NO_X released increases significantly. On the other hand, the addition of H_2O decreases the overall amount of NO_X released and renders two temporal regimes of release. Similar to H_2O, O_2 had a suppressive effect on NO_X release [16, 40]. It enhances the forward sorption reaction via increasing the stability of the N-bound species as nitrates. Additionally, it brings about higher amount of Pt oxide formation and so renders a readsorption by oxidizing NO molecules released from the surface. Thus, O_2 inhibits NO_X release process. The observations about the effect of gas composition are all due to equilibrium limitations at the surface of the catalyst and demonstrate the importance of including competitive species in the reactant gas stream [18]. According to the experimental studies, NO_X release problem was not solved and so

one of the important issues in NSR application is eliminating the NO_X release during the transition.

2.2.4 NOx Reduction

The final step in NSR process is NO_X reduction. In this period NO_X molecules trapped during lean period on the catalyst surface are reduced selectively to N_2. The NO_X reduction step is also present in Three-way Catalytic Converters (TWC). However, different from TWC, in the NSR applications large amounts of NO_X accumulated on the surface must be reduced in a very limited time. Therefore, high concentration of reductants should be introduced to the exhaust line in order to convert all NO_X to harmless products in a very short time. This period takes generally 20-60 seconds. There are three main factors that affect the NO_X reduction reaction: (i) type of reductant; (ii) temperature and (iii) amount of reductant.

Table 2.2: Catalyst performance in the presence of H_2O and CO_2 [39]

Temperature	NO_X Conversion (%)	NOx Storage Efficiency	Reduction Efficiency
175[a]	72.6	80.2	90.4
200[a]	85.7	91.0	94.2
225[a]	91.9	95.6	96.1
250	81.7	85.1	96.0
278	85.4	88.9	96.1
303	87.2	91.6	95.3
330	86.1	92.9	92.7
360	81.2	92.3	88.0
390	73.3	89.5	81.9
420	62.5	83.9	74.6

[a] represents data obtained from shortened sorption/regeneration cycles. Except for these data all data were obtained from 10 minutes sorption and 10 minutes regeneration)

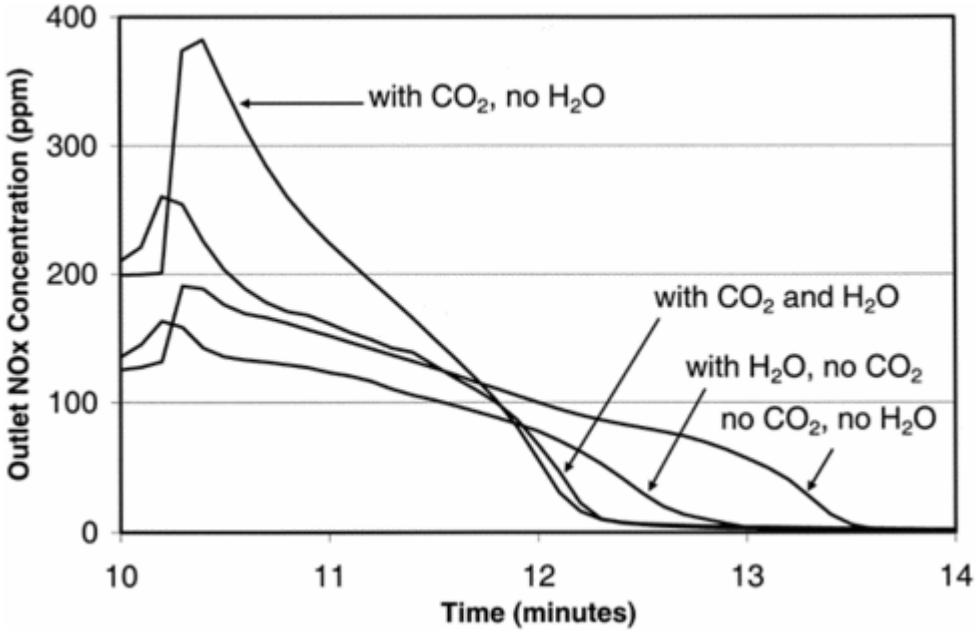

Figure 2.9: NO_X release from a $Pt/Ba/Al_2O_3$ sample at 375°C after exposure to 250 ppm NO_X, 8% O_2, and 0 or 8% H_2O, and 0 or 8% CO_2 in a balance of N_2 for 15 minutes at a space velocity of 25,000 hr^{-1}. The regeneration gas contained 1500 ppm H_2, 0 or 8% H_2O, and 0 or 8% CO_2 in a balance of N_2 for 10 minutes. Several cycles were performed until no changes were observed before this data set. The data presented were obtained from the rich/regeneration event [18]

In the literature, it was indicated that among all reductants, H_2 is the most effective. At low temperatures, the catalytic activity of H_2 is high. Propylene and CO were shown to be effective at high temperatures. On the other hand, at low temperatures, CO is not active. The inactivity of CO at low temperatures is due to the fact that CO poisons the Pt sites and so inhibits the release and reduction mechanism. In the literature, in addition to H_2, CO and propylene, diesel fuel and reformed diesel fuel were reported as reductants. Studies showed that reformed diesel fuel exhibits higher reduction performance compared to unprocessed diesel fuel. Similar results were obtained when diesel fuel, CO and CO/H_2 mixture were used as reductants. Among them, CO/H_2 demonstrated highest activity than the others. Studies related to the amount of reductants indicated that higher concentration of reductants results in more reductant delivery to the catalyst surface and this leads to higher amount of NOx reduced. The selectivity of catalyst is also very important in the NSR application,

since experiments showed that undesired products were observed during reduction. NH_3 formation was observed when H_2 was used as reductant and N_2O formation when CO was used as reductant. NH_3 and N_2O formation was also observed especially at high temperatures. NH_3 formation was observed when the H/N ratio was high [41]. Experiments related to the selectivity indicated that alkali or alkaline earth promoters which were used as sorbent material in NSR increased the selectivity. This enhanced selectivity was attributed to the weakening NO bond and so increased rate of NO dissociation which reduces the probability of N_2O formation.

The mechanisms of reduction were also debated in the literature. There are three general approaches. First approach proposed that oxidized Pt sites in the lean period are reduced by reductants and then NO_X decomposition takes place on the reduced Pt sites. Based on this approach, the particle size of Pt must be high (low dispersion) for higher activity, since smaller particles are oxidized easily. The reactions suggested by the first approach are the following when the reductants are H_2, CO and propylene [18]:

Reductant: H_2

$$H_2 + 1/2O_2 \Leftrightarrow H_2O \quad (2.13)$$

Reductant: CO

$$CO + 1/2O_2 \Leftrightarrow CO_2 \quad (2.14)$$

Reductant: C_3H_6

$$C_3H_6 + 9/2O_2 \Leftrightarrow 3CO_2 + 3H_2O \quad (2.15)$$

$$2NO \Leftrightarrow N_2 + O_2 \quad (2.16)$$

$$NO_2 \Leftrightarrow 1/2N_2 + O_2 \quad (2.17)$$

The second approach involves a direct reaction between NO_X and reductant molecules. In this case, the reactions that occur are shown below[18]:

Reductant: H_2

$$2H_2 + 2NO \Leftrightarrow N_2 + 2H_2O \quad (2.18)$$

$$2H_2 + NO_2 \Leftrightarrow N_2 + 2H_2O \quad (2.19)$$

Reductant: CO

$$CO + 2NO \Leftrightarrow N_2 + CO_2 \quad (2.20)$$

$$4CO + 2NO_2 \Leftrightarrow N_2 + 4CO_2 \quad (2.21)$$

Reductant: C_3H_6

$$2C_3H_6 + 9NO_2 \Leftrightarrow 6CO_2 + 6H_2O + 9/2N_2 \quad (2.22)$$

$$C_3H_6 + 9NO \Leftrightarrow 3CO_2 + 3H_2O + 9/2N_2 \quad (2.23)$$

Different from the first two approaches, the third one involves direct reaction between nitrate molecules and reductants. The resulting reaction is indicated below:

$$Ba(NO_3)_2 + 5H_2 \Leftrightarrow BaO + 5H_2O + N_2 \quad (2.24)$$

Based on the literature, it was mostly suggested that the actual active site is reduced Pt site and in order to retain Pt sites in the reduced form throughout the rich operation, duration of rich time and reductant concentration must high.

The type of noble metal also influences the reduction efficiency and selectivity. Based on emperical evidence, Pt and Rh exhibit better reduction activity than Pd. When NO oxidation activity was also taken into consideration, Pt is the mostly preferable candidate as a noble metal. However, the addition of Rh to NSR catalyst formulations is common due to its well-known efficiency in NO_X reduction. It is known that mixtures of the precious metals improve performance due to a better NOx reduction activity.

2.3 NSR Catalyst Formulation

In the NSR technology, in order to achieve the desired NO_X conversion, four main catalytic reactions: NO oxidation, NO_x storage, nitrate decomposition and reduction reactions, should take place. The main factor that affects the rate of reactions is the catalyst composition.

In the NSR technique, first NO is oxidized to NO_2. For oxidation reaction, precious metals represent an obvious choice due to their unparalleled red-ox activity, and Pt has been the primary oxidation catalyst choice for NSR samples [18]. It was shown that Pt is more active than Rh and Pd for NO oxidation [20, 21] and in the presence of Pt catalyst NO_2 level almost reaches the equilibrium value of 50 % at 400^oC [22]. The amount of NO_X stored on the surface increases with increasing oxidation rate and so increasing the amount of Pt in the catalyst composition. However, it was seen that the NO_X storage efficiency did not increase indefinitely with the Pt loading. The Pt loading at a given temperature of operation is optimal when the rate of NO oxidation to NO_2 is nearly equal to the NO_2 adsorption rate at the sorbent sites. Optimum Pt loading depends on the surface area of catalyst, catalyst composition and Pt dispersion and so it should be determined experimentally for each catalyst. Actually, there are two kinds of Pt sites on the surface. Sites far away from sorbent material trigger NO oxidation reaction as mentioned. On the other hand, other sites close to sorbent are active for the storage of NO_X in nitrate or nitrite form. In other words, sites far away from the sorbent material are mainly not responsible for the NO_X trapping reaction due to surface diffusion limitations [18, 24]. Actual importance for NO_X trapping belongs to adjacent sites to sorbent material. Therefore, in order to attain high NO_X trapping performance sites close to the sorbent material should be increased. This might be possible by increasing Pt and sorbent dispersion together.

After oxidation reaction, NO_2 is adsorbed on the surface and stored on the storage material in the form of nitrite or nitrate. Storage material should have basic properties to attract acidic NOx molecules and its performance increases with

increase in its basic character. Thermodynamic evaluation and reaction data in the literature demonstrated that the basicity of the component is directly related to the calculated reaction equilibrium constants for the trapping reaction [18 and references therein]. Taking into consideration the equilibrium constants, potassium is the most promosing sorbent material for trapping. Nonetheless, some experimental evidence showed that Ba is more active than K for overall NSR efficiency [18 and references therein]. The reason for the activity difference was related to the nitrate stability of barium which is high at high temperatures compared to K and so lower amount of NO_X is released without reacting in the presence of Ba. Though there was discrepancy about stability of K and Ba nitrates in the literature, it was known that bulk nitrate of potassium decomposes at lower temperatures (400^oC in air) than that of Ba (590^oC in air). However, the decomposition temperature also depends on the phases on the surface in the presence of Ba and K. The sorbent loading also has an influence on NO_X storage efficiency. The higher loadings result in higher amounts of NO_X stored on the surface. However, it was shown that when the loading exceeds a limiting value, the increase in sorbent loading decreases NO_X storage. This limiting value is called the monolayer capacity of active phases of storage material. If the sorbent material loading exceeds the monolayer capacity of active phases, then an inactive phase occurs on the surface and the high amount of sorbent material causes steric hinderance and so decreasing Pt dispersion [13]. Therefore, there is also an optimum value for loading of sorbent material to achieve as high as possible NOx storage on the surface and it depends on the surface area of support material and support-sorbent interaction. Active and inactive phase ratio on the surface and NO_X storage activity changes depending on the interaction. The properties of support material also affect the NO_X storage efficiency. It was demonstrated that Al_2O_3-supported catalysts exhibits low amount of inactive bulk-like barium phase compared to ZrO_2- and CeO_2-supported catalysts. It is reasonable to expect that Al_2O_3-supported catalysts exhibits higher NO_X storage activity than ZrO_2- and CeO_2-supported catalyst. However, as mentioned before, CeO_2-supported catalyst showed highest activity at low Ba loading due to high mobility of lattice oxygen and ZrO_2-supported catalyst exhibited highest activity at high Ba loading due to low stability of its inactive Ba containing phase (Figure 2.9). In addition, since the support material

influences surface migration velocity of NO and NO_2 molecules, it affects the kinetics of NO oxidation and NO_X sorption process.

At the end of lean period, as the catalyst reaches the saturation point, then the NSR catalyst undergoes pulse-like atmospheric change from oxidizing to reducing conditions. The intermittent shift of the medium brings about the NO_X release from the surface and some amount of unconverted NO_X is released to the atmosphere. This unconverted NO_X release is attributed to a faster nitrate decomposition than NO_X reduction. This problem can be solved by either increasing nitrate stability or increasing NO_X reduction rate. In order to increase the nitrate stability, alkali or alkaline earth material having high nitrate stability could be added to the catalyst composition in order to decrease the amount of NO_X released. In order to increase NO_X reduction rate, Rh could be added to the catalyst composition in addition to Pt. Utilization of both of them provides higher NO_X reduction efficiency by decreasing the amount of unconverted NO_X release.

2.4 Lean/Rich Cycling (Storage and Regeneration Period)

NSR is a dynamic phenomenon, where the balance of lean and rich timing is vitally important in determining the overall efficiency of NO_X removal [42]. During the lean period, NO is oxidized to NO_2 and is trapped on the surface. When the surface is saturated, exhaust atmosphere is shifted from lean to rich. In the rich duration, reductant is introduced to system and surface is regenerated completely. Therefore, lean and rich durations depend on the storage capacity of the surface and regeneration time, respectively. The effect of lean/rich duration on NO_X trapping and reduction performance was investigated by Li *et al*. [42]. In the experiments, authors studied the effect of duration time by keeping rich duration constant. They observed that the increase in lean duration results in a decrease in NO_X conversion. As seen from Figure 2.10, NO_X conversion decreases substantially by changing the lean duration from 45 s to 135 s. The reason of related decrease is that the rich duration is not long enough to recover all NO_X trapped on the surface during the high lean

duration. Therefore, the average NO_X conversion obtained from integration through all repeating lean/rich cycles declined from 93% (for 45 s lean) to 40% (for 135 s lean). In the same study, the authors also investigated the effect of rich duration for fixed lean duration. It was shown that NO_X conversion increases as increasing the rich duration (Figure 2.11). The average NO_X conversion rises from 41% (for 1.5 s rich) to 98% (for 4.5 s rich). In the same study, the NO_X conversion dependency on the L/R ratio (lean/rich duration ratio) was illustrated. As shown from Figure 2.12, NO_X conversion increases with decreasing L/R ratio. On the same figure, the NOx conversion value as a function of L/R at a temperature of 250^oC is shown. At 250^oC, NOx conversion increases with decreasing the L/R ratio at a lower rate. The reason is related to kinetic limitations of the oxidation and reduction reactions. If the oxidation and reduction are limiting, then the catalyst does not trap NO_X molecules fast enough and the surface is not effectively regenerated. Therefore the NO_X conversion vs L/R ratio line is less steep at low temperature at which kinetic limitations are present. On the other hand, it is reasonable to expect that at high temperatures, the same line should be steeper compared to the line obtained at 300 ^oC. Since, nitrate stability decreases at high temperatures, trapping becomes sensitive to the lean duration and the NOx conversion becomes less dependent on the L/R ratio [42].

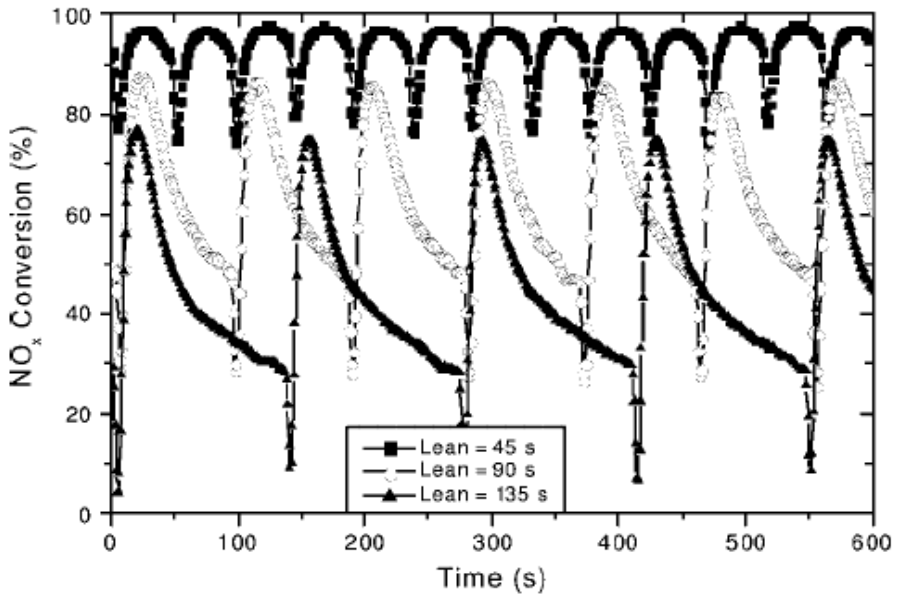

Figure 2.10: NOx conversion over an aged NOx trap as a function of lean trapping duration while holding rich timing constant at 1.5 s. Catalyst was prepared by washcoating Pt (1.7 wt%), Rh (0.3 wt%), Ba (12.6 wt%) and Al_2O_3 on ceramic monolith. Lean feed consists of 200 ppm NO, 10% O2, 10% H_2O in N_2, while the rich feed contains 3% CO, 200 ppm NO and 0% O2 in N_2. Experiments were carried out at 300^oC [42].

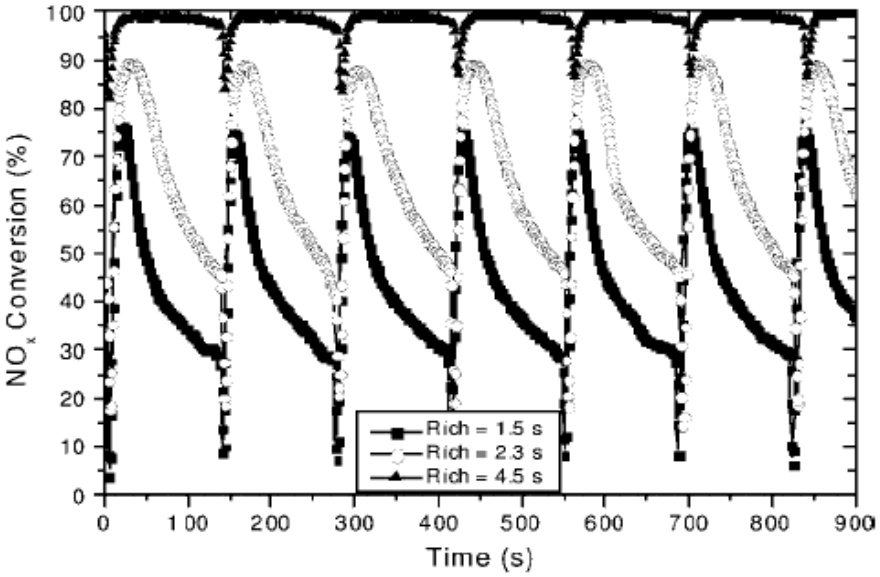

Figure 2.11: NOx conversion as a function of rich pulse duration with a constant lean trapping time (135 s). Catalyst was prepared by washcoating Pt (1.7 wt%), Rh (0.3 wt%), Ba (12.6 wt%) and Al_2O_3 on ceramic monolith. Lean feed consists of 200 ppm NO, 10% O2, 10% H_2O in N_2, while the rich feed contains 3% CO, 200 ppm NO and 0% O2 in N_2. Experiments were carried out at 300^{o}C [42].

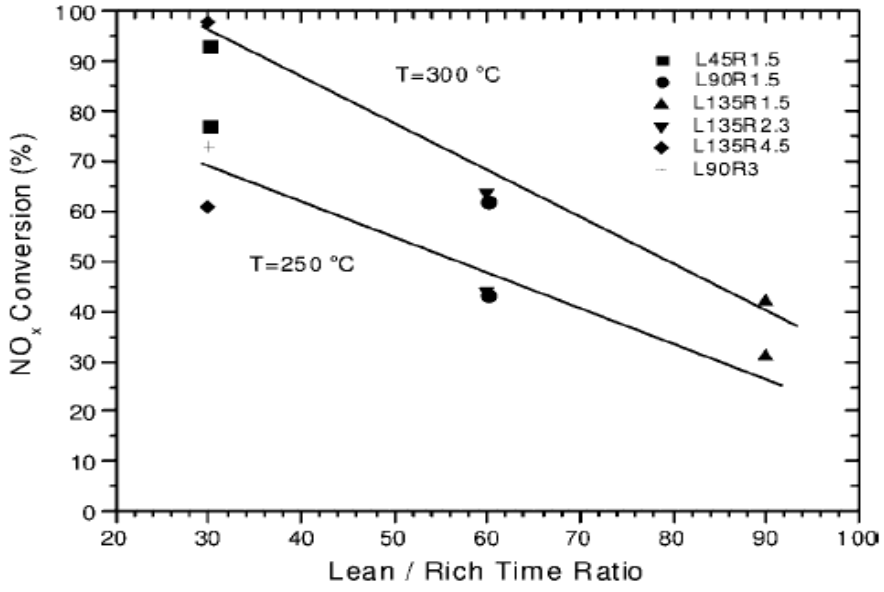

Figure 2.12: NOx conversion as a function of lean/rich ratio and temperature.
*The symbol L and R with numbers represents lean and rich duration time [42].

CHAPTER 3

THERMODYNAMICS

NOx storage and reduction technique is composed of two sequential periods: (i) storage (NOx trap) period (ii) regeneration (reduction) period. As mentioned in previous sections, there are four different reactions taking place during these periods: two in the storage period and two in the regeneration period. In this part, reactions are analyzed thermodynamically for storage and regeneration periods separately.

3.1 Storage Period

During the storage period, engine runs under lean conditions and exhaust contains excess oxygen, NO_X and low amount of HC and CO relative to NO_X. NO_X primarily consists of NO. NO_2 is active compound for NOx storage reaction, so first NO should be oxidized to NO_2. After oxidation reaction, NO_2 is converted to surface nitrate based on two different reaction pathways: (i) nitrite route (ii) nitrate route.

The NO oxidation reaction and surface nitration reactions according to nitrite and nitrate route respectively are given below:

$$NO + 1/2O_2 \Leftrightarrow NO_2 \tag{3.1}$$

$$BaO + 2NO_2 + 1/2O_2 \Leftrightarrow Ba(NO_3)_2 \tag{3.2}$$

$$BaO + 3NO_2 \Leftrightarrow Ba(NO_3)_2 + NO \qquad (3.3)$$

The enthalpy and Gibbs free energy changes of the reactions are presented in Table 3.1. Equilibrium constants of each reaction at different temperature were calculated by using Van't Hoff Equation (It was assumed that $\Delta C_p=0$). Initial mole fractions of NO and O_2 were taken 0.001 and 0.1 consistent with our flow reaction study. Taking into consideration that NO oxidation and surface nitration reactions take place at the same time, the extents of the reactions of oxidation and nitration were calculated simultaneously (The calculation procedures are shown in Appendix A.1 in detail). The calculations were made by using Mathlab Program (The code of program is given in Appendix B). Equilibrium conversions of the reactions were calculated by using the extents of reactions. Equilibrium conversion values of oxidation and nitration reactions at different temperatures are shown in Figure 3.1 and 3.2 for nitrite and nitrate reaction pathway respectively.

Table 3.1: The enthalpy and gibbs free energy changes of NO oxidation and surface nitration reactions at standard state (25 ^oC, 1 atm)

Reaction		$\Delta H°$ (kJ/mol)	$\Delta G°$ (kJ/mol)
3.1	$NO + ½\ O_2 \rightarrow NO_2$	-57.1	-35.4
3.2	$BaO + 2NO_2 + ½\ O_2 \rightarrow Ba(NO_3)_2$	-505.0	-373.9
3.3	$BaO + 3NO_2 \rightarrow Ba(NO_3)_2 + NO$	-447.9	-338.5

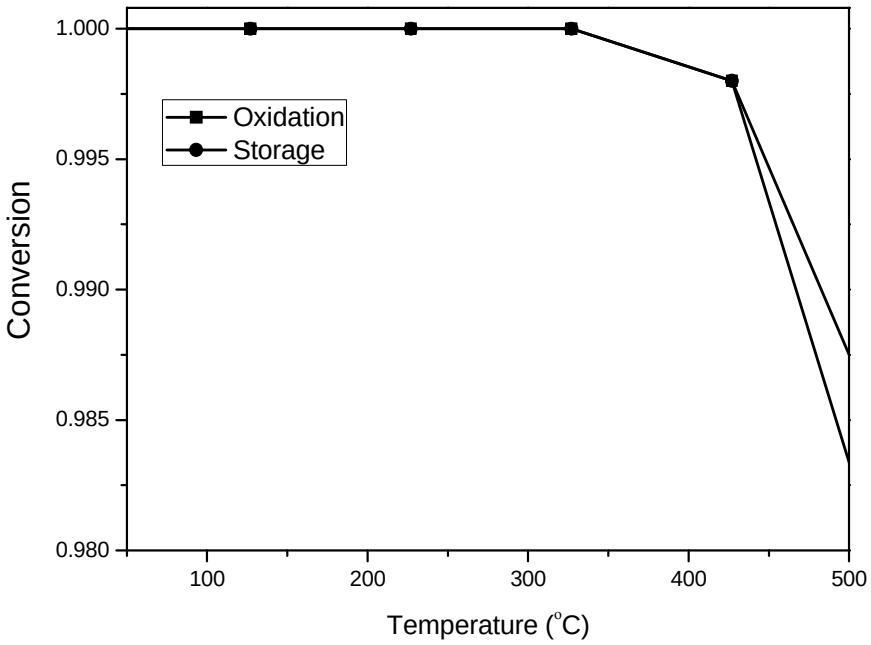

Figure 3.1: Equilibrium conversion values of oxidation and nitration reaction with respect to temperature for nitrite route

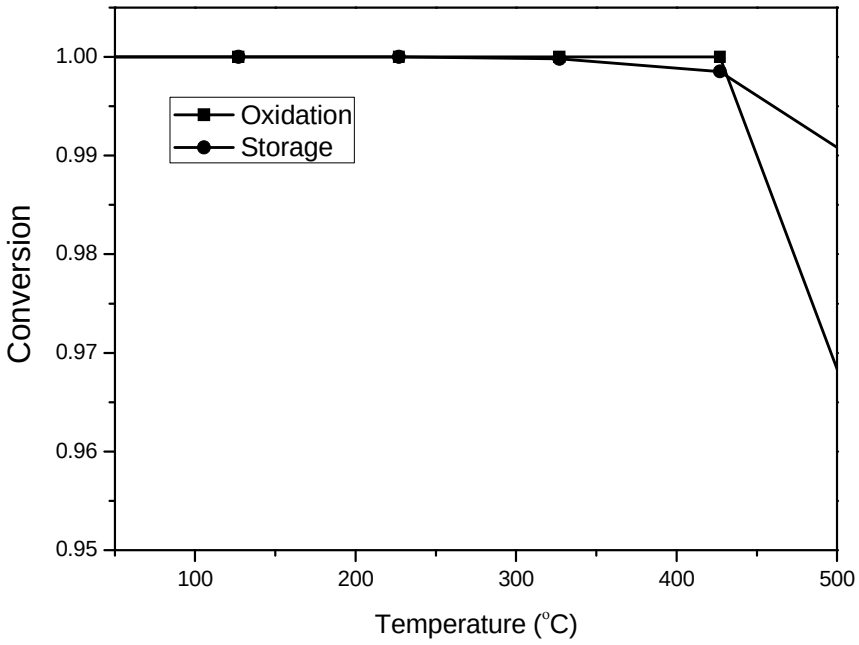

Figure 3.2: Equilibrium conversion values of oxidation and nitration reaction with respect to temperature for nitrate route

3.2 Regeneration Period

At the end of the storage period, gas composition is shifted from lean to rich. Since the gas composition is reductant rich, the partial pressure of oxygen approaches to 0 and barium nitrate that forms in the oxygen excess medium decomposes to NO_2 and NO. In case H_2 is taken as reductant and NO_2, NO and O_2 nitrate decomposition products and taking in to consideration the dependency of reactions, then the reactions taking place in the regeneration period would be given by following:

$$H_2 + 1/2O_2 \Leftrightarrow H_2O \tag{3.4}$$

$$NO_2 + H_2 \Leftrightarrow NO + H_2O \tag{3.5}$$

$$NO + H_2 \Leftrightarrow 1/2N_2 + H_2O \tag{3.6}$$

At standard state, the enthalpy and Gibbs free energy changes of these reactions are presented in Table 3.2. Equilibrium constants were also calculated by using Van't Hoff Equation (It was assumed that $\Delta C_p=0$) and by using equilibrium constants the extent of reactions were calculated. During the calculation some assumptions were made: (i) surface nitrate decomposes according to the reverse reaction of nitrate formation by nitrite route; (ii) All nitrates on the surface are converted to NO_2 and O_2 with a constant rate throughout the regeneration period; (iii) The gas molar flow rate of rich gas composition is taken to be consistent with our flow reaction study. The calculation procedure and program code using for the calculation are presented in Appendix A.2 and B.2 respectively. The Equilibrium conversions of each reaction with respect to temperature are shown in Figure 3.3.

Table 3.2: The enthalpy and Gibbs free energy changes of regeneration reactions at standard state (25 ^{o}C, 1 atm)

Reaction		ΔH° (kJ/mol)	ΔG° (kJ/mol)
3.4	$H_2 + ½ O_2 \rightarrow H_2O$	-241.8	-228.6
3.5	$NO_2 + H_2 \rightarrow NO + H_2O$	-184.7	-193.2
3.6	$NO + H_2 \rightarrow ½ N_2 + H_2O$	-332.1	-315.2

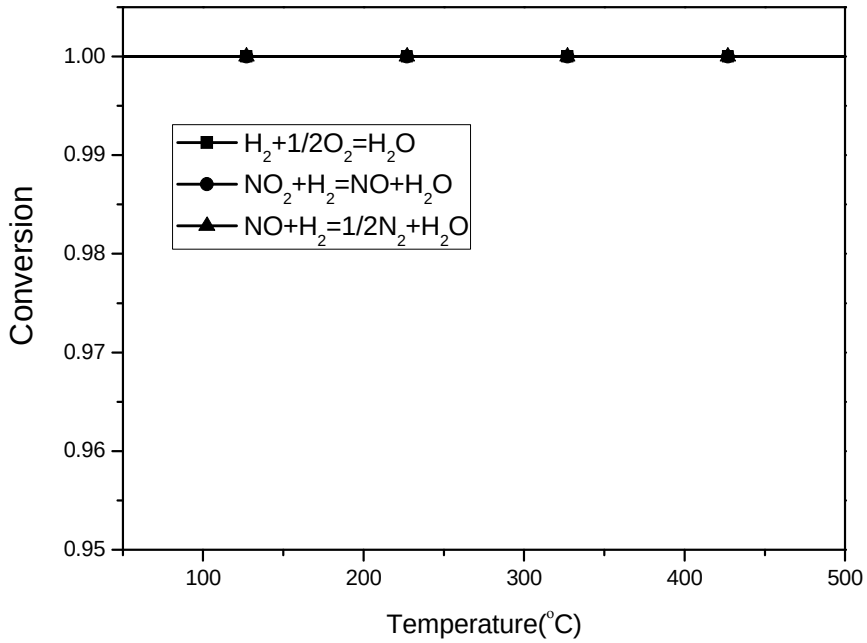

Figure 3.3: Equilibrium conversion values of reaction 3.4, 3.5 and 3.6 with respect to temperature

CHAPTER 4

EXPERIMENTAL

4.1 Catalyst Preparation

Cerium-zirconium mixed oxides ($Ce_xZr_{1-x}O_2$) used as support materials for NO_X Storage and Reduction (NSR) catalysts were prepared by the Pechini method which is a sol-gel like method based on mixing the related mixed oxide precursors with an α-hydroxy carboxylic acid and then barium and platinum were loaded on the supports via incipient wetness impregnation.

4.1.1 Preparation of Mixed Oxide

Pure ceria, pure zirconia and cerium-zirconium mixed oxide ($Ce_xZr_{1-x}O_2$) with different Ce and Zr contents (x=0.25, 0.5, 0.75) were prepared by Pechini method. Pechini method is a sol-gel like method and is based on mixing the related mixed oxide precursors with an α-hydroxy carboxylic acid. After mixing, around the metal cations complex ring-shaped compounds form in the solution. A polyhydroxyalcohol is then added and the solution is heated to 150-250^oC to form large cross-linked network. After removing the excess water, a solid polymeric resin results. At high temperature, the resin is decomposed and the mixed oxide is obtained [43-46].

In order to prepare mixed oxides and pure ceria and zirconia, $Ce(C_2H_3O_2)_3.1.5H_2O$ (cerium acetate) and $ZrOCl_2.8H_2O$ (zirconium oxychloride) were used as Ce and Zr

source respectively. Citric acid ($C_7H_8O_7.H_2O$) was used as α-hydroxy carboxylic acid and ethylene glycol ($C_2H_6O_2$) was selected as polyhroxyalcohol. The equal molar quantities of citric acid and ethylene glycol were added into the mixed solution of the desired amount of cerium acetate and zirconium oxychloride where the molar ratio citric acid to anions was 1:1. Aqueous solution of NH_3 was utilized to adjust the pH value at 6. The mixture was stirred at 50^oC for half an hour and calcined at 500^oC for 2 h. By following this procedure, CeO_2, $Ce_{0.25}Zr_{0.75}O_2$, $Ce_{0.5}Zr_{0.5}O_2$, $Ce_{0.25}Zr_{0.75}O_2$ and ZrO_2 powders were obtained.

4.1.2 Preparation of NSR Catalysts

In order to obtain final desired Pt/BaO/$Ce_xZr_{1-x}O_2$ (x=0, 0.25, 0.5, 0.75, 1) catalysts, barium and platinum were added sequentially on to the prepared ceria, zirconia and mixed oxide supports via incipient wetness impregnation. In incipient wetness impregnation technique, oxide precursors are dissolved in just sufficient solvent to cover the surface of the support. The support was then impregnated with this solution. Then, the slurry is dried at 100-120^oC to remove the excess water. Finally, the dried sample is calcined to stabilize the surface area, the pore structure and the crystalline phase and to remove unwanted ligands originating from the metal precursors [47, 48].

In the experiments, $BaCl_2.2H_2O$ (barium chloride dihyride) and $Pt(NH_3)_4Cl_2.H_2O$ (tetraamine platinum chloride) were used as Ba and Pt precursors, respectively. First, the support material was impregnated with the Ba containing solution. Barium chloride dihyride was dissolved in water having a volume equal to the pore volume of support material. The amount of barium chloride dihyride was determined in such a way that the weight percentage of BaO in the final product was 10% with respect to support material. After the impregnation, the sample was dried at 120^oC overnight and calcined in air at 500^oC for 2h. After Ba doping of the support surface, Pt was loaded by repeating the same procedure so as to yield 1 wt % Pt in the final product. The Pt/BaO/Al_2O_3 with a similar Ba and Pt composition was used as a reference

sample for the activity measurements. The phase of alumina is corundum (ICDD Card No: 10-0173).

4.2 Catalyst Characterization

4.2.1 X-Ray Diffraction (XRD) Analysis

The $Ce_xZr_{1-x}O_2$ (x=0, 0.25, 0.5, 0.75, 1) powders prepared by Pechini Method were characterized by XRD. XRD data were obtained by Rigaku X-ray diffractometer (30 kV, 15 mA) with a miniflex counter using a Cu Kα radiation (λ=1.54 Å). The diffraction pattern was collected in the 2θ range of 10–80° at a scanning rate of 1° min^{-1} in steps of 0.05° and was analyzed by Powder Diffraction File database (International Centre for Diffraction Data).

4.2.2 Surface Area, Pore Size Distribution and Adsorption-Desorption Isotherms

After Ba and Pt loading, the surface area and pore size distribution of the resulting powder catalysts were determined by Micromeritics ASAP 2000 gas sorption and porosimetry system. Prior to the experiment, the sample was degassed at 120°C for 12 h under the vacuum environment to desorb all gas molecules on the surface. The degassing process was carried out in a vacuum oven. Nitrogen was utilized as inert gas and the surface area of samples were measured using nitrogen adsorption isotherms at 77 K. Surface areas were calculated by the BET (Brunauer-Emmett-Teller) method and the pore size distributions were determined by using the BJH (Barrett-Joyner-Halenda) method**.**

4.2.3 Temperature Programmed Reduction (TPR) Analysis

Reducibility of resulting catalyst surfaces was determined by H_2 temperature programmed reduction (TPR) study. TPR experiments were performed by a home

built system using a fixed bed pyrex glass reactor (D= 4 mm, L= 60 cm) and for all experiments 50 mg of catalyst was used. 5 % H_2/He gas mixture was fed to the reactor throughout the experiments and the temperature was increased at a constant rate of 10^{o}C/min from room temperature to 500^{o}C. A temperature controlled tube oven (Protherm-PTF 12/70/450) was utilized and all gas flows were metered by mass flow controllers (MKS 1179 B). During the experiments, total volumetric flow rate and space velocity were 35 cm^3/min (sccm) which corresponds to 8300 h^{-1}. The outlet H_2 concentrations were recorded online by means of a Quadrupole Mass spectrometer (Pfeifer QMS 200).

4.2.4 CO Chemisorption

The surface sites of the catalysts were characterized via chemisorption experiments with CO used as a probe molecule. CO chemisorption experiments were conducted in a gas manifold system attached to a DRIFTS reaction cell. All DRIFTS spectra were recorded by Perkin Elmer Spectrum 100 DRIFT Spectrometer combined with a Pike reaction cell and the temperature of reaction cell was adjusted by a Pike Temperature Control Unit. All spectra were recorded with 4 cm^{-1} resolution in the range of 4000-400 cm^{-1} using a liquid nitrogen cooled MCT detector and scan number was selected as 128 in order to increase signal to noise ratio.

Experimental setup is shown in Figure 4.1. Feed gas (He, H_2, O_2 and CO) lines were connected to a gas manifold and the outflow of manifold was attached to the reaction cell. Also, the outflow of reaction cell is closed by a plug (batch system) in order to be able to carry out volumetric chemisorption experiments. All of the experiments were performed in such a way that firstly desired gas composition was accumulated in the manifold and then sent to the reaction cell. In the experiments, 50 mg sample was used for alumina containing catalyst, 45 mg for ceria containing and 25 mg for the others.

Prior to the CO chemisorption experiments, the following pretreatment procedure was performed. First, the sample was outgassed at room temperature for 20 min at a pressure of 10^{-6} torr. Then, H_2 treatment was carried out three times at 200^{o}C for 20 min and between each H_2 treatment, the system was evacuated. Finally, the system was outgassed at the same temperature and cooled to 50^{o}C. After the pretreatment, background spectra were recorded and CO isotherm data were collected together with DRIFTS spectra at 50^{o}C in the range of 0-50 mm Hg.

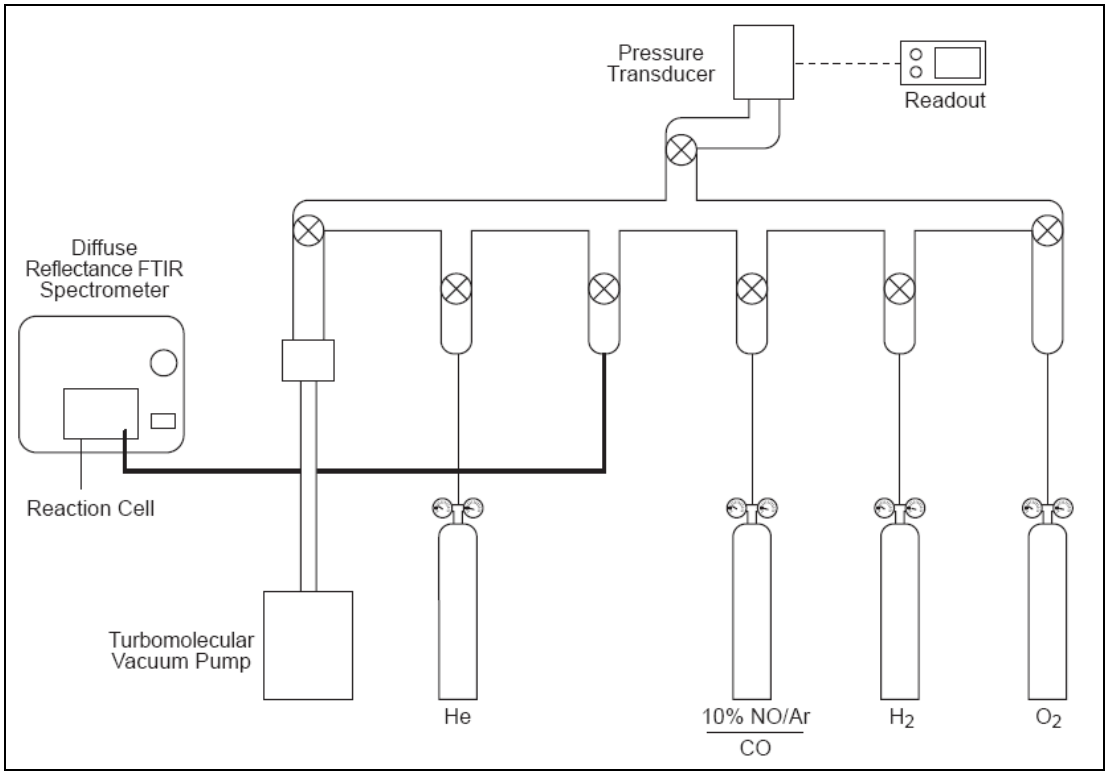

Figure 4.1: Gas Handling Manifold, FT-IR and DRIFTS attachment set-up

4.2.5 In-situ DRIFT spectroscopic study of NO_X Storage process

Surface species forming on the catalysts surfaces throughout the NO_X storage period were analyzed by means of in-situ DRIFTS. Experiments were conducted in the same experimental setup used for CO chemisorption experiments (Figure 4.1).

Unlike the CO chemisorption experiments, 10% NO-Ar gas line was connected to the manifold instead of CO. DRIFT spectra were recorded with 4 cm^{-1} resolution in the range of 4000-400 cm^{-1} using a liquid nitrogen cooled MCT detector and scan number was selected as 128 similar to CO chemisorption experiments. In the experiments, 50 mg sample was used for alumina containing catalyst, 45 mg for ceria containing and 25 mg for the others.

Before the experiment, the samples were pretreated. The sample was outgassed at room temperature for 20 min at a pressure of 10^{-6} torr. Then H_2 treatment was carried out at 200^oC for 20 min. After surface reduction, NO/Ar/O_2 1:10:100 mixtures were fed to the cell to remove carbonates and hydroxides on the surface of the sample at 200^oC. H_2 treatment at 200^oC was repeated once more for 20 min and the surface of the sample was activated in O_2 environment at the same temperature for 20 min. Finally, the manifold and the reaction cell were outgassed and cooled to room temperature under vacuum. Between each stage of pretreatment process, manifold and reaction cell were evacuated.

After applying the pretreatment procedure, background spectra was recorded at room temperature. Then, DRIFTS spectra were recorded after admission 10% NO-Ar gas mixture in the range of 0-1000 mm Hg.

In the experiments, the reducibility of nitrates on the surface was also investigated. After volumetric chemisorption, manifold and reaction cell were outgassed for a while and then H_2 treatment was performed at 300^oC.

4.3 Reaction Tests

The catalytic activities of the samples were tested in our home-built transient reaction system. The setup of the reaction system is shown in Figure 4.2. As seen in the figure, our experimental setup consists of a gas supply system, reaction system and analyzer. Gas supply system uses four gas cylinders (Ar, O_2, H_2 and 10% NO/N_2)

and mass flow controllers (MKS 1179 B). The flow of the four gas streams were controlled by mass flow controllers. In order to accomplish lean and rich experiments sequentially, a four port dual actuated switching valve (Swagelok-MS 142 ACE) was used and controlled by a control panel. Our reaction system is composed of a pyrex glass reactor and a temperature controlled tube oven (Protherm-PTF 12/70/450). The length and inner diameter of reactor are 60 cm and 4 mm, respectively. The composition of outlet gas stream was determined by a Quadrupole Mass spectrometer (Pfeifer QMS 200).

Prior to NO_x storage and reduction (NSR) experiments, all catalysts were pre-reduced at 500^{o}C in 5% H_2 environment for 2 h. After the pretreatment, storage and reduction experiments were conducted with periodic switch of gases between the compositions of 10 % oxygen, 1000 ppm NO for lean and 1100 ppm NO, 10000 ppm H2 for rich conditions. The gas composition data for three lean-rich cycles were collected on-line by mass spectrometer. The first two lean-rich cycle were considered as surface activation period and the data obtained in the third lean-rich cycle was taken as actual data. NO (m/e=30), NO_2 (m/e=46), N_2 (m/e=28), H_2 (m/e=2), NH_3 (m/e=17) and O_2 (m/e=32) were recorded during experiments. The volumetric flow rates of gases were 171 and 137 sccm and the space velocities were 41000 and 37000 h^{-1} for lean and rich period, respectively. All of the tests were carried out at 350^{o}C. The lean and rich operation time was selected as 10 and 15 min respectively to observe NOx concentration trends clearly. Furthermore, 50 mg sample was used for each experiment.

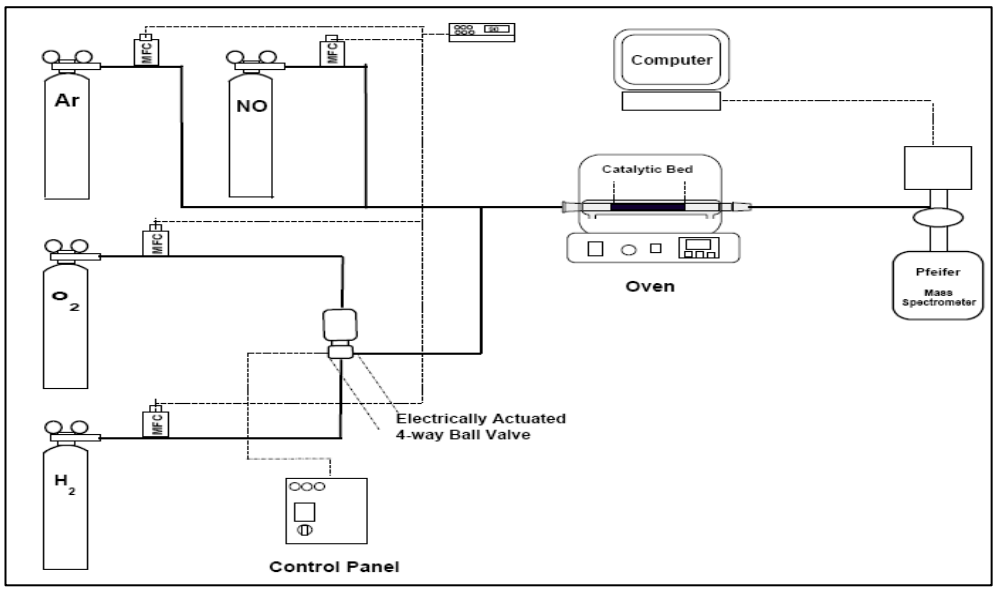

Figure 4.2: Experimental Setup of NSR reaction experiments

CHAPTER 5

RESULTS AND DISCUSSION

5.1 XRD Analysis

The X-Ray diffraction patterns of prepared $Ce_xZr_{1-x}O_2$ (x= 0, 0.25, 0.5, 0.75, 1) mixed oxide powders are shown in Figure 5.1. As seen in the figure, all samples except for pure zirconia exhibit single phase crystalline formation. The diffraction lines of CeO_2 and $Ce_{0.75}Zr_{0.25}O_2$ show the presence of cubic fluorite structure and $Ce_{0.5}Zr_{0.5}O_2$ and $Ce_{0.25}Zr_{0.75}O_2$ indicate tetragonal phase. In $Ce_xZr_{1-x}O_2$ (x=0.25, 0.5, 0.75) mixed oxide samples, there are no extra peaks corresponding to pure ceria and zirconia. This suggests that Ce and Zr ions are homogeneously distributed in the prepared samples. Furthermore, Figure 5.1 shows that diffraction peaks are shifted to higher values with increasing Zr content in the samples. This is attributed to lattice shrinkage due to the replacement of Ce^{+4} with smaller cation Zr^{+4} [49, 50, 51 and references therein]. A mixture of two phases was only observed in the presence of ZrO_2 sample. It indicates monoclinic phase along with tetragonal phase in conjuction with the literature [50].

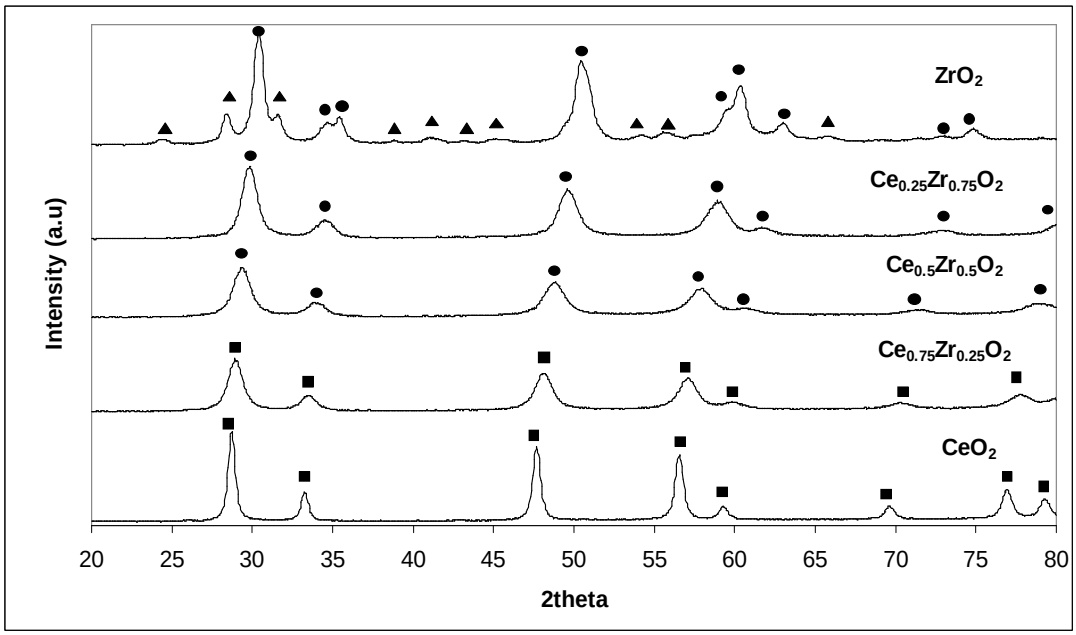

Figure 5.1: X-ray diffraction data of Ce-Zr mixed oxides prepared by Pechini Method and calcined at 500 ^{o}C (■ cubic phase, ● tetragonal phase, ▲ monoclinic phase)

5.2. Surface Area, Pore Size Distribution and Adsorption-Desorption Isotherms

The BET surface areas and structural parameters obtained from BET analysis are given in Table 5.1. The BET surface area of Pt/BaO/Al_2O_3 is 33.4 m^2/g. Since it has higher average pore radius, the highest pore volume makes its surface area high among the others. Pt/BaO/CeO_2 has highest average pore diameter. This can be due to larger atomic radii of Ce^{+4} cation than the Zr^{+4} and Al^{+3}. Pt/BaO/ZrO_2 has lowest pore volume and pore diameter in the same range with alumina. Thus, the lowest surface area belongs to Pt/BaO/ZrO_2. The mixed oxide supported catalysts exhibit different characteristics from ceria and zirconia supported catalyst. They have low pore diameter and so higher surface area than the others. They also have narrower pore size distribution than the pure ceria, zirconia and alumina supported catalysts, as shown in Figure 5.2. Pore diameters of Pt/BaO/$Ce_{0.5}Zr_{0.5}O_2$ and Pt/BaO/$Ce_{0.25}Zr_{0.75}O_2$ are in between 18 and 100 Å whereas pore diameters of

$Pt/BaO/Ce_{0.5}Zr_{0.5}O_2$ are in between 18 and 150 Å. Among the mixed oxide supported catalysts, $Pt/BaO/Ce_{0.5}Zr_{0.5}O_2$ and $Pt/BaO/Ce_{0.75}Zr_{0.25}O_2$ catalysts indicate highest BET surface area and $Pt/BaO/Ce_{0.25}Zr_{0.75}O_2$ catalyst shows lowest BET surface area.

Table 5.1: BET surface area, BET single point total volume of pores and average pore diameters of NSR catalysts

Catalyst	BET Surface Area (m^2/g)	Avarage Pore Diameter (A)	Pore Volume (cm^3/g)
$Pt/BaO/Al_2O_3$	33.4	131.5	0.11
$Pt/BaO/CeO_2$	20.9	148.4	0.08
$Pt/BaO/Ce_{0.75}Zr_{0.25}O_2$	33.8	92.3	0.08
$Pt/BaO/Ce_{0.5}Zr_{0.5}O_2$	35.3	75.0	0.07
$Pt/BaO/Ce_{0.25}Zr_{0.75}O_2$	27.7	78.0	0.05
$Pt/BaO/ZrO_2$	9.05	133.3	0.03

The nitrogen adsorption-desorption isotherms of the catalyst are presented in Figure 5.3. $Pt/BaO/Al_2O_3$ and $Pt/BaO/CeO_2$ and $Pt/BaO/ZrO_2$ show type II adsorption isotherm. On the other hand, $Pt/BaO/Ce_{0.75}Zr_{0.25}O_2$, $Pt/BaO/Ce_{0.5}Zr_{0.5}O_2$ and $Pt/BaO/Ce_{0.25}Zr_{0.75}O_2$ exhibit type IV adsorption isotherm. Type C hysteresis loop are observed for all catalysts. Hysteresis loops characterizes ink-bottle shape pores for $Pt/BaO/Ce_{0.75}Zr_{0.25}O_2$, $Pt/BaO/Ce_{0.5}Zr_{0.5}O_2$ and $Pt/BaO/Ce_{0.25}Zr_{0.75}O_2$ catalysts and wide mouth shape for $Pt/BaO/Al_2O_3$ and $Pt/BaO/CeO_2$ and $Pt/BaO/ZrO_2$ catalysts.

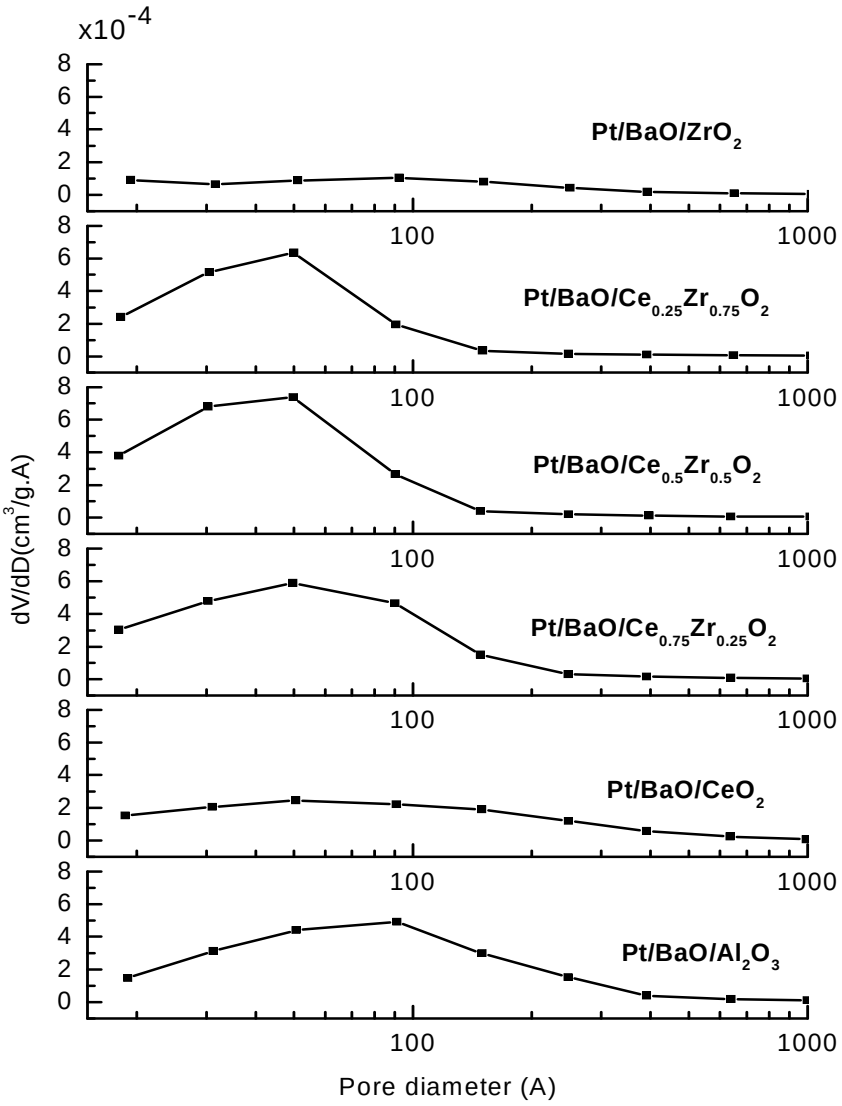

Figure 5.2: BJH pore size distribution of NSR catalysts

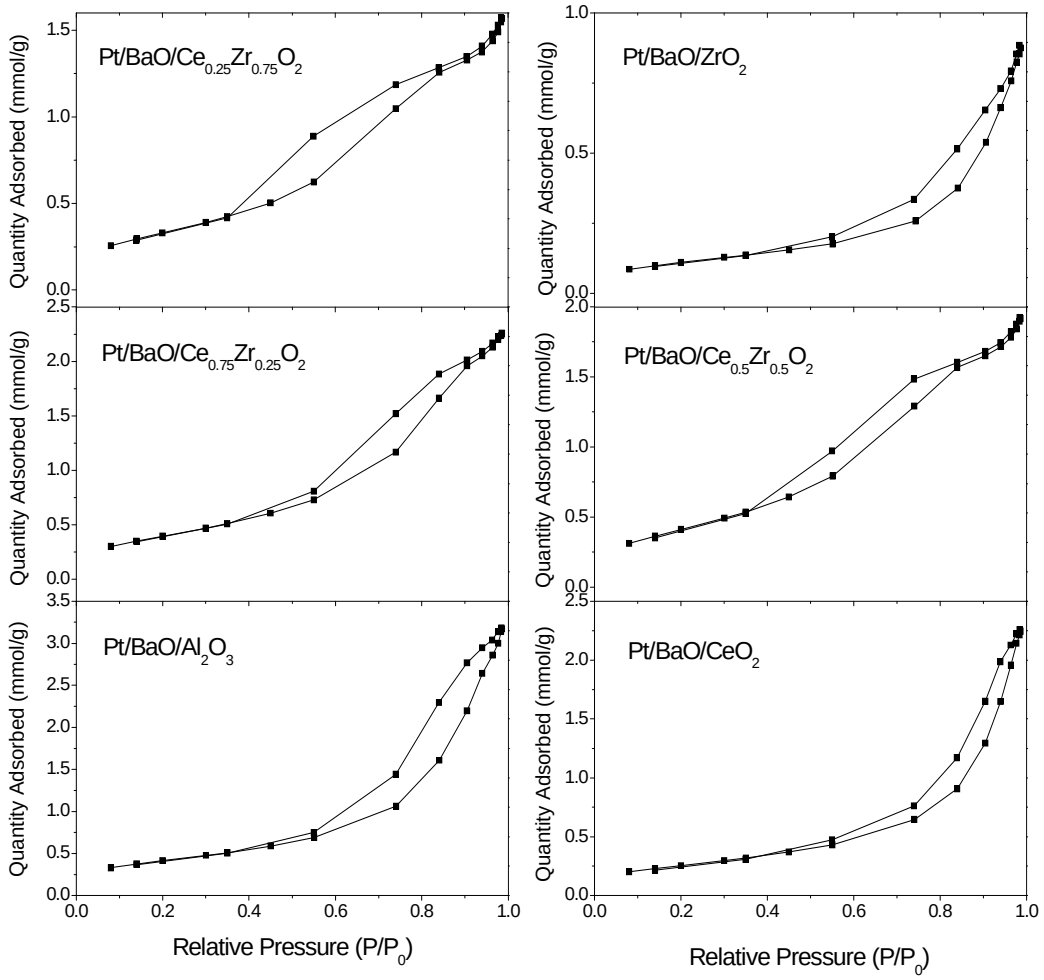

Figure 5.3: N_2 Adsorption-Desorption isotherms of NSR catalysts

5.3. TPR Analysis

The TPR profiles of catalysts were obtained by processing raw data. The experiment showed that hydrogen ion current signals of the catalysts exhibit baseline drift with respect to temperature. A similar baseline drift was also observed in the presence of an empty reactor. Therefore, for each catalyst polynomial baseline was substracted from raw data. The raw data and polynomial fitting for $Pt/BaO/Ce_{0.25}Zr_{0.75}O_2$ catalyst

are seen in Figure 5.4a. The H_2 consumption data with respect to temeparture for $Pt/BaO/Ce_{0.25}Zr_{0.75}O_2$ catalyst was determined by substracting raw data from polynomial fitting data. Then ion current was converted to concentration by multiplying with calibration factor. The final H_2 consumption data is seen in Figure 5.4b. The same procedure was repeated for other catalysts and TPR profiles for each catalyst were obtained.

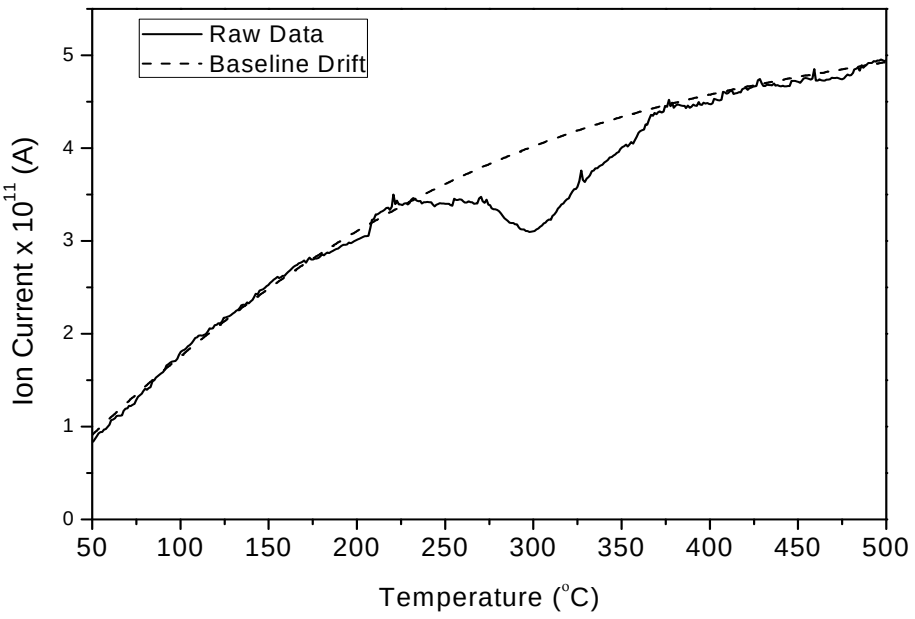

Figure 5.4a: The raw TPR data and polynomial fittting curve of $Pt/BaO/Ce_{0.25}Zr_{0.75}O_2$ catalyst

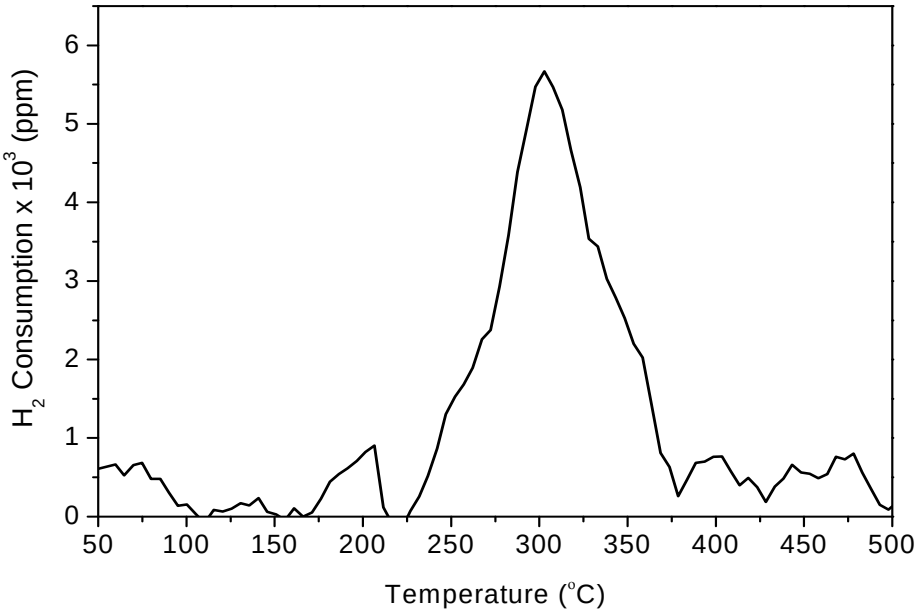

Figure 5.4b: TPR profile of the Pt/BaO/$Ce_{0.25}Zr_{0.75}O_2$ catalyst in the range of 50-500°C

Temperature programmed reduction (TPR) profiles of the NSR catalysts are shown in Figure 5.5. Profiles are shown in the temperature scale from 50 to 500°C. As seen in the Figure 5.5, in the presence of alumina and zirconia supported catalysts no remearkable H_2 consumption was observed. It was determined that the negative band at 350°C in the TPR profile of the alumina supported catalyst is originated from flow rate fluctutation. In contrast alumina and zirconia supported catalysts, the ceria-containing catalysts exhibit reduction peaks. In the literature it was demonstrated that the reduction of pure ceria was taken place in two stages [52-54]. Two peaks were observed at 550 and 900°C. The first peak at 550°C was attributed to the reduction of Ce^{+4} on the surface sites and the second peak at 900°C was attributed to the reduction of Ce^{+4} in bulk sites [55-57]. In the case of Ce-Zr mixed solution these two peaks are shifted to the lower temperature. It was exhibited that incorporation of zirconium in the ceria lattice increases H_2 consumption and decrease the temperature of surface and bulk reduction [53, 55, 58, 59]. Also, it was known that the presence of noble metal decreases the temperature of surface reduction [58, 60]. In our case, the pure

ceria supported catalyst shows a broad reduction peak about 150-450^{o}C and the peak maximum is placed at 312 ^{o}C. This peak could be attributed to the reduction of Ce^{4+} on the surface sites. Since the presence of Pt decreases the temperature of surface reduction, the maximum peak temperature is shifted from 550^{o}C to 312 ^{o}C. Also, two shoulders at 275 and 150^{o}C were observed in the TPR profile of pure ceria supported catalyst. These could be attributed to the reduction of chlorine containing precursors ($Pt^{4+}O_xCl_y$) which are originated from chlorine ion retaining on the surface and the reduction of Pt^{4+} on the surface, respectively [60 and references therein]. Nevertheless, these two assignments are controversial and in orger to give exact assignment extra experiments are needed. For Pt/BaO/$Ce_xZr_{1-x}O_2$ (x=0.75, 0.5, 0.25) catalysts, one peak was observed similar to ceria supported catalyst. These peaks are also assigned to the reduction of surface Ce^{4+} sites.

The maximum reduction temperature (T_{max}) and calculated the amount of H_2 consumed of Pt/BaO/$Ce_xZr_{1-x}O_2$ (x=1, 0.75, 0.5, 0.25) catalysts are also represented in Table 5.2. Table exhibits that the amount of H_2 consumption increases with increasing Zr content in the ceria lattice. The highest H_2 consumption is obtained in the presence of Pt/BaO/$Ce_{0.25}Zr_{0.75}O_2$ catalyst. This suggests that the reducibility of ceria is enhanced by incorporation of Zr into ceria lattice be consistent with literature [53, 55, 58, 59, 61]. Table 5.2 also shows that the reduction temperature of ceria containing catalysts were shifted to lower temperatures when the Zr content was greater than 0.5. This might be due to structure of the catalysts. We know that Pt/BaO/$Ce_{0.25}Zr_{0.75}O_2$ and Pt/BaO/$Ce_{0.5}Zr_{0.5}O_2$ catalysts indicate tetragonal phase and Pt/BaO/$Ce_{0.75}Zr_{0.25}O_2$ crystallizes into cubic phase. Therefore, it can be postulated that tetragonal phase are reduced easily compared to cubic phase. TPR results showed that the reduction peaks of the Pt/BaO/$Ce_xZr_{1-x}O_2$ (x=1, 0.75, 0.5, 0.25) catalysts are mainly associated with support reduction and the reducibility of the ceria containing catalyst is enhanced by incorporation of Zr into ceria lattice.

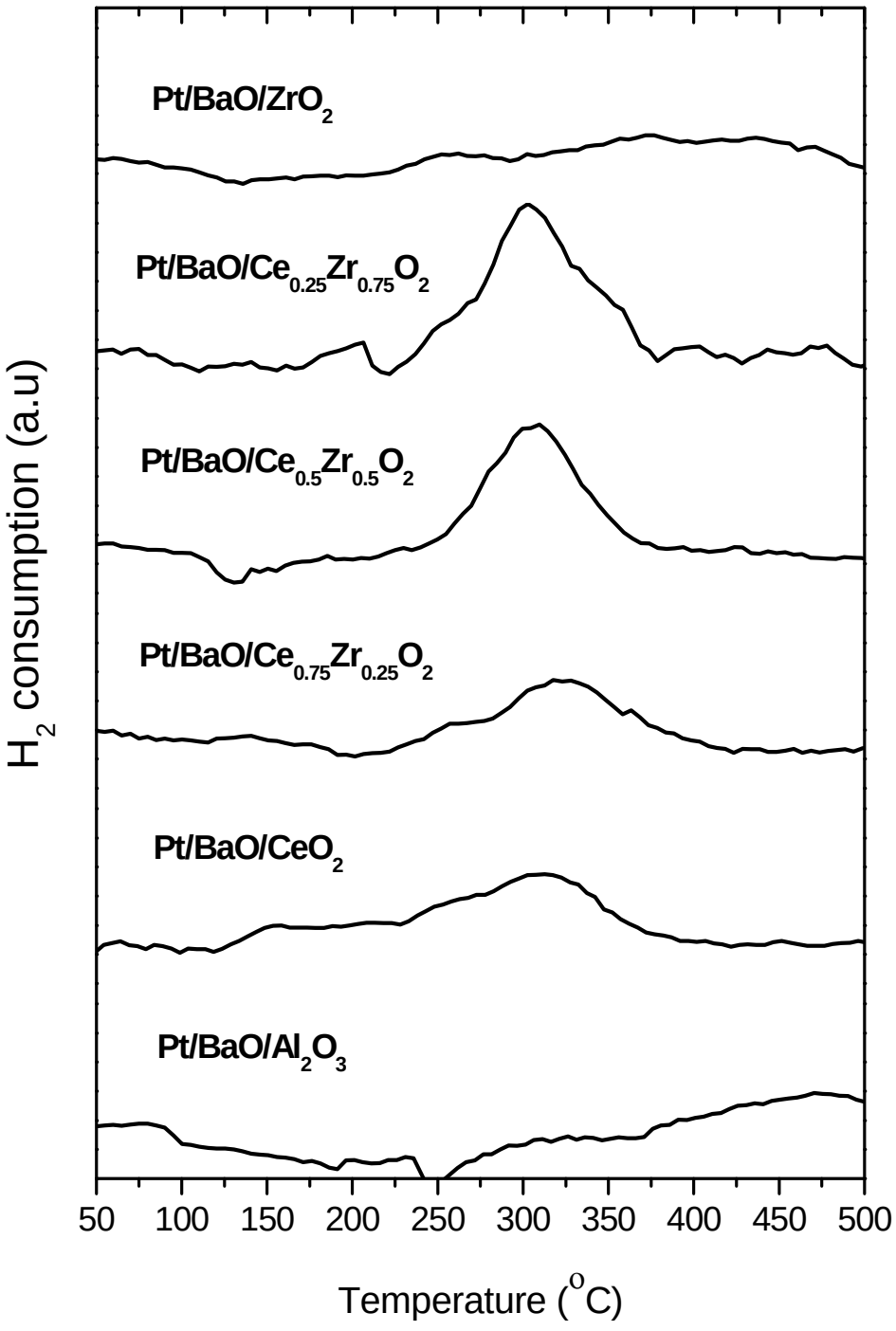

Figure 5.5: TPR profiles of NSR catalysts in the range of 50-500^{o}C

Table 5.2: TPR data of catalysts (maximum reduction temperature and the amount of H_2 consumed)

Catalyst	T_{max} (^oC)	H_2 consumed (µmol/g catalyst)
$Pt/BaO/CeO_2$	312	208.6
$Pt/BaO/Ce_{0.75}Zr_{0.25}O_2$	317	203.8
$Pt/BaO/Ce_{0.5}Zr_{0.5}O_2$	309	218.5
$Pt/BaO/Ce_{0.25}Zr_{0.75}O_2$	302	256.7

5.4 CO Chemisorption

The DRIFT spectra after admission of CO on $Pt/BaO/Al_2O_3$ at 50^oC are shown in Figure 5.6. As seen from the figure, there are three main bands appearing at low CO exposure and growing in intensity with increasing pressure: bands at (i) 2070 cm^{-1} (ii) 1786 cm^{-1} (iii) 1627 cm^{-1}. The band at 2070 cm^{-1} exhibits two shoulders at 2084 and 2000 cm^{-1}. These three bands at 2084, 2070 and 2000 cm^{-1} are attributed to linear bonded CO on Pt sites [62-65]. Literature studies suggest that as the electron density around Pt atom increases, the frequency of band decreases [62, 63, 66, 67]. Therefore, these three bands could be ascribed to $Pt^{\delta+}$ carbonyl, Pt^0 carbonyl and $Pt^{\delta-}$ carbonyl respectively. Pt^0 carbonyl forms due to partial reduction of PtO by CO or by H_2 at pretreatment stage and $Pt^{\delta-}$carbonyl accounts for a strong interaction between Pt and BaO. Moreover, the band at 1786 cm^{-1} could be ascribed to bridged bonded CO on Pt [64, 65] or CO adsorbed onto BaO [63] and 1627 cm^{-1} are assigned to bidentate carbonate on BaO [4 and references therein].

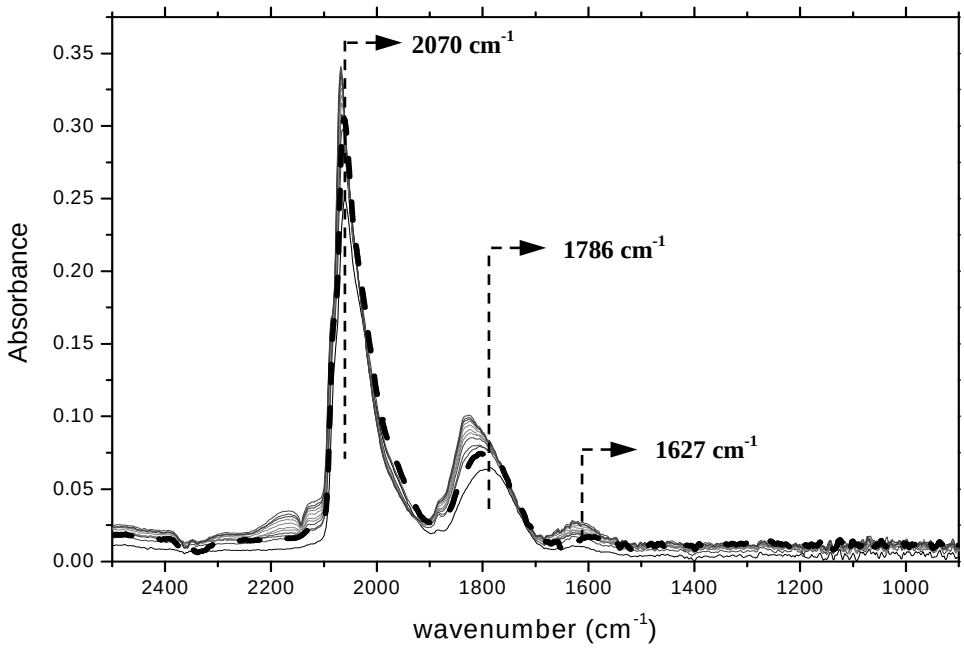

Figure 5.6: DRIFT Spectra after exposure of $Pt/BaO/Al_2O_3$ catalyst to (a) 1 torr (b) 5 torr (c) 10 torr (d) 15 torr (e) 20 torr (f) 25 torr (g) 30 torr (h) 35 torr (i) 40 torr (j) 45 torr (k) 50 torr CO at 50°C. All spectra were recorded after reaching equilibrium. Dashed line represents the spectra obtained after subsequent evacuation following 50 torr CO exposure.

The DRIFT spectra indicate that surface is covered by CO bound to Pt sites and carbonates on BaO phases in the presence of alumina supported catalyst. Similar surface species were also observed in the presence of $Pt/BaO/Ce_xZr_{1-x}O_2$ catalysts. In contrast to alumina supported catalyst, $Pt/BaO/Ce_xZr_{1-x}O_2$ catalysts exhibit a negative band at around 1980 cm^{-1}. It is proposed that this negative band arises from remaining H_2 after pretreatment process. Since the background spectra were taken after pretreatment process, the band associated with H_2 on Pt grows in intense negatively as H_2 desorbs from the surface. Thus, in order to prevent this negative band the evacucation time must be keep high after H_2 pretreatment. In order to make our explanation definite, CO chemisorption experiment on $Pt/BaO/Ce_{0.5}Zr_{0.5}O_2$ was repeated by increasing evacuation time after H_2 treatment. The DRIFT spectra of $Pt/BaO/Ce_{0.5}Zr_{0.5}O_2$ catalyst with low and high evacuation time are shown in Figure 5.7 and 5.8. As shown from the figures, negative band in the spectra with low

evacuation time (Figure 5.7) disappears after high evacuation time (Figure 5.8). In order to verify our explanation total area under all of the curves in the whole spectral region was also determined for spectra having low and high evacuation time. It was observed that total areas under the curve are similar for both spectra. Moreover, in order to be sure that the band at around 1980 cm^{-1} is attributed to H_2 on Pt site, the spectra obtained after H_2 treatment in the pretreatment stage was investigated. Figure 5.9 exhibits that the spectra obtained before the H_2 treatment and after H_2 treatment. As ssen from the figure, after H_2 treatment a band at 1988 cm^{-1} became apparent. Thus, it can be said that this band is ascribed to H_2 on Pt. Moreover, in the spectra of $Pt/BaO/Ce_xZr_{1-x}O_2$ catalysts the other bands at around 1600, 1540, 1450, 1300, 1250 and 1064 are ascribed to carbonate on BaO [4 and references therein].

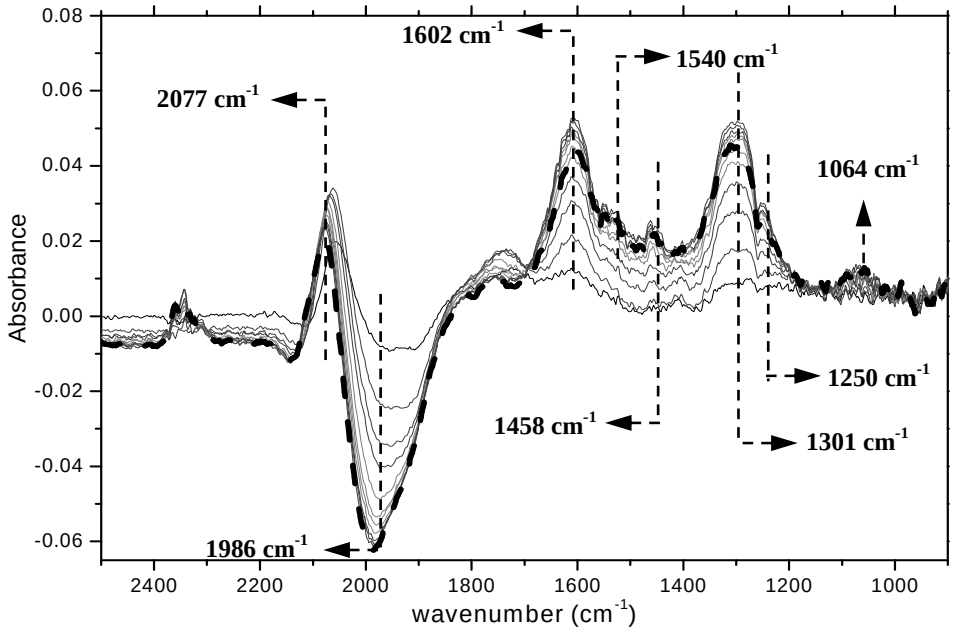

Figure 5.7: DRIFT Spectra with low evacuation time after exposure of $Pt/BaO/Ce_{0.5}Zr_{0.5}O_2$ catalyst to (a) 1 torr (b) 5 torr (c) 10 torr (d) 15 torr (e) 20 torr (f) 25 torr (g) 30 torr (h) 35 torr (i) 40 torr (j) 45 torr (k) 50 torr CO at 50^oC. All spectra were recorded after reaching equilibrium. Dashed line represents the spectra obtained after subsequent evacuation following 50 torr CO exposure.

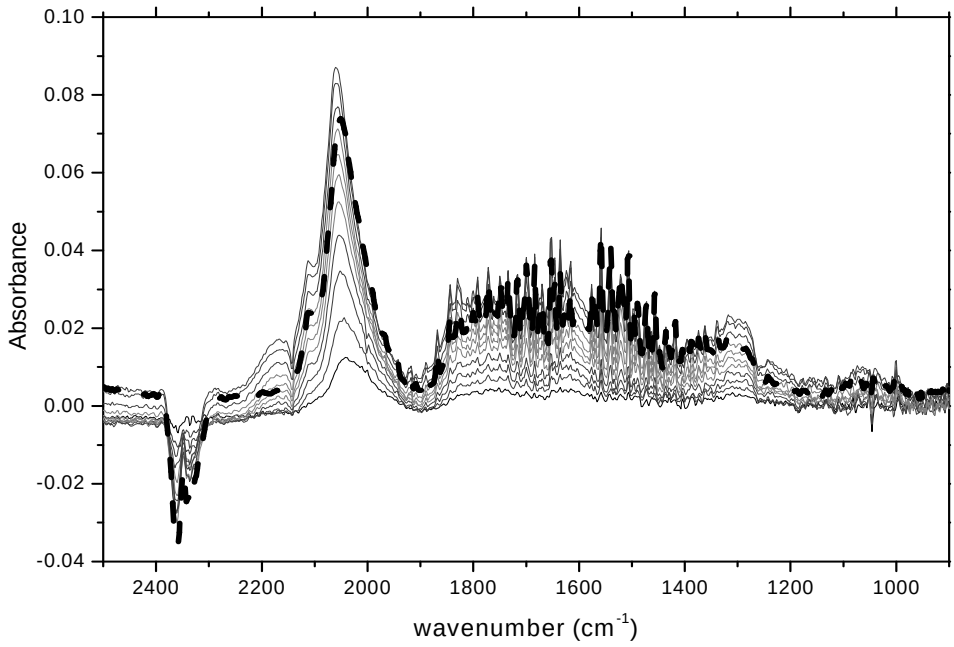

Figure 5.8: DRIFT Spectra with high evacuation time after exposure of Pt/BaO/ $Ce_{0.5}Zr_{0.5}O_2$ catalyst to (a) 1 torr (b) 5 torr (c) 10 torr (d) 15 torr (e) 20 torr (f) 25 torr (g) 30 torr (h) 35 torr (i) 40 torr (j) 45 torr (k) 50 torr CO at 50^{o}C. All spectra were recorded after reaching equilibrium. Dashed line represents the spectra obtained after subsequent evacuation following 50 torr CO exposure

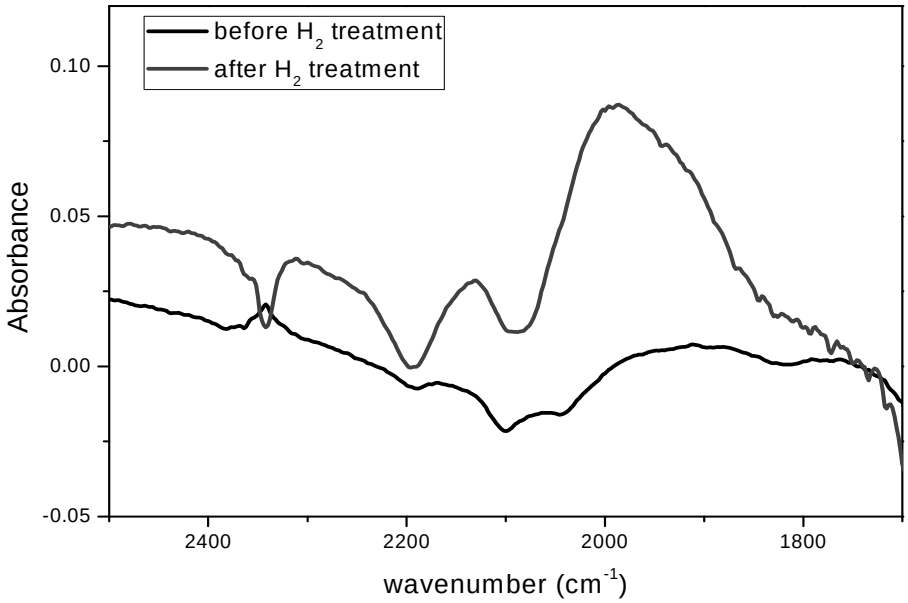

Figure 5.9: DRIFT spectra obtained before and after H_2 treatment in the pretreatment stage of the CO chemisorption experiment for Pt/BaO/$Ce_{0.5}Zr_{0.5}O_2$ catalyst

As verifying our explanation, the spectra obtained after evacuation were used to compare Pt dispersion of $Pt/BaO/Ce_xZr_{1-x}O_2$ catalysts ((The DRIFT spectra of $Pt/BaO/Ce_xZr_{1-x}O_2$ catalysts are shown in Appendix C). In order to be able to compare Pt dispersions of catalysts, the area under the bands associated with CO on Pt were used. For the $Pt/BaO/Ce_xZr_{1-x}O_2$ catalysts the areas under the peak at around 2080 cm^{-1} were calculated. The calculated areas with respect to per gram of catalysts are represented in Table 5.3. Table indicates that highest CO on Pt sites was observed in the presence of $Pt/BaO/Ce_{0.5}Zr_{0.5}O_2$ catalyst. In other words, $Pt/BaO/Ce_{0.5}Zr_{0.5}O_2$ reveals the highest Pt dispersion among the $Pt/BaO/Ce_xZr_{1-x}O_2$ catalysts. On the other hand, the lowest dispersion was observed in the presence of $Pt/BaO/ZrO_2$ catalyst.

Table 5.3: Total area under all of the curves in the whole spectral region normalized to per gram catalyst

Catalyst	**Total area under the curve (cm^{-1}/g catalyst)**
$Pt/BaO/CeO_2$	11.9
$Pt/BaO/Ce_{0.75}Zr_{0.25}O_2$	38.9
$Pt/BaO/Ce_{0.5}Zr_{0.5}O_2$	63.7
$Pt/BaO/Ce_{0.25}Zr_{0.75}O_2$	47.6
$Pt/BaO/ZrO_2$	27.3

5.5 Reaction Study

NO_X Storage and Reduction capability of catalysts were determined by reaction tests. Catalysts were exposed to 1000 ppm NO, 10% O_2 and balance inert gas mixture at lean period and 1100 ppm NO, 10000 ppm H_2 and balance inert gas mixture at rich period. The volumetric flow rates of gases were 171 and 137 for lean and rich period

respectively. The NO_x outlet concentration was determined by using ion current of (m/e=30) signal and recorded throghout the storage and reduction period.

Figure 5.10 indicates the NO_x outlet concentration for all catalysts investigated during the lean (O_2 excess) period. Figure shows that significant amount of NO_x are trapped on the surface for all samples. All catalysts exhibit similar storage behaviour in the time period from t=0 to t=200 s. In the first 20 s, total NO_x uptake occurs and after that NO_X trapping rate decreases slowly. Nonetheless, from t=200s to t=600 s catalysts give two different concentration profile. The one belongs to $Pt/BaO/Al_2O_3$, $Pt/BaO/CeO_2$ and $Pt/BaO/Ce_{0.25}Zr_{0.75}O_2$ shows nearly constant profile whereas the one belongs to $Pt/BaO/Ce_{0.75}Zr_{0.25}O_2$, $Pt/BaO/Ce_{0.5}Zr_{0.5}O_2$ and $Pt/BaO/ZrO_2$ exhibits a slow increase up to the end of the lean period. The amount of NO_x stored on the surface was calculated as integrated from t=0 to t=600 s subtracted from the concentration of saturation (inlet concentration-1000 ppm) multiplied by storage time. The results are presented in Table 5.4 as the ratio mole NO/mole BaO. Table shows that the NO_X trapping efficiency of catalysts does not differ too much from each other since similar BaO loadings were present on all samples. The highest NO_X trapping efficiency is observed in the presence of $Pt/BaO/Ce_{0.25}Zr_{0.75}O_2$ catalyst. $Pt/BaO/CeO_2$ and $Pt/BaO/Al_2O_3$ catalysts follow $Pt/BaO/Ce_{0.25}Zr_{0.75}O_2$ catalyst with 0.64 and 0.62 as mole NO/mole BaO. The lowest storage efficiency is observed in the presence of $Pt/BaO/Ce_{0.5}Zr_{0.5}O_2$ catalyst.

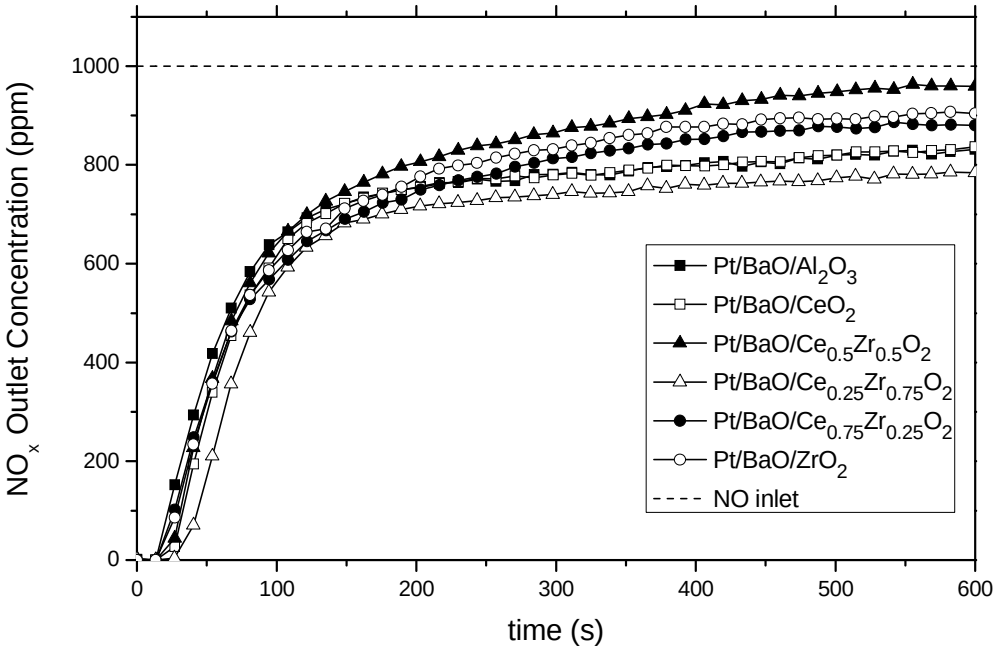

Figure 5.10: NOx Outlet Concentration during storage period in 1000 ppm NO, 10 % O_2 and balance Ar at 350 ^oC. The space velocity of gases is 41000 h^{-1}.

NO_x concentration profiles of all catalysts during the reduction period (regeneration-H_2 excess) are shown in Figure 5.11. As seen in the figure, Pt/BaO/$Ce_{0.25}Zr_{0.75}O_2$ displays highest breakthrough peak during the switching from lean to rich. This means that highest NO_x release occurs in the presence of Pt/BaO/$Ce_{0.25}Zr_{0.75}O_2$ catalyst. Pt/BaO/Al_2O_3, Pt/BaO/CeO_2 and Pt/BaO/$Ce_{0.5}Zr_{0.5}O_2$ have similar NO_x response and they exhibit higher NO_x breaktrough peak than the Pt/BaO/$Ce_{0.75}Zr_{0.25}O_2$ and Pt/BaO/ZrO_2 catalysts. The lowest breaktrough peak, in other words, the lowest NO_x release is observed in the presence of Pt/BaO/$Ce_{0.75}Zr_{0.25}O_2$ catalyst. When the breakthrough peak decreases, the NO_x concentration reaches to zero level within the 200 s indicating NO_x reduction by H_2. The fastest reduction rates (the fastest decrease in NO_x concentration) are observed in the presence of Pt/BaO/$Ce_{0.75}Zr_{0.25}O_2$, Pt/BaO/$Ce_{0.5}Zr_{0.5}O_2$ and Pt/BaO/ZrO_2 catalysts which have almost similar reduction behaviors. On the other hand Pt/BaO/ $Ce_{0.25}Zr_{0.75}O_2$ catalyst indicates the lowest reduction rate.

The amount of NO_x reduced was also calculated by integration method. The amount of NO_x released without being reduced is calculated as the integral from t=600 s to t=1500 s. Then total amount of NO_x passing through the reactor is calculated as multiplying inlet NO_x concentration by time. The amount of NO_x reduced is found by subtracting the amount of NO_x release from the total amount of NO_x. During the calculation, the effect of concentration increase (from 1000 ppm to 1100 ppm) due to switching from lean to rich is eliminated by using NO_x concentration data obtained from free reactor experiments. As a result of calculations, the reduction efficiencies of all catalysts are found by dividing the amount of NO_x reduced by the total amount NO_x and listed in Table 5.4. Table indicates that the highest and lowest reduction efficiencies are observed in the presence of $Pt/BaO/Ce_{0.75}Zr_{0.25}O_2$ and $Pt/BaO/Ce_{0.25}Zr_{0.75}O_2$ catalysts respectively.

The reaction results showed that all catalysts exhibits similar NO_x conversion during all operation time of lean-rich cycle and it is difficult to differentiate the catalytic performance of the catalysts from each other by using reaction data.

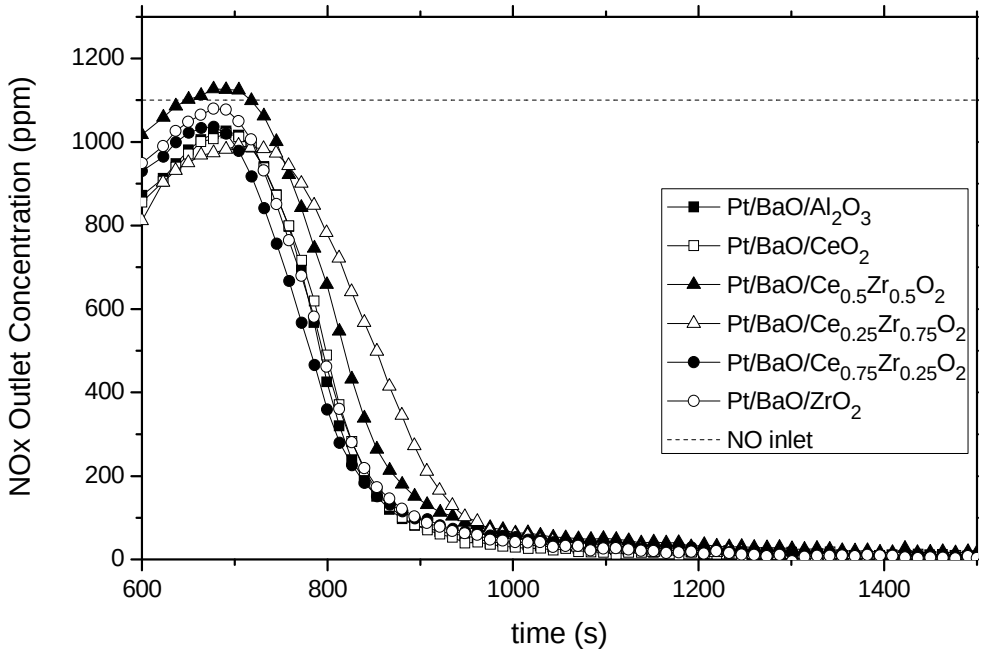

Figure 5.11: NOx Outlet Concentration during reduction period in 1100 ppm NO, 10000 ppm H_2 and balance Ar at 350 ^oC. The space velocity of gases is 37000 h^{-1}.

Table 5.4: Storage and Reduction Efficiencies of all catalysts

Catalyst	mole NO/mole BaO	NOx Reduction Efficinecy(%)
$Pt/BaO/Al_2O_3$	0.62	77.9
$Pt/BaO/CeO_2$	0.64	77.9
$Pt/BaO/Ce_{0.75}Zr_{0.25}O_2$	0.59	78.2
$Pt/BaO/Ce_{0.5}Zr_{0.5}O_2$	0.47	73.1
$Pt/BaO/Ce_{0.25}Zr_{0.75}O_2$	0.74	73.0
$Pt/BaO/ZrO_2$	0.54	77.1

5.6 In-situ DRIFT Spectroscopic Study of the NSR Process

Figure 5.12 shows the DRIFT spectra of all catalysts after admission of 1000 torr 10% NO in Ar, after subsequent evacuation and after H_2 treatment at 300^{o}C. As seen from the figure, after high gas admission four visible bands at 1627, 1765, 1845 and 1904 cm^{-1} were observed in the DRIFT spectra of $Pt/BaO/Al_2O_3$ catalyst. The band at 1627 cm^{-1} is assigned to bridging nitrate on Al_2O_3 [62 and references therein]. The band at 1765 cm^{-1} might be due to linear Pt^0 mononitrosyl or $Pt^{\delta-}$ mononitrosyl (Pt-NO) having strong interaction with BaO sites. In the literature it was suggested that $Pt^{\delta+}$ gives the band at 1800 cm^{-1} and the band frequency decreases with increasing electron density around the Pt atom [62]. Moreover, Hadjiivanov [68] and Kustov and Makkee [69] assigned band at 1778 and 1770 cm^{-1} to Pt^0 mononitrosyl. The other two peaks observed at 1904 and 1845 cm^{-1} are attributed to gas phase NO molecules [70]. It was observed that these peaks disappear after evacuation process. Also, the intensities of the bands at 1765 and 1627 cm^{-1} decreased after evacuation.

In the presence of alumina supported catalyst, no remarkable bands were observed in the spectral region 1600-1000 cm^{-1} after gas exposure. By contrast, in the related spectral region broad bands were observed in the presence of $Pt/BaO/Ce_xZr_{1-x}O_2$ catalysts. These bands are attributed to nitrite and nitrate species on the surface [4, 71-81]. The exact band positions observed in the DRIFT spectra of all catalyst after gas exposure and subsequent evacuation were summarized in Table 5.5. Figure 5.12 and Table 5.5 exhibit that after gas exposure the main intense bands were observed at around 1420 and 1320 cm^{-1} in the presence of $Pt/BaO/Ce_xZr_{1-x}O_2$ catalysts. These bands together with the band at 1040 cm^{-1} are assigned to monodentate nitrate on BaO phase [63, 65, 71, 72]. The band at 1040 cm^{-1} was not easily detected in the presence of $Pt/BaO/Ce_{0.25}Zr_{0.75}O_2$. The reason could be explained that the intense band at 1227 cm^{-1} and the band at 1040 cm^{-1} overlap. In addition to the band associated with monodentate nitrate on BaO, the bands at 1522 and 1255 cm^{-1} were also observed in the presence of $Pt/BaO/CeO_2$ and $Pt/BaO/Ce_{0.75}Zr_{0.25}O_2$. These bands are assigned to bridging bidentate nitrate on BaO phase [63, 65, 82]. The analogous band at 1255 cm^{-1} was also apparent whereas the analogous band at 1522

cm^{-1} is not discernible in the presence of $Pt/BaO/Ce_{0.5}Zr_{0.5}O_2$ and $Pt/BaO/ZrO_2$. The reason why the band at 1522 cm^{-1} was not observed in the presence of $Pt/BaO/Ce_{0.5}Zr_{0.5}O_2$ could be related to overlapping bands. Figure 5.12 exhibits that after gas exposure the band at 1522 cm^{-1} is not apparent due to intense peaks at 1625 and 1600 cm^{-1} which are attributed to gas phase NO_2 [70]. However, when the reaction cell was evacuated then the peaks associated with gas phase NO_2 disappeared and the band at 1522 cm^{-1} became discernible. The DRIFT spectra of all catalysts after exposure 1-1000 torr gas mixture and their background spectra were shown in Appendix D and E, respectively. The spectra of $Pt/BaO/Ce_xZr_{1-x}O_2$ catalysts exhibit that at low gas exposure, first the bands at around 1220 and 1180 cm^{-1} grow in intense and then when the gas pressure increases, the bands at 1420, 1320 and 1040 cm^{-1} become apparent. The bands at 1220 and 1180 cm^{-1} are assigned to bidentate nitrite on BaO phase [24, 63, 64, 72]. This suggest that NO is firstly conveted to nitrite at low gas pressure and then the nitrites are transformed into nitrate on the surface with increasing pressure. DRIFT spectra also shows that after the bands associated with monodentate nitrate on BaO become apparent and then the bands associated with bridging bidentate nitrate on BaO grow in intense. Thus, results imply that nitrites are transformed into monodentate nitrates and then in turn converted to bridging nitrate on BaO. Figure 5.12 shows that after high gas exposure, the band associated with bidentate nitrite on BaO (1220 cm^{-1}) was only observed in the presence of $Pt/BaO/Ce_{0.25}Zr_{0.75}O_2$ catalyst Also, the bands at 1522 and 1255 cm^{-1} were not observed in the presence of the same catalyst. This means that nitrites can not be totally converted to nitrates on the $Pt/BaO/Ce_{0.25}Zr_{0.75}O_2$ surface after high gas exposure.

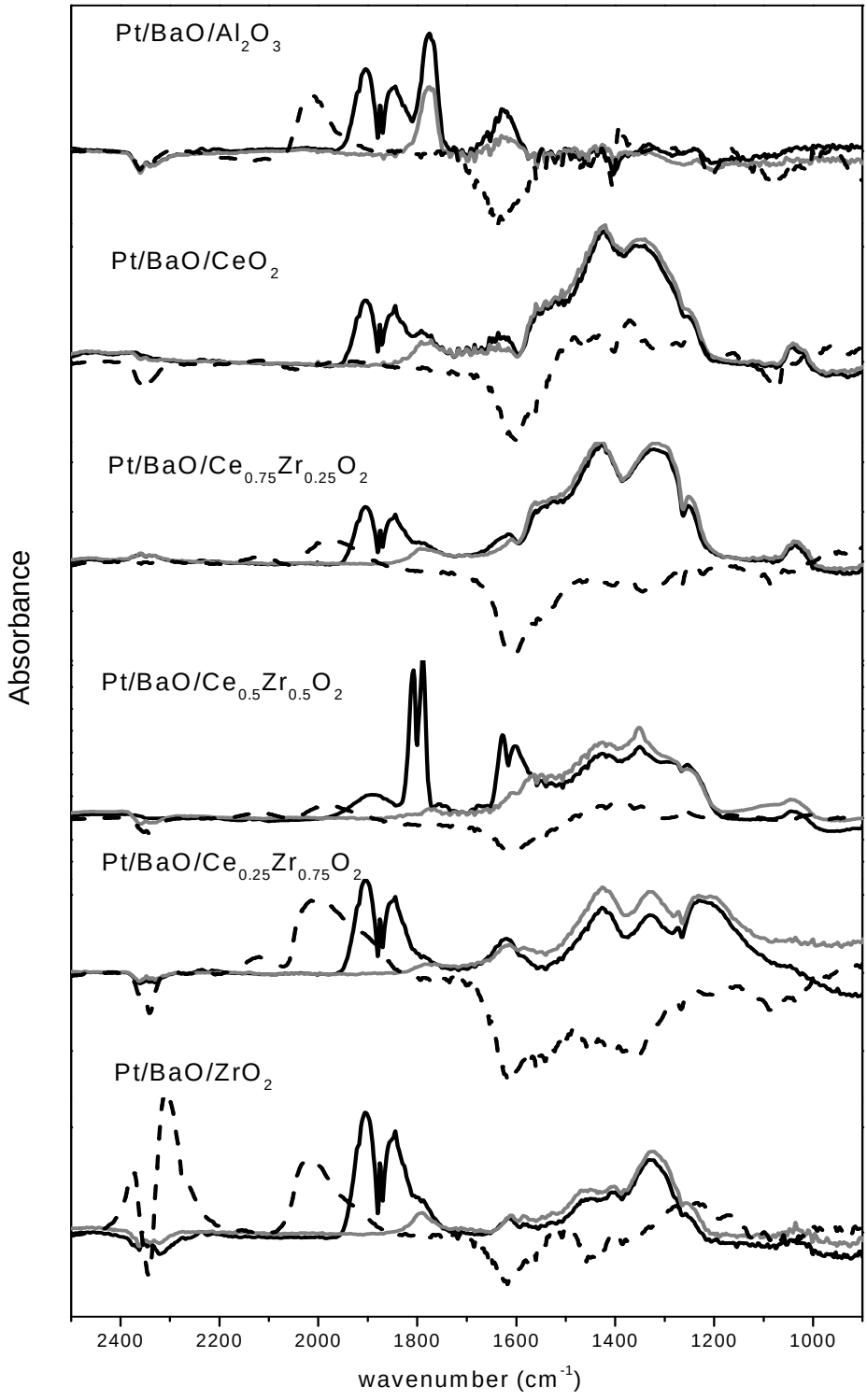

Figure 5.12: DRIFT spectra of all catalysts after admission of 1000 torr 10% NO in He (black line), after subsequent evacuation (gray line) and after H_2 treatment at 300^{o}C (dash line).

Table 5.5: Species detected by DRIFTS measurement after high gas exposure and following evacuation for each catalyst

Catalyst	Species and their wavenumbers (cm^{-1})											
	After high pressure gas exposure											
	Gas Phase NO [70]		Gas Phase NO_2 [70]		Pt mononitrosyl [62,68,69]	Bridging nitrate on support [62]	Bidentate nitrite on BaO [24,63,64,72]	Monodentate nitrate on BaO [63,65,71,72]			Bridging bidentate nitrate on BaO [63,65,82]	
$Pt/BaO/Al_2O_3$	1903	1844	-	-	1778	1627	-	-	-	-	-	-
$Pt/BaO/CeO_2$	1904	1846	-	-	1790	1635	-	1423	1348	1043	1522	1255
$Pt/BaO/Ce_{0.75}Zr_{0.25}O_2$	1905	1844	-	-	1798	1615	-	1427	1326	1035	1522	1252
$Pt/BaO/Ce_{0.5}Zr_{0.5}O_2$	-	-	1628	1600	1788	-	-	1423	1351	1041	-	1254
$Pt/BaO/Ce_{0.25}Zr_{0.75}O_2$	1905	1844	-	-	1788	1617	1227	1427	1330	-	-	1272
$Pt/BaO/ZrO_2$	1904	1846	-	-	1792	1616	-	1450	1330	1039	-	1256
	After evacuation											
$Pt/BaO/Al_2O_3$	-	-	-	-	1776	1627	-	-	-	-	-	-
$Pt/BaO/CeO_2$	-	-	-	-	1780	1635	-	1423	1342	1035	1520	1251
$Pt/BaO/Ce_{0.75}Zr_{0.25}O_2$	-	-	-	-	1788	1610	-	1427	1318	1031	1520	1249
$Pt/BaO/Ce_{0.5}Zr_{0.5}O_2$	-	-	-	-	1772	1628	-	1415	1350	1041	1529	1252
$Pt/BaO/Ce_{0.25}Zr_{0.75}O_2$	-	-	-	-	1782	1615	1218	1423	1326	-	-	1272
$Pt/BaO/ZrO_2$	-	-	-	-	1792	1610	-	1447	1324	1031	-	1254

As mentioned before, the band around 1780 cm^{-1} is attributed to Pt mononitrosyl. After high gas exposure, in the presence of Pt/BaO/$Ce_xZr_{1-x}O_2$ (x=1, 0.75, 0.25, 0) catalysts the band at 1780 cm^{-1} was not clearly observed due to band overlapping. However, in the presence of Pt/BaO/$Ce_{0.5}Zr_{0.5}O_2$ catalyst two separate bands at 1809 and 1790 cm^{-1} were observed. These two bands could be associated with NO adsorbed on two different Pt sites. The band at 1809 cm^{-1} could be due to NO adsorbed on positively charged Pt ($Pt^{\delta+}$-NO) and the band 1790 might correspond to neutral or negatively charged Pt (Pt-NO or $Pt^{\delta-}$NO). After evacuation process, the band at 1809 cm^{-1} disappears completely and the band at 1790 cm^{-1} considerably decreases in intensity. Just the opposite is valid for the Pt/BaO/$Ce_xZr_{1-x}O_2$ (x=1, 0.75, 0.25, 0) catalysts. After evacuation process, the band at around 1780 cm^{-1} became more apparent for the Pt/BaO/$Ce_xZr_{1-x}O_2$ (x=1, 0.75, 0.25, 0) catalysts. The frequencies of the band after evacuation for each catalyst are shown in Table 5.5. Table shows that the lowest frequency of the band belongs to Pt/BaO/$Ce_{0.5}Zr_{0.5}O_2$ catalyst. As discussed before, the frequency of the Pt mononitrosyl band decreases with increasing electron density around Pt particles. Thus, if the band frequency decreases then the Pt-BaO interaction increases due to electronegative effect of O atoms in the BaO sites. This implies that the highest Pt-BaO interaction was observed in the presence of Pt/BaO/$Ce_{0.5}Zr_{0.5}O_2$.

Figure 5.12 exhibits the spectra obtained after evacuation process. It was seen that there were no substantial change in the spectra of the catalysts. Table 5.5 shows that the band positions were shifted to lower frequency and the intensity of the bands decreases after evacuation. The spectra obtained after evacuation process reveal the remaining surface species after NO_X storage and they could give information about NO_x storage performance of the catalysts. In order to compare the storage activities of all catalysts, the absorbance value of the spectra obtained after evacuation process was divided by the amount of the catalyst and normalized absorbance values were obtained. The normalized absorbance values of all catalysts with respect to freguency are shown in Figure 5.13. Figure 5.13 demonstrates normalized spectra of all catalysts after evacuation process. As mentioned before, the spectral region at 1550-1250 cm^{-1} belongs to nitrate bands. As seen from the Figure, the highest nitrate

formation was observed in the presence of $Pt/BaO/Ce_{0.5}Zr_{0.5}O_2$. Also, $Pt/BaO/Ce_{0.75}Zr_{0.25}O_2$ exhibits high storage performance. No remarkable nitrate formation was observed in the presence of alumina supported catalyst. Figure 5.13 could also provide information about Pt dispersion. The band at around 1780 cm^{-1} is attributed to NO on Pt sites. Figure shows that highest band intensity was observed in the presence of $Pt/BaO/Ce_{0.5}Zr_{0.5}O_2$ and $Pt/BaO/Al_2O_3$. The other catalysts reveal almost similar band intensity. Since each catalyst contains same amount of Pt, this suggest that $Pt/BaO/Ce_{0.5}Zr_{0.5}O_2$ and $Pt/BaO/Al_2O_3$ have the highest Pt dispersion. The idea that $Pt/BaO/Ce_{0.5}Zr_{0.5}O_2$ has high Pt dispersion is supported by Figure 5.12. Figure 5.12 exhibits that the bands associated with gas phase NO_2 was only observed in the presence of $Pt/BaO/Ce_{0.5}Zr_{0.5}O_2$. This means that the remarkable amount of NO is oxidized to NO_2 on the $Pt/BaO/Ce_{0.5}Zr_{0.5}O_2$ surface even in the absence of gas phase O_2.

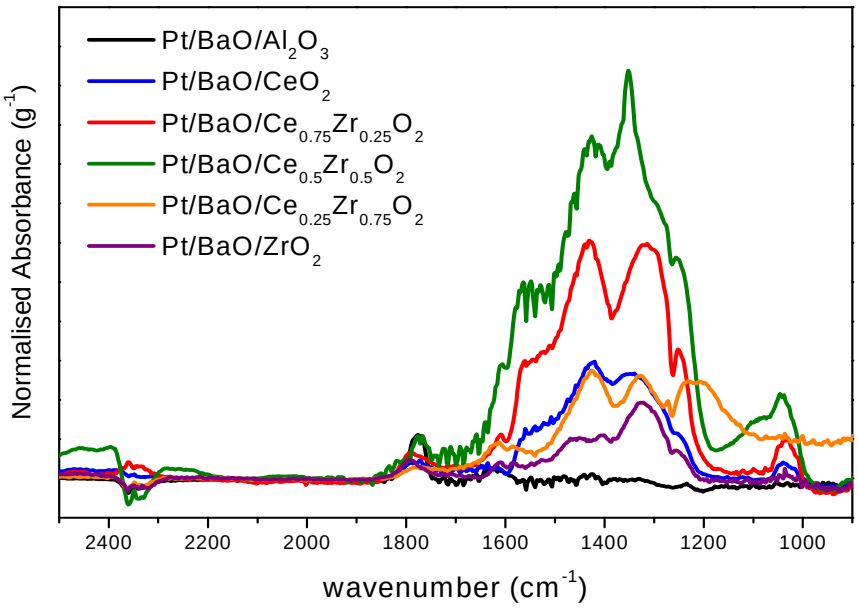

Figure 5.13: The normalized absorbance values of all catalysts with respect to freguency after evacuation process

The NO_X reduction behaviours of the catalysts were also investigated by DRIFTS analysis. Figure 5.12 exhibits the spectra of all catalysts obtained after H_2 treatment at 300^{o}C. As seen from the figure the bands associated with the nitrates and nitrites disappear for all catalysts. This means that nitrates and nitrites decompose after the reduction period for all catalysts. Also, negative band at 1627 cm^{-1} was observed in the spectra of alumina supported catalyst and negative bands were observed in the spectral region 1620-1250 cm^{-1} in the spectra of $Pt/BaO/Ce_xZr_{1-x}O_2$. CO chemisorption experiments exhibit that the negative band at 1627 cm^{-1} in the spectra of alumina supported catalyst is attributed to bidentate carbonate on BaO phase and the negative bands in the spectral region 1620-1250 cm^{-1} are attributed to carbonates on BaO phases for $Pt/BaO/Ce_xZr_{1-x}O_2$. This means that surface carbonates were replaced by surface nitrates after NO exposure and since the band positions of carbonates and nitrates overlap, first no the negative bands was observed after carbonate decomposition. However, after the surface was reduced by H_2, then nitrate also decomposed and negative band became apparent. In contrast to negative bands, after reduction positive bands become apparent in the spectra of all catalysts except for $Pt/BaO/Ce_{0.5}Zr_{0.5}O_2$ catalyst. The positive band was observed at around 2000 cm^{-1} in the presence of all catalyst except for $Pt/BaO/Ce_{0.5}Zr_{0.5}O_2$ catalyst. The CO chemisorption experiments showed that this band is attributed to H_2 on Pt sites (the band in Figure 2.9). In addition, positive band at around 2100 cm^{-1} was also observed in the presence of $Pt/BaO/Ce_xZr_{1-x}O_2$ (x=0.75, 0.5, 0.25). This band is assigned to cynanide on Pt [65].

DRIFTS results demonstrate that NO is stored on the $Pt/BaO/Ce_xZr_{1-x}O_2$ catalysts in the form of nitrite and nitrate whereas no nitrate and nitrite formations were observed in the presence of alumina supported catalyst. This means that $Pt/BaO/Ce_xZr_{1-x}O_2$ catalysts are able to convert NO_X molecules into surface nitrite and nitrates in the absence of gas phase O_2 at room temperature. This could be due to high oxygen mobility of $Ce_xZr_{1-x}O_2$ supports. Since the NO_2 is precursor for the trapping process, in other words, the NO oxidation reaction is preliminary step for NO_x storage process; the high oxygen mobility of $Ce_xZr_{1-x}O_2$ could favor the storage reaction. The oxygen mobility of catalysts was tested by means of TPR analysis. The TPR results

reveal that the highest oxygen mobility of support or highest reducibility was observed in the presence of $Pt/BaO/Ce_{0.25}Zr_{0.75}O_2$ catalyst. The $Pt/BaO/Ce_{0.5}Zr_{0.5}O_2$ catalyst exhibited the second highest reducibility. As opposed to TPR results, low amount of nitrate formation was observed on the surface of $Pt/BaO/Ce_{0.25}Zr_{0.75}O_2$ catalyst. Along with nitrate, nitrite was also observed in the presence of $Pt/BaO/Ce_{0.25}Zr_{0.75}O_2$ catalyst. However, no nitrite formation was observed on the surface of other catalysts. The highest nitrate formation was observed in the presence of $Pt/BaO/Ce_{0.5}Zr_{0.5}O_2$ catalyst. This could be related to high Pt dispersion on the surface. This idea was supported by CO chemisorption experiments. The CO chemisorption experiments demonstrate that the $Pt/BaO/Ce_{0.5}Zr_{0.5}O_2$ catalyst revealed the highest Pt dispersion. The peaks due to gas phase NO_2 also suggest that the $Pt/BaO/Ce_{0.5}Zr_{0.5}O_2$ catalyst could oxidize the considerable amount of NO to NO_2 in the absence of gas phase O_2. In addition, the reduction activities of catalysts were observed via DRIFTS analysis. It was observed that all nitrates and nitrites decomposed after reduction for all catalytsts.

Throughout the study, the storage and reduction activities of catalysts were investigated. Reaction results revealed that all catalysts exhibits similar NO_X conversion for lean and rich period and it is difficult to differentiate the performance of catalysts from each other. Thus, the actual importance belongs to DRIFTS results. DRIFTS results reveal that the $Pt/BaO/Ce_xZr_{1-x}O_2$ (x=0.75, 0.5, 0.25) shows higher storage performance than the ceria and zirconia supported catalysts. Among the $Pt/BaO/Ce_xZr_{1-x}O_2$ (x=0.75, 0.5, 0.25), the highest performance was observed in the presence of $Pt/BaO/Ce_{0.5}Zr_{0.5}O_2$ catalyst. The TPR and CO chemisorption experiments suggest that this performance is attributed to both high reducibility of support and high Pt dispersion.

CHAPTER 6

SUMMARY AND CONCLUSIONS

The NO_x storage and reduction over $Pt/BaO/Ce_xZr_{1-x}O_2$ (x= 1, 0.75, 0.5, 0.25, 0) catalysts was studied. The NO_x storage and reduction capability of catalysts were investigated by reaction tests and DRIFTS. $Pt/BaO/Al_2O_3$ was used as reference NSR catalyst to compare storage and reduction activities of catalysts. Ce-Zr mixed oxide was synthesized via Pechini Method and phases were detected by XRD. XRD results indicated that Ce and Zr ions are homogeneously distributed in prepared samples. After phase verification, 10 % BaO (w/w) and 1% Pt (w/w) were loaded on mixed oxide and reference alumina support sequentially. The prepared $Pt/BaO/Ce_xZr_{1-x}O_2$ and $Pt/BaO/Al_2O_3$ catalyst were characterized by BET. BET results exhibited that $Pt/BaO/Ce_xZr_{1-x}O_2$ (x= 0.75, 0.5, 0.25) catalysts have higher BET surface area and narrower pore size distribution than $Pt/BaO/CeO_2$ and $Pt/BaO/ZrO_2$ catalysts. The highest surface area was observed in the presence of $Pt/BaO/Ce_{0.5}Zr_{0.5}O_2$ catalyst and the lowest surface area was observed in the presence of $Pt/BaO/ZrO_2$. BET characterization was followed by H_2 temperature programmed reduction (TPR) study. TPR analysis was made to observe reducibility of catalysts. TPR results showed that the reduction peaks of the $Pt/BaO/Ce_xZr_{1-x}O_2$ (x=1, 0.75, 0.5, 0.25) catalysts are mainly associated with support reduction and the reducibility of the ceria containing catalyst is enhanced by incorporation of Zr into ceria lattice. In order gain insight about Pt dispersion of catalysts CO chemisorption experiments were also made. The $Pt/BaO/Ce_{0.5}Zr_{0.5}O_2$ catalyst revealed the highset Pt disperison. The NO_x storage and reduction activities were tested by reaction analysis at 350^oC. The results

demonstrated that the NO_x storage and reduction activity of all catalysts does not differ remarkably from each other. The NO_X storage performances of all catalysts were differentiated from each other by means of in-situ DRIFTS study. DRIFTS results revealed that the highest amount of nitrate formation occurs on the surface of $Pt/BaO/Ce_{0.25}Zr_{0.75}O_2$ catalyst. This is assigned to both high reducibility of support and high Pt dispersion of catalyst. The reduction activities were also tested by in-situ DRIFTS analysis. It was shown that all nitrates on the surface of all catalysts decomposed after H_2 reduction at 300^oC.

REFERENCES

[1] New Scientist Environment-Special Report Energy and Fuels
World Energy Use Graphic,
http://environment.newscientist.com/data/images/ns/sreport_graphic/energy-fuels-mg18725151500.jpg, (last accessed date: 22th August, 2008)

[2] W. S. Epling, A. Yezerets, N. W. Currier, Appl Catal B-Environ 74 (2007) 117–129

[3] E. M. Holmgreen, M. M. Yung, U. S. Ozkan, Appl Catal B-Environ 74 (2007) 73–82

[4] E. Fridell, M. Skoglundh, B. Westerberg, S. Johansson, G. Smedler, J Catal 183 (1999) 196–209

[5] Design of an Otto Cycle,
http://www.qrg.northwestern.edu/thermo/design-library/otto/otto.html,
(last accessed date: 27th July, 2008)

[6] J. Kašpar, P. Fornasiero, N. Hickey, Catal Today 77 (2003) 419–449

[7] N. Nejar, M. Makkee, M. J. Illan-Gomez, Appl Catal B-Environ 75 (2007) 11–16

[8] M. Chaoa, T. Lina, H. Chaoa, F. Changa, C. Chenb, Sci Total Environ 279 (2001) 167-179

[9] Emission Standards,
http://www.dieselnet.com/standards, (last accessed date: 27th July, 2008)

[10] J. A.Z. Pieterse, S. Booneveld, Appl Catal B-Environ 73 (2007) 327–335

[11] H. Iwakuni, Y. Shinmyou, H. Yano, H. Matsumoto, T. Ishihara, Appl Catal B-Environ 74 (2007) 299–306

[12] B. Akca, Synthesıs and Characterızatıon of Co-Pb/Sba-15 Mesoporous Catalysts, Middle East Technical University, Ankara (2006)

[13] P. Forzatti, I. Nova, L. Castoldi, Chem Biochem Eng Q 19 (4) (2005) 309–323

[14] Matsumoto, S. Cattech 4 (2000) 102

[15] P. Broqvist, H. Gro1nbeck, E. Fridell, J Phys Chem B 108 (2004) 3523-3530

[16] A. Amberntsson, H. Persson, P. Engström, B. Kasemo, Appl Catal B-Environ 31 (2001) 27–38

[17] M. Adamowska, S. Muller, P. Costa, A. Krzton, P. Burg, Appl Catal B-Environ 74 (2007) 278–289

[18] W. S. Epling, L. E. Campbell, A. Yezerets, N. W. Currier, J. E. Parks, Cataly Rev 46 (2) (2004) 163-245

[19] R. L. Muncrief, K. S. Kabin, M. P. Harold, AIChE Journal 50 (10) (2004) 2526-2540

[20] H. Ohtsuka, T. Tabata, Appl Catal B-Environ 29 (2001) 177

[21] H. Ohtsuka, Appl Catal B-Environ 33 (2001) 325

[22] A. Amberntsson, E. Fridell, M. Skoglundh, Appl Catal B-Environ 46 (2003) 429

[23] E. Xue, K. Seshan, J. R.H. Ross, Appl Catal B-Environ 11 (1996) 65

[24] H. Mahzoul, J.F. Brilhac, P. Gilot, Appl Catal B-Environ 20 (1999) 47

[25] L. Lietti, P. Forzatti, I. Nova, E. Tronconi, J Catal. 204 (2001) 175

[26] E. Fridell, M. Skoglundh, S. Johansson, B. Westerberg, A. Torncrona, G. Smedler, Stud Surf Sci Catal 116 (1997) 537

[27] X. Li, M. Meng, P. Lin, Y. Fu, T. Hu, Y. Xie, J. Zhang, Top Catal 22 (2003) 111

[28] T. Kobayashi, T Yamada, K. Kayano, SAE Technical Paper Series 970745

[29] N. Takahashi, H. Shinjoh, T. Iijima, T. Suzuki, K. Yamazaki, K. Yokota, H. Suzuki, N. Miyoshi, S. Matsumoto, T. Tanizawa, T. Tanaka, S. Tateishi, K. Kasahara, Catal Today 27 (1996) 63

[30] G. Fornasari, F. Trifiro, A. Vaccari, F. Prinetto, G. Ghiotti, G. Centi, Catal Today 75 (2002) 421

[31] M. Piacentini, M. Maciejewski, A. Baiker, Appl Catal B-Environ 59 (2005) 187-195

[32] M. Piacentini, M. Maciejewski, A. Baiker, Appl Catal B-Environ 60 (2005) 265-275

[33] J. Szanyi, J. H. Kwak, D. H. Kim, X. Wang, J. Hanson, R. J. Chimentao, C. H. F. Pedena, Chem Commun (2007) 984–986

[34] P.T. Fanson, M.R. Horton, W.N. Delgass, J. Lauterbach, Appl Catal B-Environ 46 (2003) 393

[35] V. Labalme, N. Benhamou, N. Guilhaume, E. Garbowski, M. Primet, Appl Catal A-Gen 133 (1995) 351

[36] L. Castoldi, I. Nova, L. Lietti, P. Forzatti, Catal Today 96 (2004) 43–52

[37] M. Piacentini, M. Maciejewski, A. Baiker, Appl Catal B-Environ 72 (2007) 105-117

[38] C.M.L. Scholz, V.R. Gangwal, M.H.J.M. de Croon, J.C. Schouten, J Catal 245 (2007) 215–227

[39] W. S. Epling, G. C. Campbell, J. E. Parks, Catal Lett 90 1–2 (2003) 45-56

[40] Z. Liu, J. Anderson, J Catal 224 (2004) 18-27

[41] V. Medhekar, V. Balakotaiah, M. P. Harold, Catal Today 121 (2007) 226–236

[42] Y. Li, S. Roth, J. Dettling, T. Beutel, Top Catal 16-17 (2001) 1-4

[43] M. R. Morelli, R. J. Brook in Ceramic Processing Science and Technology 51, Eds. H. Hausner, G. L. Messing, S. Hirano, The American Ceramic Society, Vol 51 pp. 81-85 1995

[44] H. H. Kung in Studies in Surface Science and Catalysis 45:Transition Metal Oxides, Eds. H. H. Kung, Elsevier, pp. 121-135 1989

[45] J. Lin, M. Yu, C. Lin, X. Liu, J Phys Chem C 111 (2007) 5835-5845

[46] V. A. Sadykova, T. G. Kuznetsovaa, S. A. Veniaminova, D. I. Kochubeya, B. N. Novgorodova, E. B. Burginaa, E. M. Moroza, E. A. Paukshtisa, V. P. Ivanova, S. N. Trukhana, S. A. Beloshapkina, Y. V. Potapovaa, V. V. Luninc, E. Kemnitzd, A. Aboukaise, React Kinet Catal Lett 76 No:1 (2002) 83-92

[47] M. S. Wong in Metal Oxides: Chemistry and Applications, Eds. J. L. G. Fierro, Taylor&Francis, pp. 31-54 2006

[48] W. V. Knowles, M. O. Nutt, M. S. Wong in Catalyst Preparation: Science and Engineering, Eds. J. Regalbuto, Taylor&Francis, pp. 251-279 2007

[49] C. Bozo, F. Gaillard, N. Guilhaume, Appl Catal A-Gen 220 (2001) 69–77

[50] B. M. Reddy, A. Khan, Catal Surv Asia 9 (3) (2005) 155-171

[51] S. Pengpanich, V. Meeyoo, T. Rirksomboon, K. Bunyakiat, Appl Catal A-Gen 234 (2002) 221–233

[52] K. Otsuka, W. Ye, M. Nakamura, Appl Catal A-Gen 183 (1999) 317-324

[53] P. Fornasiero, G. Balducci, R. Di Monte, J. Kaspar, V. Sergo, G. Gubitosa, A. Ferrero, M. Graziani, J Catal 164 (1996) 173-183

[54] M. F. Luo, X. M. Zheng, Appl Catal A-Gen 189 (1999) 15-21

[55] A. Trovarelli, F. Zamar, J. Llorca, C. Leitenburg, G. Dolcetti, J. T. Kiss, J Catal 169 (1997) 490-502

[56] S. Pengpanich, V. Meeyoo, T. Rirksomboon, K. Bunyakiat, Appl Catal A-Gen 234 (2002) 221-233

[57] C. Bozo, N. Guilhaume, E. Garbowski, M. Primet, Catal Today 59 (2000) 33-45

[58] P. Fornasiero, J. Kaspar, M. Graziani, J Catal 167 (1997) 576-580

[59] S. Ricote, G. Jacobs, M. Milling, Y. Ji , P. M. Patterson, B. H. Davis, Appl Catal A-Gen 303 (2006) 35–47

[60] P. Fornasiero, J. Kaspar, V. Sergo, M. Graziani, J Catal 182 (1999) 56-69

[61] S. Larrondo, M. A. Vidal, B. Irigoyen, A. F. Craievich, D. G. Lamas, I. O. Fabregas, G. E. Lascalea, N. E. Walsöe de Reca, N. Amadeo, Catal Today, 107-108 (2005) 53-59

[62] F. Prinetto, G. Ghiotti, I. Nova, L. Lietti, E. Tronconi, P. Forzatti, J Phys Chem B 105 (2001) 12732-12745

[63] P. T. Fanson, M. R. Horton, W. N. Delgass, J. Lauterbach, Appl Catal B-Environ 46 (2003) 393-413

[64] J. Luo, M. Meng, Y. Zha, Y. Xie, T. Hu, J. Zhang, T. Liu, Appl Catal B-Environ 78 (2008) 38–52

[65] H. Abdulhamid, J. Dawody, E. Fridell, M. Skoglundh, J Catal 244 (2006) 169-182

[66] V. B. Kazanski, V. Y. Borovkov, E. G. Derouane, Catal Lett 19 (1993) 327-331

[67] Z. Gandao, B. Coq, L. Charles de Menorval, D. Tichit, Appl Catal A-Gen 147 (1996) 395-406

[68] K. I. Hadjiivanov, Catal Rev 42 (1&2) (2000) 71-144

[69] A. L. Kustov, M. Makkee, Appl Catal B-Environ (2008), article in press

[70] X. Chen, J. Schwank, J. Li, W. F. Schneider, C. T. Goralski, P. J. Schmitz, Appl Catal B-Environ 61 (2005) 164–175

[71] C. Sedlmair, K. Seshan, A. Jentys, J. A. Lercher, J Catal 214 (2003) 308-316

[72] K. Shimizu, Y. Saito, T. Nobukawa, N. Miyoshi, A. Satsuma, Catal Today 139 (2008) 24–28

[73] S. M. Mathew, S. B. Umbarkar, M. K. Dongare, Catal Commun 8 (2007) 1178–1182

[74] T. Lesage, C. Verrier, P. Bazin, J. Saussey, M. Daturi, Phys Chem Chem Phys 5 (2003) 4435–4440

[75] P. Broqvist, H. Grönbeck, E. Fridell, I. Panas, Catal Today 96 (2004) 71–78

[76] J. A. Anderson, B. Bachiller-Baeza, M. Fernandez-Garcia, Phys Chem Chem Phys 5 (2003) 4418–4427

[77] Y. Su, K. S. Kabin, M. P. Harold, M. D. Amiridis, Appl Catal B-Environ 71 (2007) 207–215

[78] B. R. Kromer, L. Cao, L. Cumaranatunge, S. S. Mulla, J. L. Ratts, A. Yezerets, N. W. Currier, F. H. Ribeiro, W. N. Delgass, J. M. Caruthers, Catal Today 136 (2008) 93–103

[79] R. S. Larson, J. A. Pihl, V. K. Chakravarthy, T. J. Toops, C. S. Daw, Catal Today 136 (2008) 104–120

[80] L.F. Liotta, A. Macaluso, G.E. Arena, M. Livid, G. Centi, G. Deganello, Catal Today 75 (2002) 439–449

[81] F. Prinetto, G. Ghiotti, I. Nova, L. Castoldi, L. Lietti, E. Tronconi, P. Forzatti, Phys Chem Chem Phys 5 (2003) 4428–4434

[82] Y. Su, M. D. Amiridis, Catal Today 96 (2004) 31

APPENDIX A

EQUILIBRIUM CONVERSION CALCULATIONS

App. A.1 Equilibrium conversions calculations of storage reactions

The nitrite route reactions:

$$NO + 1/2O_2 \Leftrightarrow NO_2 \quad (1)$$

$$BaO + 2NO_2 + 1/2O_2 \Leftrightarrow Ba(NO_3)_2 \quad (2)$$

Table A.1: Enthalpy and Gibbs Free Energy of Species

	ΔH^o (kj/mol)	ΔG^o (kj/mol)
NO (g)	90.3	86.6
NO_2 (g)	33.2	51.2
O_2 (g)	0	0
BaO (s)	-553.5	-525.1
$Ba(NO_3)_2$	-992.1	-796.6

For Reaction 1:

$$\Delta H^o_{rxn} = \sum_i \nu_i \Delta H^o_{f,i} = 33.2 - 90.3 = -57.1 kj/mol \quad \text{(eqn 1)}$$

$$\Delta G^{o}_{rxn} = \sum_i \nu_i \Delta G^{o}_{f,i} = 51.2 - 86.6 = -35.4 kj/mol \quad \text{(eqn 2)}$$

$$K_{a1} = \exp(\frac{-\Delta G^{o}_{rxn}}{RT}) = \exp(\frac{35400}{8.314 \times 298})) = 4.48 \times 10^{6} \quad \text{(eqn 3)}$$

$$K_a(T_2) = K_a(T_1) \exp[(\frac{-\Delta H^{o}_{rxn}}{R}) \times (\frac{1}{T_2} - \frac{1}{T_1})] \quad \text{(eqn 4)}$$

If we choose temperature as 350 ^{o}C or 623 K;

$T = 623K$

$$K_{a1}(T = 623K) = 4.48 \times 10^{6} [\frac{57100}{8.314} (\frac{1}{623} - \frac{1}{298})] = 5.13 \quad \text{(eqn 5)}$$

For Reaction 2:

$$\Delta H^{o}_{rxn} = \sum_i \nu_i \Delta H^{o}_{f,i} = (-992.1) - [(33.2)(2) + (-553.5)] = -505.0 kj/mol$$

(eqn 6)

$$\Delta G^{o}_{rxn} = \sum_i \nu_i \Delta G^{o}_{f,i} = (-796.6) - [(51.2)(2) - (525.1)] = -373.9 kj/mol$$

(eqn 7)

$$K_{a2} = \exp(\frac{-\Delta G^{o}_{rxn}}{RT}) = \exp(\frac{373900}{8.314 \times 298}) = 3.47 \times 10^{65} \quad \text{(eqn 8)}$$

$$K_{a2}(T = 623K) = 3.47 \times 10^{65} [\frac{505000}{8.314} (\frac{1}{623} - \frac{1}{298})] = 2.30 \times 10^{19} \quad \text{(eqn 9)}$$

If we call the extent of reaction 1 and 2 as X_1 and X_2 respectively, then initial and final number of moles of species would be in the following:

Table A.2: Numbers of Species Moles for nitrite route reaction

Species	Initial Number of Moles	Final Number of Moles
NO	1	$1-2X_1$
NO_2	-	$2X_1-4X_2$
O_2	100	$100-X_1-X_2$
Inert	899	899
Total	1000	$1000- X_1-5X_2$

Using relation between the equilibrium constant and the specific activities of species:

$$K_a = \prod_{i=1} a_i^{\nu_i} \qquad \text{(eqn 10)}$$

Since the total pressure is close to atmospheric pressure during the operation, the activities gas components are equal to molar fraction of them. Also, it is assumed that activities of solid components are equal to 1.

$$a_{NO} = P_{NO} = P \times y_{NO} \qquad \text{(eqn 11)}$$

$$a_{NO_2} = P_{NO_2} = P \times y_{NO_2} \qquad \text{(eqn 12)}$$

$$a_{O_2} = P_{O_2} = P \times y_{O_2} \qquad \text{(eqn 13)}$$

$$a_{Ba(NO_3)_2} = a_{BaO} = 1 \qquad \text{(eqn 14)}$$

Then;

$$K_{a1}(T) = \prod_{i=1} a_i^{\nu_i} = \frac{a_{NO_2}^{\ 2}}{a_{NO}^{\ 2} \times a_{O_2}} = \frac{y_{NO_2}^{\ 2}}{y_{NO}^{\ 2} \times y_{O_2}} = \frac{4(1000 - X_1 - 5X_2)(X_1 - 2X_2)^2}{(100 - X_1 - X_2)(1 - 2X_1)^2}$$

(eqn 15)

$$K_{a2}(T) = \prod_{i=1} a_i^{\nu_i} = \frac{a_{Ba(NO_3)_2}^{\ 2}}{a_{BaO}^{\ 2} \times a_{NO_2}^{\ 4} \times a_{O_2}} \qquad \text{(eqn 16)}$$

$$K_{a2}(T) = \prod_{i=1} a_i^{\nu_i} = \frac{1}{y_{NO_2}^{\ 2} \times y_{O_2}^{\ 1/2}} = \frac{(1000 - X_1 - 5X_2)^5}{16(100 - X_1 - X_2)(X_1 - 2X_2)^4}$$

The K values calculated from eqn 5 and 9 are substituted into eqn 15 and 16 respectively and then extents of reactions are calculated by Mathlab Program (Mathlab code is shown in Appendix B.1). Equilibrium conversions of reactions are calculated by using extents of reactions.

The nitrate route reactions:

$$NO + 1/2O_2 \Leftrightarrow NO_2 \qquad (1)$$

$$BaO + 3NO_2 \Leftrightarrow Ba(NO_3)_2 + NO \qquad (3)$$

In order to find equilibrium constant of reaction 3 (K_{a3}), calculation procedure similar to nitrite reaction route is followed and final equality is given in the equation 17.

$$K_{a3}(T = 623K) = 2.69 \times 10^{18} \qquad \text{(eqn 17)}$$

Initial and final numbers of moles of species are shown in Table A.3.

Table A.3: Numbers of Species Moles for nitrate route reaction

Species	Initial Number of Moles	Final Number of Moles
NO	1	$1-2X_1+X_2$
NO_2	-	$2X_1-3X_2$
O_2	100	$100-X_1$
Inert	899	899
Total	1000	$1000- X_1-2X_2$

Using the mole numbers in Table A.3 and equation 10, following equations are obtained:

$$K_{a1}(T)=\prod_{i=1} a_i^{\nu_i}=\frac{a_{NO_2}{}^2}{a_{NO}{}^2\times a_{O_2}}=\frac{y_{NO_2}{}^2}{y_{NO}{}^2\times y_{O_2}}=\frac{(1000-X_1-2X_2)(2X_1-3X_2)^2}{(100-X_1)(1-2X_1+X_2)^2} \quad \text{(eqn 18)}$$

$$K_{a3}(T)=\prod_{i=1} a_i^{\nu_i}=\frac{a_{Ba(NO_3)_2}\times a_{NO}}{a_{BaO}\times a_{NO_2}{}^3} \quad \text{(eqn 19)}$$

$$K_{a3}(T)=\prod_{i=1} a_i^{\nu_i}=\frac{y_{NO}}{y_{NO_2}{}^3}=\frac{(1000-X_1-2X_2)^2(1-2X_1+X_2)}{(2X_1-3X_2)^3}$$

Extents of reactions are calculated by Mathlab Program (Mathlab code is shown in Appendix B.1). Equilibrium conversions of reactions are calculated by using extents of reactions.

App. A.2 Equilibrium conversions calculations of regeneration reactions

The regeneration reactions are listed below:

$$H_2 + 1/2O_2 \Leftrightarrow H_2O \quad (4)$$

$$NO_2 + H_2 \Leftrightarrow NO + H_2O \quad (5)$$

$$NO + H_2 \Leftrightarrow 1/2N_2 + H_2O \quad (6)$$

The decomposition reaction of the nitrate was excluded from regeneration reactions, since it was assumed that all nitrates were converted to NO_2 and O_2 according to reverse reaction of nitrate formation by nitrite route.

Table A.4: Enthalpy and Gibbs Free Energies of Species

	ΔH^o (kj/mol)	ΔG^o (kj/mol)
NO (g)	90.3	86.6
NO_2 (g)	33.2	51.2
H_2 (g)	0	0
O_2 (g)	0	0
H_2O	-241.8	-228.6

In order to find the reaction enthalpies and gibbs free energies for each reaction same procedure using in the storage reaction were applied and the results were shown at Table 3.2 in the theory part. Furthermore, equilibrium constants of reactions were calculated in the same manner.

Initial and final numbers of moles of species in the regeneration period are shown in Table A.5 (X_4, X_5, X_6 are extent of reactions of reaction 4,5 and 6 respectively).

Initial molar flow rate of NO_2 and O_2 were calculated by assuming that barium nitrate forming on the surface at the storage period totally decomposed with a constant rate throughout the regeneration period. So,

The mass of $BaNO_3$ on the surface was found by:

$$m_{Ba(NO_3)_2} = m_{catalyst} \times 0.1 = 0.05 \times 0.1 = 5 \times 10^{-3}\, g \qquad \text{(eqn 20)}$$

The mole of $Ba(NO_3)_2$:

$$n_{Ba(NO_3)_2} = \frac{m_{Ba(NO_3)_2}}{MW_{Ba(NO_3)_2}} = \frac{5 \times 10^{-3}\, g}{153 g / moles} = 3.27 \times 10^{-5}\, moles \qquad \text{(eqn 21)}$$

Then according to nitrate decomposition reaction by nitrite route:

$$Ba(NO_3)_2 \Leftrightarrow BaO + 2NO_2 + 1/2O_2$$

The mole numbers of NO_2 and O_2 were:

$$n_{NO_3} = 2 \times n_{Ba(NO_3)_2} = (2)(3.27 \times 10^{-5}) = 6.54 \times 10^{-5}\, moles \qquad \text{(eqn 22)}$$

$$n_{O_3} = (1/2) \times n_{Ba(NO_3)_2} = (1/2)(3.27 \times 10^{-5}) = 1.635 \times 10^{-5}\, moles \qquad \text{(eqn 23)}$$

Then, dividing mole numbers of NO_2 and O_2 by duration time of regeneration period molar flow rate of NO_2 and O_2 were found:

$$\dot{n}_{NO_2} = \frac{6.54 \times 10^{-5}\, moles}{900 s} = 7.27 \times 10^{-8}\, moles / s \qquad \text{(eqn 24)}$$

$$\dot{n}_{O_2} = \frac{1.635 \times 10^{-5}\, moles}{900 s} = 1.82 \times 10^{-8}\, moles / s \qquad \text{(eqn 25)}$$

The molar flow rate of NO, H_2 and inert gas were also taken consistent number with our flow reaction study:

$$\dot{n}_{NO} = 1.15 \times 10^{-7} \, moles / s$$

$$\dot{n}_{H2} = 1.15 \times 10^{-6} \, moles / s$$

$$\dot{n}_{Ar} = 1.15 \times 10^{-6} \, moles / s$$

Then, the molar flow rates of gases were normalized with respect to total molar flow rate of gases and normalized value of molar flow rate used as initial mole numbers of gases in Table A.5. Molar flow rate and normalized value were shown in Table A.6.

Table A.5: Numbers of Species Moles for regeneration period

Species	Initial Number of Moles	Final Number of Moles
NO	1.1	$1.1-2X_6+X_5$
NO_2	0.7	$0.7-X_5$
O_2	0.2	$0.2-X_4$
H_2	11	$11-2X_4-X_5-2X_6$
H_2O	-	$2X_4+2X_6+X_5$
N_2	-	X_6
Inert	987	987
Total	1000	$1000- X_4-X_6$

Table A. 6: Molar flow rate and normalized value of gases in regeneration period

	$\dot{n}$ (molar flow rate)$\times 10^{-8}$	Normalized Value
NO (g)	11.5	1.1
NO_2 (g)	7.27	0.7
H_2 (g)	115	11
O_2 (g)	1.82	0.2
inert	10300	987
total	10435.59	1000

Using the mole numbers in Table A.5 and equation 10, following equations are obtained:

$$K_{a4}(T) = \frac{(2X_4 + 2X_6 + X_5)^2 (1000 - X_1 - X_3)}{(11 - 2X_4 - X_5 - 2X_6)^2 (0.2 - X_4)} = 1.18 \times 10^{40} \qquad \text{(eqn 26)}$$

$$K_{a4}(T) = \frac{(2X_4 + 2X_6 + X_5)(1.1 + X_5 - 2X_6)}{(11 - 2X_4 - X_5 - 2X_6)(0.7 - X_4)} = 7.35 \times 10^{33} \qquad \text{(eqn 27)}$$

$$K_{a6}(T) = \frac{(2X_4 + 2X_6 + X_5)^2 (X_6)(1000 - X_4 - X_6)}{(11 - 2X_4 - X_5 - 2X_6)^2 (1.1 + X_5 - 2X_6)^2} = 1.78 \times 10^{55} \qquad \text{(eqn 28)}$$

These three equations were solved by Mathlab Program simultaneously and the extent of reactions were calculated (Appendix B.2). Equilibrium conversions of reactions are calculated by using extents of reactions.

APPENDIX B

MATLAB PROGRAM CODE FOR CONVERSION CALCULATIONS

App. B.1 Matlab program code used to calculate extent of reactions at storage period

Matlab Code for Nitrite Route Reactions

```
K1_0 = 2.57e12;% Equilibrium Constant of oxidation reaction at 298 K
K2_0 = 1.399e131;% Equilibrium Constant of storage reaction at 298 K

T=transpose(300:100:1300); % Temperature (K)

for i=1:11
K1 = K1_0*exp((13735.86/T(i)) - 46.09); % Equilibrium Constant of
%oxidation reaction at different temperatures between 300-1300K
K2 = K2_0*exp((121481.8/T(i)) - 407.65); % Equilibrium Constant of
%storage reaction at different temperatures between 300-1300K
end
syms x1 x2;

S = solve('(((2*x1-4*x2)^2)*(1000-x1-5*x2))/((1000-x1-x2)*((1-
2*x1)^2))-K1','((1000-x1-5*x2)^5)/((100-x1-x2)*((2*x1-4*x2)^4))-
K2');
```

Matlab Code for Nitrate Route Reactions

```
K1_0 = 2.57e12;% Equilibrium Constant of oxidation reaction at 298 K
K2_0 = 8.15e118;% Equilibrium Constant of storage reaction at 298 K

T=transpose(300:100:1300); % Temperature (K)

for i=1:11
K1 = K1_0*exp((13735.86/T(i)) - 46.09); % Equilibrium Constant of
%oxidation reaction at different temperatures between 300-1300K
K2 = K2_0*exp((121481.8/T(i)) - 407.65); % Equilibrium Constant of
%storage reaction at different temperatures between 300-1300K
end
```

```
syms x1 x2;

S=solve('(((2*x1-3*x2)^2)*(1000-x1-2*x2))/((100-x1)*((1+x2-
2*x1)^2))-K1','(((1000-x1-2*x2)^2)*(1+x2-2*x1))/((2*x1-3*x2)^3)-
K2');
```

App. B.2 Matlab program code used to calculate extent of reactions at regeneration period

```
K1_0 = 1.179e40;   % Equilibrium Constant of oxidation reaction at
298 K
K2_0 = 7.347e33; % Equilibrium Constant of storage reaction at 298 K
K3_0 = 1.784e55; % Equilibrium Constant of storage reaction at 298 K


T=transpose(300:100:1300); % Temperature (K)

for i=1:11
K1 = K1_0*exp((13735.86/T(i)) - 46.09); % Equilibrium Constant of
oxidation reaction at different temperatures between 300-1300K
K2 = K2_0*exp((121481.8/T(i)) - 407.65); % Equilibrium Constant of
storage reaction at different temperatures between 300-1300K
K3 = K3_0*exp((133485.6/T(i)) – 345.92); % Equilibrium Constant of
storage reaction at different temperatures between 300-1300K

end
syms x1 x2 x3;

S = solve('(((2*x3-4*x2)^2)*(1000-x1-5*x2))/((1000-x1-x2)*((1-
2*x1)^2))-K1','((1000-x1-5*x3)^5)/((100-x1-x2)*((2*x1-4*x2)^4))-
K2',’ ((1000-x1-5*x2)^5)/((100-x1-x2)*((2*x1-4*x3)^4))-K3);
```

APPENDIX C

DRIFT SPECTRA OF CATALYSTS AFTER CO EXPOSURE

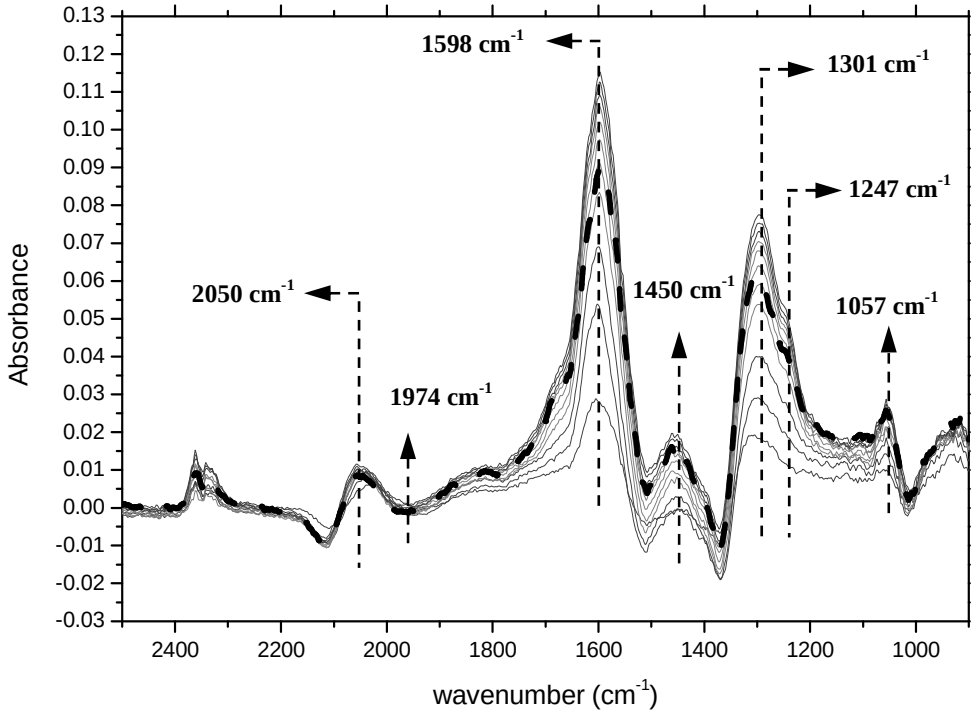

Figure C.1: DRIFT Spectra after exposure of $Pt/BaO/CeO_2$ catalyst to (a) 1 torr (b) 5 torr (c) 10 torr (d) 15 torr (e) 20 torr (f) 25 torr (g) 30 torr (h) 35 torr (i) 40 torr (j) 45 torr (k) 50 torr CO at 50^oC. All spectra were recorded after reaching equilibrium. Dashed line represents the spectra obtained after subsequent evacuation following 50 torr CO exposure.

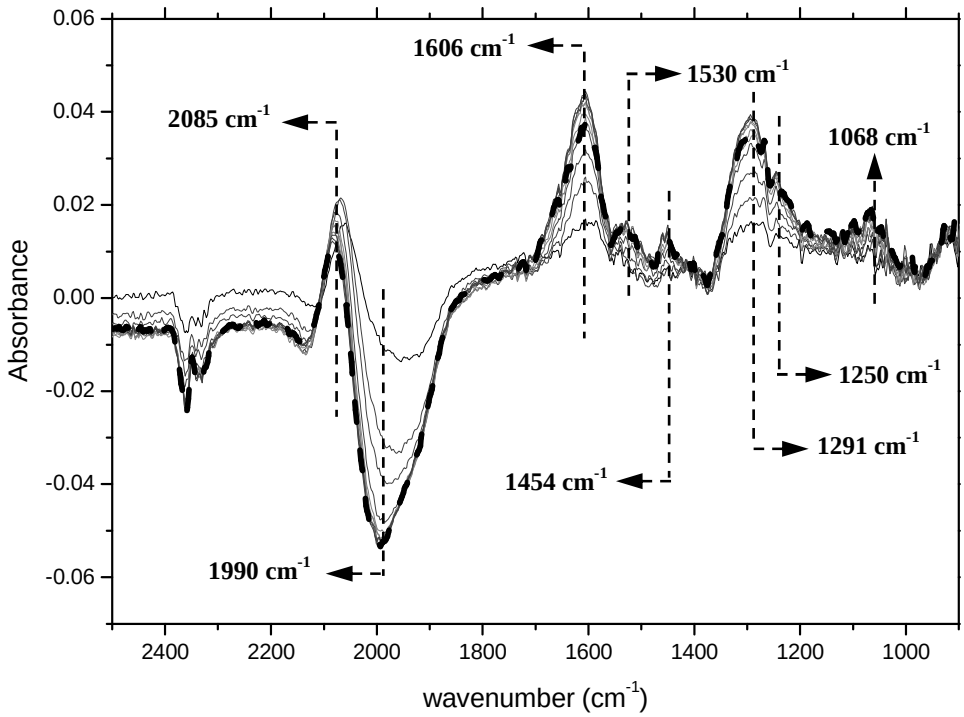

Figure C.2: DRIFT Spectra after exposure of Pt/BaO/$Ce_{0.75}Zr_{0.25}O_2$ catalyst to (a) 1 torr (b) 5 torr (c) 10 torr (d) 15 torr (e) 20 torr (f) 25 torr (g) 30 torr (h) 35 torr (i) 40 torr (j) 45 torr (k) 50 torr CO at 50^{o}C. All spectra were recorded after reaching equilibrium. Dashed line represents the spectra obtained after subsequent evacuation following 50 torr CO exposure

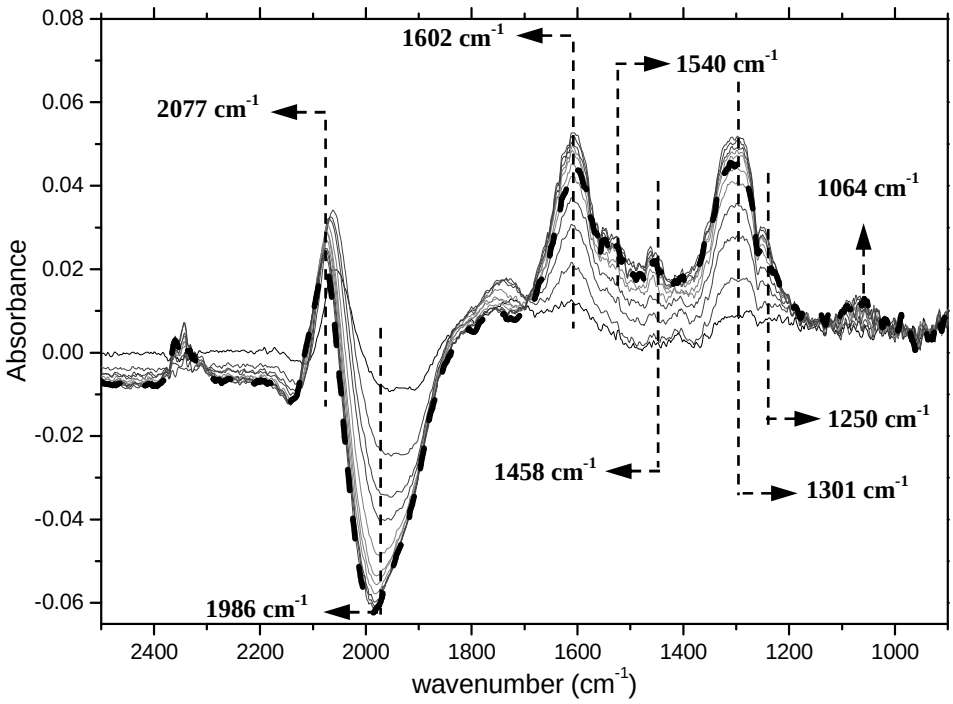

Figure C.3: DRIFT Spectra after exposure of $Pt/BaO/Ce_{0.5}Zr_{0.5}O_2$ catalyst to (a) 1 torr (b) 5 torr (c) 10 torr (d) 15 torr (e) 20 torr (f) 25 torr (g) 30 torr (h) 35 torr (i) 40 torr (j) 45 torr (k) 50 torr CO at 50^oC. All spectra were recorded after reaching equilibrium. Dashed line represents the spectra obtained after subsequent evacuation following 50 torr CO exposure

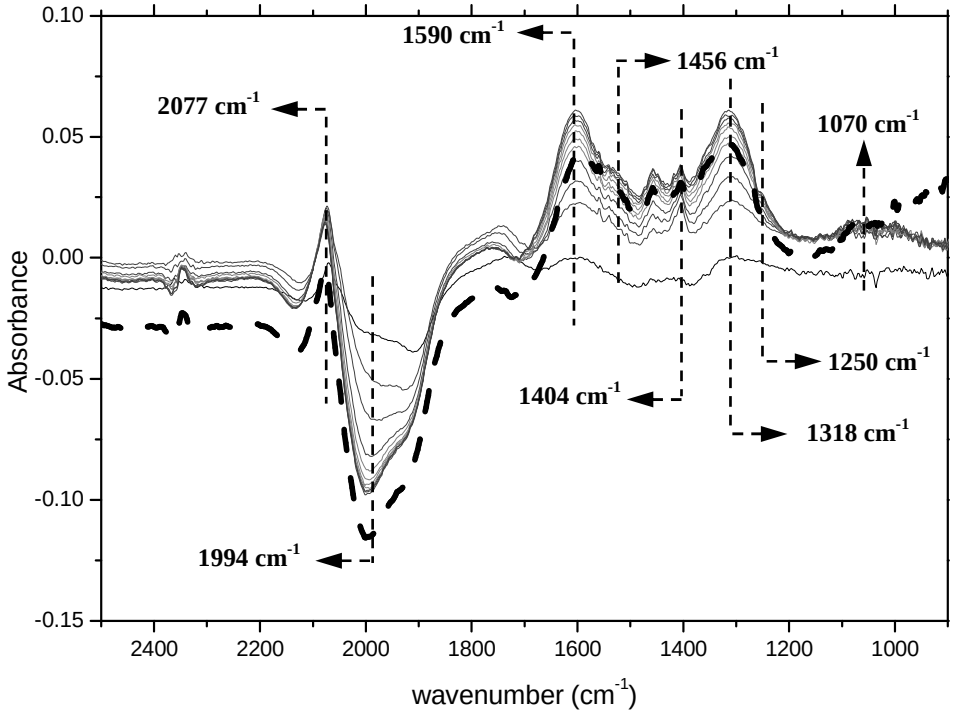

Figure C.4: DRIFT Spectra after exposure of $Pt/BaO/Ce_{0.25}Zr_{0.75}O_2$ catalyst to (a) 1 torr (b) 5 torr (c) 10 torr (d) 15 torr (e) 20 torr (f) 25 torr (g) 30 torr (h) 35 torr (i) 40 torr (j) 45 torr (k) 50 torr CO at 50^oC. All spectra were recorded after reaching equilibrium. Dashed line represents the spectra obtained after subsequent evacuation following 50 torr CO exposure

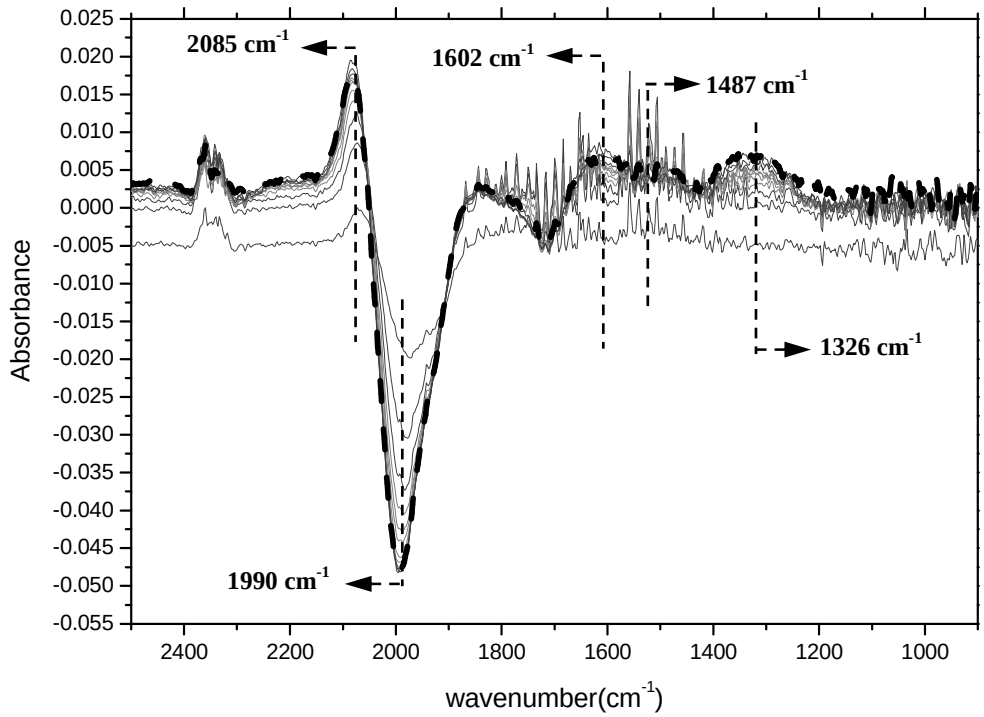

Figure C.5: DRIFT Spectra after exposure of $Pt/BaO/ZrO_2$ catalyst to (a) 1 torr (b) 5 torr (c) 10 torr (d) 15 torr (e) 20 torr (f) 25 torr (g) 30 torr (h) 35 torr (i) 40 torr (j) 45 torr (k) 50 torr CO at 50oC. All spectra were recorded after reaching equilibrium. Dashed line represents the spectra obtained after subsequent evacuation following 50 torr CO exposure

APPENDIX D

DRIFT SPECTRA OF CATALYSTS AFTER 10 % NO/Ar EXPOSURE

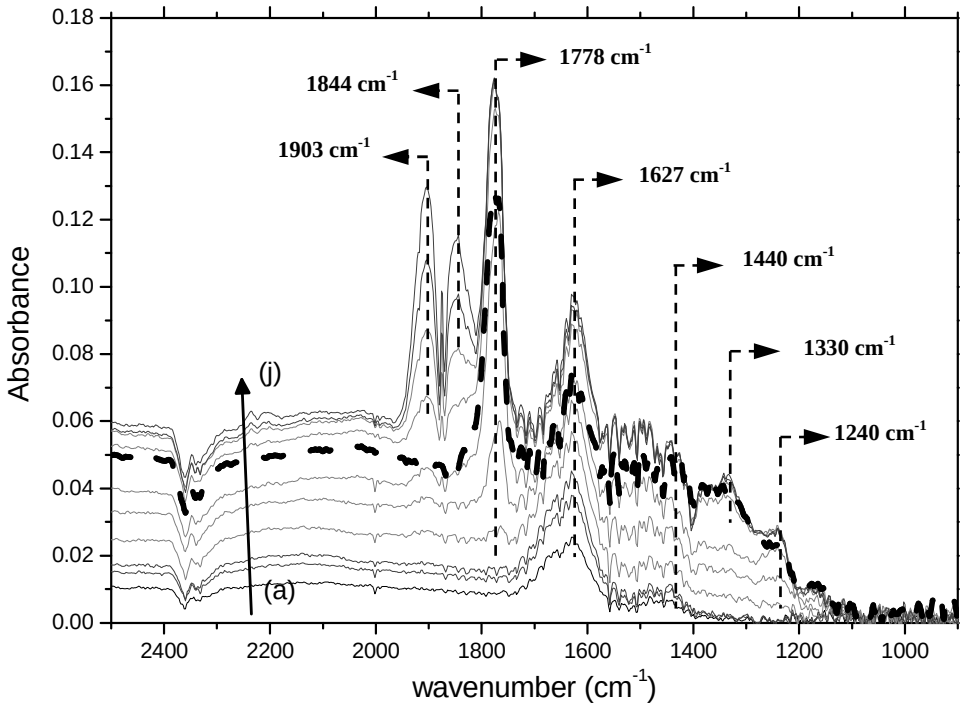

Figure D.1: DRIFT Spectra after exposure of $Pt/BaO/Al_2O_3$ catalyst to (a) 1 torr (b) 5 torr (c) 10 torr (d) 25 torr (e) 50 torr (f) 100 torr (g) 250 torr (h) 500 torr (i) 750 torr (j) 1000 torr 10% NO-Ar at RT. All spectra were recorded after reaching equilibrium. Dashed line represents the spectra obtained after subsequent evacuation following 1000 torr gas exposure.

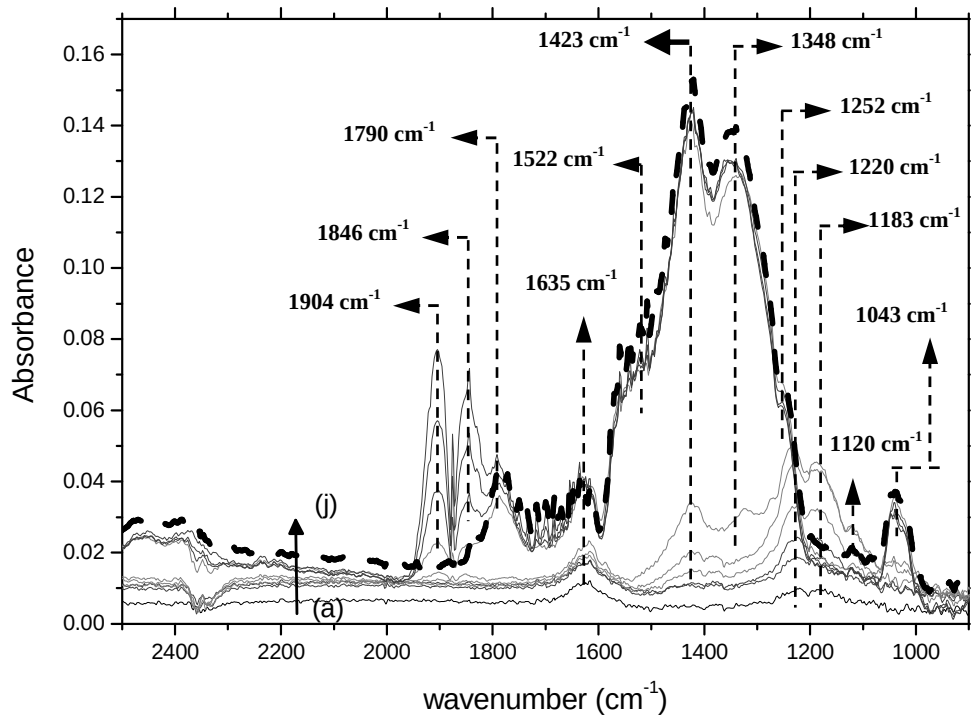

Figure D.2: DRIFT Spectra after exposure of $Pt/BaO/CeO_2$ catalyst to (a) 1 torr (b) 5 torr (c) 10 torr (d) 25 torr (e) 50 torr (f) 100 torr (g) 250 torr (h) 500 torr (i) 750 torr (j) 1000 torr 10% NO-Ar at RT. All spectra were recorded after reaching equilibrium. Dashed line represents the spectra obtained after subsequent evacuation following 1000 torr gas exposure.

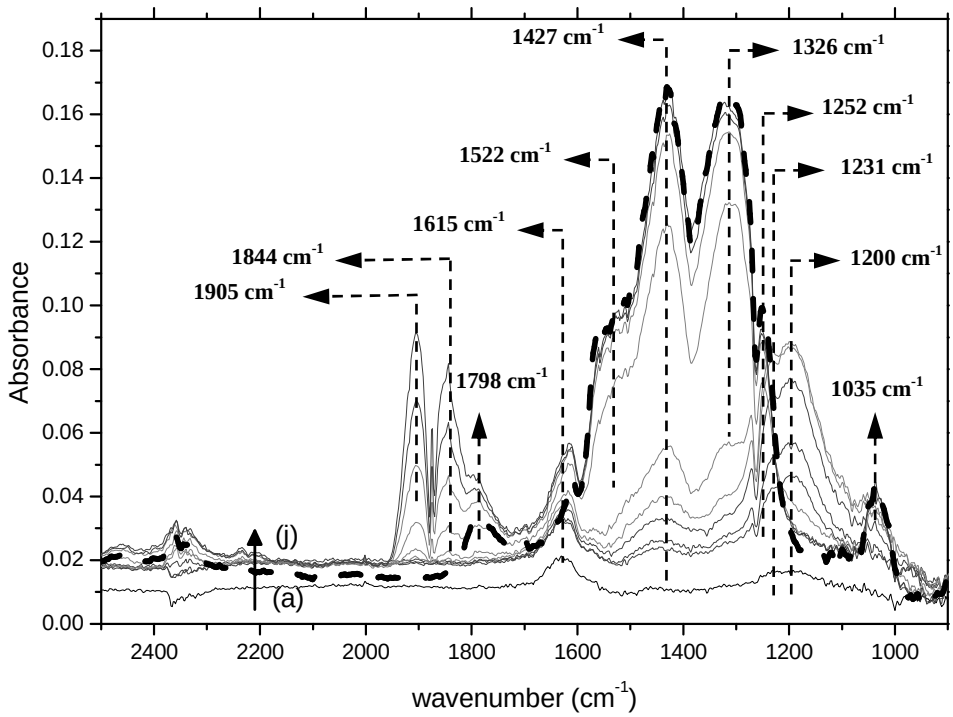

Figure D.3: DRIFT Spectra after exposure of $Pt/BaO/Ce_{0.75}Zr_{0.25}O_2$ catalyst to (a) 1 torr (b) 5 torr (c) 10 torr (d) 25 torr (e) 50 torr (f) 100 torr (g) 250 torr (h) 500 torr (i) 750 torr (j) 1000 torr 10% NO-Ar at RT. All spectra were recorded after reaching equilibrium. Dashed line represents the spectra obtained after subsequent evacuation following 1000 torr gas exposure

.

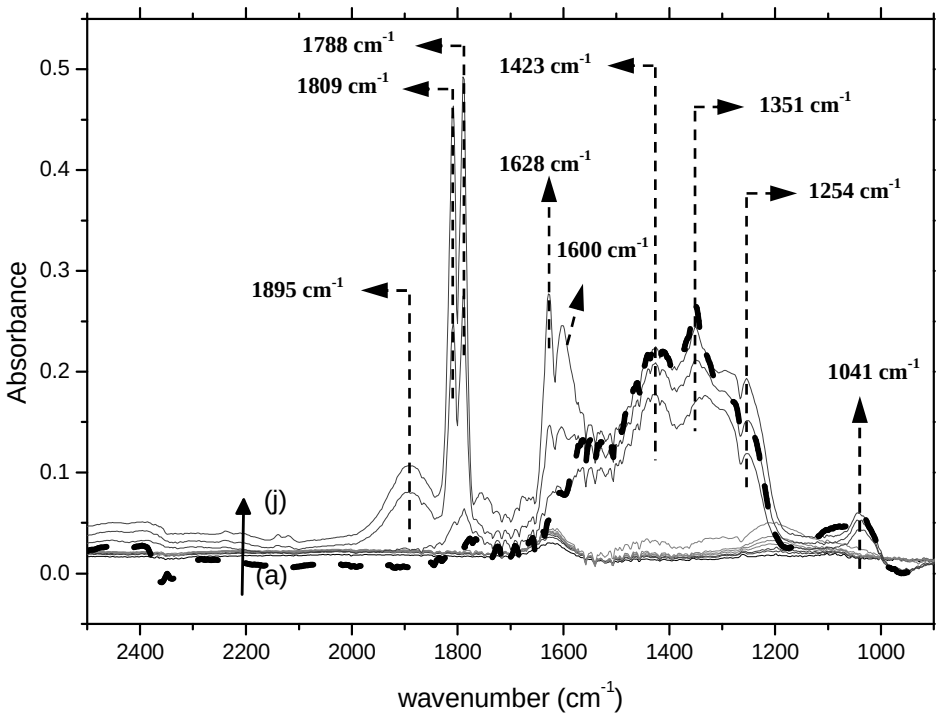

Figure D.4: DRIFT Spectra after exposure of Pt/BaO/$Ce_{0.5}Zr_{0.5}O_2$ catalyst to (a) 1 torr (b) 5 torr (c) 10 torr (d) 25 torr (e) 50 torr (f) 100 torr (g) 250 torr (h) 500 torr (i) 750 torr (j) 1000 torr 10% NO-Ar at RT. All spectra were recorded after reaching equilibrium. Dashed line represents the spectra obtained after subsequent evacuation following 1000 torr gas exposure.

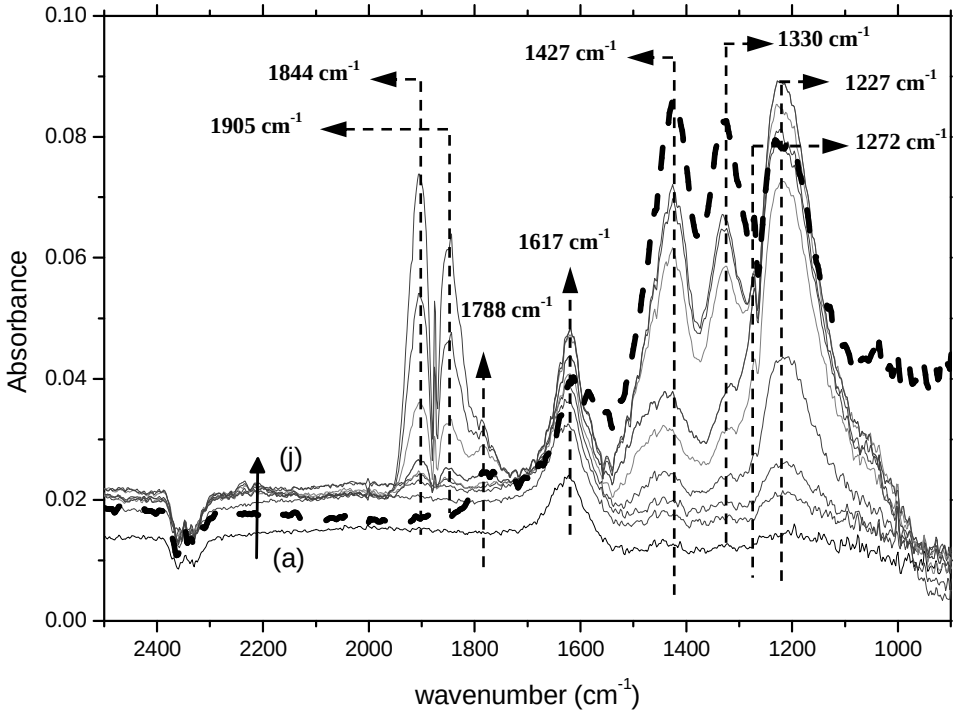

Figure D.5: DRIFT Spectra after exposure of Pt/BaO/$Ce_{0.25}Zr_{0.75}O_2$ catalyst to (a) 1 torr (b) 5 torr (c) 10 torr (d) 25 torr (e) 50 torr (f) 100 torr (g) 250 torr (h) 500 torr (i) 750 torr (j) 1000 torr 10% NO-Ar at RT. All spectra were recorded after reaching equilibrium. Dashed line represents the spectra obtained after subsequent evacuation following 1000 torr gas exposure.

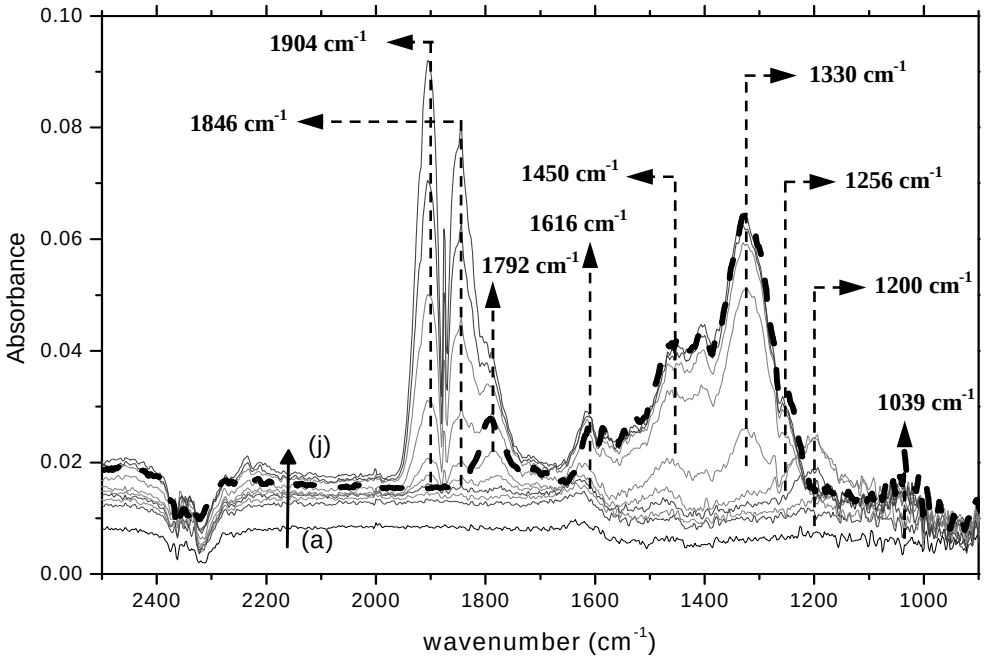

Figure D.6: DRIFT Spectra after exposure of $Pt/BaO/ZrO_2$ catalyst to (a) 1 torr (b) 5 torr (c) 10 torr (d) 25 torr (e) 50 torr (f) 100 torr (g) 250 torr (h) 500 torr (i) 750 torr (j) 1000 torr 10% NO-Ar at RT. All spectra were recorded after reaching equilibrium. Dashed line represents the spectra obtained after subsequent evacuation following 1000 torr gas exposure.

APPENDIX E

BACKGROUND SPECTRA OF CATALYSTS OBTAINED BEFORE 10 % NO/Ar GAS EXPOSURE

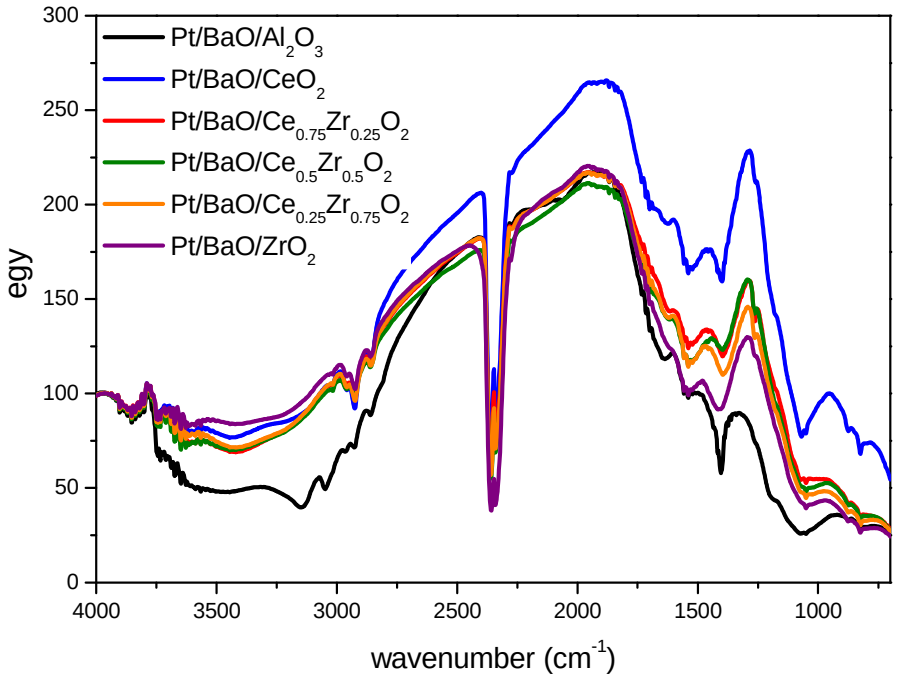

Figure E.1: Background spectra of catalysts that obtained before 10 % NO/Ar gas exposure